TÉCNICO LISBOA

On the Design of a Methodology for Camber Morphing Optimisation with Noise Reduction

Robert Valldosera Martinez

Thesis to obtain the Master of Science Degree in

Aerospace Engineering

Supervisors: Prof. Fernando José Parracho Lau
Dr. Frederico José Prata Rente Reis Afonso

Examination Committee

Chairperson: Prof. Filipe Szolnoky Ramos Pinto Cunha
Supervisor: Prof. Fernando José Parracho Lau
Member of the Committee: Prof. Edgar Caetano Fernandes

May 2019

”Sometimes it takes you a long time to sound like yourself.”

Miles Davis

Acknowledgments

I really want to thank Prof. Fernando Lau for having given me the opportunity to develop such a fulfilling thesis, involving different topics such as Computational Fluid Dynamics and Aeroacoustics, the latter completely new for me and which has definitely caught my attention for future dedication. I am truly grateful to Dr. Frederico Afonso for his unconditional attention and guidance through this period, for he has taught me to be critic and resolutive. I would also like to thank everybody in the Aerospace department's office for the very good times spent there and for their help, in particular to Simão Rodrigues for his kind help at any necessary moment, to João Souto for his dedication on making the acoustic framework possible, and to my beloved friend João Lourenço for his splendid help and friendship.
Specially, this thesis is dedicated to my parents, who have given everything to raise my two sisters and me so that now we can become what we wish to.

Resumo

No sentido de reduzir o ruído gerado por uma configuração híper-sustentadora 2D nas fases de descolagem e aterragem, uma estrutura adaptativa 2D tendo como base o mesmo perfil alar (NLR7301) foi desenhada recorrendo a uma otimização aerodinâmica de forma, tendo o resultado final sido comparado com a configuração híper-sustentadora. Para tal foi desenvolvida uma metodologia a qual consiste em otimizar a forma aerodinâmica do perfil alar base, considerando as equações estacionárias de RANS e um escoamento compressível a um determinado ângulo de ataque, visando maximizar o coeficiente de sustentação de forma a alcançar um valor similar ao da configuração híper-sustentadora e ao mesmo tempo respeitar os constrangimentos estruturais impostos. Para o efeito foi utilizado um algoritmo baseado em gradientes, os quais foram estimados recorrendo ao método adjunto. Após obter a forma ótima, uma análise aerodinâmica no domínio do tempo foi realizada para providenciar o algoritmo aeroacústico, baseado na formulação de Farassat 1A, com dados de pressão ao longo do tempo. Os resultados alcançados são posteriormente processados e comparados com os obtidos para a configuração híper-sustentadora. Ao comparar a solução de estrutura adaptativa com a configuração híper-sustentadora foi verificada uma redução de ruído gerado à custa de uma redução de sustentação máxima e um aumento de coeficiente de resistência aerodinâmico.

Palavras-chave: Estruturas Adaptativas, Aeroacústica, Mecânica dos Fluídos Computacional, Otimização Aerodinâmica de Forma

Abstract

In order to decrease the emitted airframe noise by a two-dimensional high-lift configuration during take-off and landing performances (NLR7301 with trailing edge flap), a morphing airfoil has been designed through a shape design optimisation procedure starting from a baseline airfoil (NLR7301), with the aim of emulating a high-lift configuration in terms of aerodynamic performances. A methodology has been implemented to accomplish such aerodynamic improvements on the aforementioned baseline airfoil by means of the compressible steady RANS equations at a certain angle of attack, with the objective of maximising its lift coefficient up to equivalent values regarding the high-lift configuration, while respecting the imposed structural constraints to guarantee a realistic optimised design. For such purpose, a gradient-based optimisation through the discrete adjoint method has been undertaken. Once the optimised airfoil is achieved, unsteady simulations have been carried out to obtain surface pressure distributions along a certain time-span to latter serve as the input data for the aeroacoustic prediction framework, based on the Farassat 1A formulation, where the subsequent results for both configurations are post-processed to allow for a comparative analysis. Conclusively, the morphing airfoil has proved to be advantageous in terms of aeroacoustics, in which the noise has been reduced with respect to the conventional high-lift configuration for a comparable lift coefficient, although being penalised by a significant drag coefficient increase due to stall conditions on the morphing airfoil's trailing edge.

Keywords: Morphing Structures, Aeroacoustics, Computational Fluid Dynamics, Shape Design Optimisation

Contents

List of Tables

List of Figures

Nomenclature

Greek symbols

α	Angle of attack.
Δ	Increment of a certain quantity.
δ_f	Flap deflection angle.
δ_{ij}	Kronecker delta
γ	Heat capacity ratio.
Γ_∞	Far-field.
κ	Thermal conductivity coefficient; Turbulent kinetic energy(Spalart-Allmaras turbulence model).
λ_i^{conv}	Convective spectral radius.
λ_i^{visc}	Viscous spectral radius.
μ	Molecular viscosity coefficient.
μ_t	Turbulent eddy viscosity.
ν_t	Turbulent kinematic viscosity.
Ω	Computational domain.
ϕ	Generic quantity.
ρ	Density.
ρ_o	Reference density.
τ_e	Emission time.
θ	Local angle between the normal to the surface and the radiation direction $\vec{r}$.

Roman symbols

A_B	Baseline airfoil area.
A_M	Morphing airfoil area.

c Chord.

c_B Baseline airfoil chord.

C_d Coefficient of drag.

c_f Flap chord.

C_l Coefficient of lift.

C_m Coefficient of moment.

c_M Morphing airfoil chord.

C_p Specific heat at constant pressure.

C_v Specific heat at constant volume.

E Total energy per unit mass.

e Specific internal energy.

f Frequency.

f_c Central frequency.

f_l Lower frequency limit.

f_u Upper frequency limit.

g_i Inequality-based constraints.

h Specific enthalpy.

$H(f)$ Heaviside function.

h_i Equality-based constraints.

I_{ind} Coordinate x tag for the design variables.

J_{ind} Coordinate y tag for the design variables.

k Fourier's law proportionality constant.

M Mach number.

M_r Mach in the radiation direction.

n Normal direction to the surface.

$N(i)$ Neighbours of node i.

n_N Number of nodes on the airfoil's surface.

p Pressure.

p'	Pressure fluctuation.
p'_L	Loading noise pressure fluctuation.
p'_T	Thickness noise pressure fluctuation.
p_{ref}	Reference pressure.
Pr	Prandtl number.
Q	Source term.
q	Heat flux.
R	Ideal gas constant.
R_i	Residuals of the governing equations at node i.
Re	Reynolds number.
S	Surface.
s_{ij}	Strain-rate tensor.
St_l	Strouhal number.
T	Temperature.
t	Time.
t^*	Desired observer time for computing the perturbations.
t_B	Baseline airfoil thickness.
t_M	Morphing airfoil thickness.
t_{DFT}	Execution time for Discrete Fourier Transform.
t_{FFT}	Execution time for Fast Fourier Transform.
T_{ij}	Lighthill's stress tensor.
u'	Velocity fluctuation.
u, v, w	Velocity Cartesian components.
U_∞	Free-stream velocity.
U_i	Velocity component.
v_n	Velocity on the normal direction to the surface.
w	Weighting factor.
y^+	Dimensionless wall-distance.

Subscripts

∞	Free-stream condition.
i, j, k	Computational indexes.
x, y, z	Cartesian components.
ref	Reference condition.

Superscripts

$\overline{\phi}$	Mean value of a certain quantity.
*	Adjoint.
T	Transpose.

Glossary

AD	Automatic Differentiation
CAA	Computational Aeroacoustics
CFD	Computational Fluid Dynamics
CFL	Courant-Friedrichs-Lewy
DFT	Direct Fourier Transform
FFD	Free Form Deformation
FFT	Fast Fourier Transform
FVM	Finite Volume Method
FW-H	Ffowcs-Williams and Hawking Acoustic Prediction Formulation
LBL-VS	Laminar-Boundary-Layer-Vortex-Shedding noise
LES	Large-Eddy Simulation
LE	Leading Edge
MPI	Message Passing Information
N-S	Navier Stokes
NACA	National Advisory Committee for Aeronautics
NASA	National Aeronautics and Space Administration
OASPL	Overall Sound Pressure Level
PDE	Partial Differential Equation
PIV	Particle Image Velocimetry
RANS	Reynolds-Averaged Navier-Stokes equations
SA	Spalart-Allmaras turbulence model
SLSQP	Sequential Least Squares Programming
SL	Sea Level Conditions
SPL	Sound Pressure Level
SST	Shear Stress Transport turbulence model
SU2	Stanford University Structured
TBL-TE	Turbulent Boundary Layer-Trailing Edge noise
TE	Trailing Edge

Chapter 1

Introduction

The importance of aircraft noise has become greater along the past decades and has been recognized and categorized as a serious environmental pollutant. Moreover, the health-related effects on the population surrounding the airports has also been a powerful reason for the development of measures in order to considerably reduce the noise emissions, as in conjunction with other environmental noise such as road traffic noise emissions, it has been stated to have influence on many diseases such as cardiovascular diseases, sleep disturbance and annoyance by the World Health Organization [1] in concordance with other researches [2–4]. Consequently, noise emission regulations were implemented by several policy-makers both in Europe (EASA) [5] and the United States (FAA) [6] (both equivalent to the ICAO standards [7]) due to the extended annoyance of the population and the general concern growth about the topic by the air transportation sector.

In the very beginning of aviation, airports were built outside the metropolis to avoid the population to be exposed to the produced noise. Nowadays, the urbanization tendency shows a globalisation behaviour of urban areas to increase their population while reducing the rural areas [8]. That is, an increase of urban population from 54% on 2014 to a 66% by 2050. This fact means that the peripheral airports have naturally been immersed into the urban areas and hence raised the population exposure to the generated noise. Followed by this tendency, the world's total population growth projection is also remarking a severe increase in addition to the life expectancy [9] which obviously contributes to this problem.

EuroControl has developed a European market demand forecast [10] for the incoming years until 2035 where four different scenarios are presented and analysed. As regulations' presence has drastically influenced the transportation sector through all the operational requirements, this study presents a "most-likely" scenario with a "Regulated Growth" of the market. This term refers to a moderate economic growth in conjunction with the environmental, social and economic demands to address the growing global sustainability concerns. It is predicted to be 14.4 million flights in Europe by 2035, which represents 1.5 times more than 2012. In other words, an increase of 50% which is an average of 1.8% increase per year. Even though traffic growth is expected to slow down by 2025 as the market would have arrived to a certain level of maturity, the capacity of many European airports will be arriving to their limit. In the same direction, two of the biggest companies from the Aerospace industry have developed

global market forecasts. Both Airbus and Boeing stated a 4.4% and a 4.7% global annual air traffic flow growth for the next 20 years, respectively [11, 12].

Parallel to this massive global market growth, the aviation industry is aware of its societal and environmental impact and many research projects involving many different institutions are pushing the developments of the aviation industry towards green aeronautical technologies, guaranteeing environmental sustainability as well as the more strict noise emissions regulations that will be continuously released along the years. As part of the EU Horizon 2020 research and innovation programme [13] from 2014, the largest European research programme at developing innovative, cutting-edge technology for reducing aircraft C02 and noise emissions Clean Sky 2 [14] is undertaking to achieve the ACARE 2020 goals [15] concerning the aircraft external noise reduction of 50% with respect to the year 2000 noise levels [16, 17] (i.e. minus 10 dB). In addition, the research also pursues noise emission long-term goals stated by the Europe's Vision for Aviation "Flightpath 2050" [18], setting the aspiring goal of reducing perceived noise by 65% compared to the noise levels in the year 2000.

With respect to the United States research programmes to noise emission reduction, it is necessary to mention the "Continuous Lower Energy, Emissions and Noise Program [19] from the Federal Aviation Administration (FAA) which is the principal environmental effort to accelerate the development of new aircraft and engine technologies and advance sustainable alternative jet fuels. This program was into five-year with companies such as Boeing, General Electric, Honeywell, Pratt I& Whitney and Rolls-Royce until 2015, followed on by the CLEEN II program being supported by new contributors such as Aurora Flight Sciences, Delta Tech Ops/MDS Coating Technologies and Rohr, Inc./UTC Aerospace Systems to achieve and improve the proposed goals by CLEEN I until 2020 [19]. Regarding to noise emissions, this program pursues a reduction of cumulative 32 dB below the Annex 16, Chapter 4 from the ICAO regulations [7].

It is evident that the global market growth involves a higher demand of both operations and aircraft. Boeing has anticipated the need for more than 41000 new deliveries over the next 20 years [12] in order to satisfy the above 4% global annual air traffic flow growth. Hence, air traffic operations will have to be redesigned and adjusted to withstand the high demands while fulfilling the noise and C02 emission restrictions imposed by the corresponding organisms. Far from the obvious, there are solutions that must be carefully considered such as the increase of rate of operations per hour in an airport. Documents *9426* [20] and *4444* [21] from the ICAO standards state a minimum separation between aircraft that are operating within the airport's jurisdiction regarding the wake vortices generated by an aircraft. That is, it may be not possible to increase the rate of operations as these restrictions must be followed in order to guarantee the safety of each individual aircraft. In order to make it a real option, only those airports with a viable expansion (in terms of territory availability and legislative compromises) for the incoming years will be able to reconsider the rates of operations per hour as improved airport logistics could be planified. One of this cases is the Heathrow airport, which would start (pending on a government last approval) a third runway project during the current year. This would suppose a severe increase in annual operations from 474000 to 740000 by 2040 according to the Airport Expansion Consultation of Heathrow [22].

But airport expansions are not suitable for the whole vast number of global operating airports due to

different factors such as lack of territory, lack of economic investment and overall social, political and economic factors. For those with an expansion approval, it is not clear how this will deal with the increasing noise reduction restrictions as well as to satisfy the market demand. Other possibilities would include the night flight operations which, by now, are being strongly restricted anywhere in the globe due to the noise annoyance caused to the residential areas in the vicinity. According to the sixth meeting organised by the Worldwide Air Transportation Conference [23], 241 airports are subjected to night flight restrictions. With respect to this amount, 66% are located in Europe and 16% in North America. As an illustrative example, Heathrow airport night shifts are banned under UK government legislation from 23:00h to 07:00h [22, 24].

Hence, noise reduction around airports is an urgent and crucial matter to be accomplished by the aviation industry as, in order to fulfil the inevitable demand growth and the noise emission restrictions, quieter aircraft are a requirement for its future. External noise produced by an aircraft is due to multiple sources that can be gathered into two different main groups: Engine noise and Airframe noise. The first generation of subsonic jet-liners were very noisy because of the high exhaust velocity of their engines. This high noise emission was reduced by 20 to 30 dB [25] by the implementation of high bypass ratio turbofans. The exhaust velocity was reduced but the same thrust was produced with a higher flow rate. In addition, there were gains in propulsive efficiency, which let to less fuel consumption and hence the high-bypass turbofan engines became the only choice for large commercial airliners. Even though the engine was the main source of noise, with the above mentioned reduction, airframe noise started being identified as a notorious noise source specially in the operations near airports where the high-lift devices and the landing gear were deployed [26].

1.1 Motivation and Objectives

High-lift devices are essential for approach and landing operations as they enable a substantial increment of lift to operate at the low speeds that are related to these manoeuvres. On the other hand, several researches have proven the high contribution to airframe noise [26–29] from the gap flows between the main wing and both the slat and the flap a well as the flap side-edge. This undesirable flow-induced noise is able to match and even exceed the engine noise during these operations. The complexity of the flow around a wing at a high-lift configuration is high due to different phenomena such as laminar-turbulent boundary layer transition, free shear layers, wakes, thick boundary layers and the interaction of these, among others. In addition, flow separation over the flap can occur at moderate angles of attack. The understanding of the characteristics of the flow are of vital importance in order to use the noise prediction models that have been developed [30–32].

But it was on 1980 that the Preliminary Design Department of Boeing, with the contribution of NASA, published a report about a novel technology: Morphing. The report discussed about the capabilities of a variable wing geometry [33] in order to reduce the fuel consumption and operating costs. This new concept, firstly introduced to increase the efficiency on cruise conditions, may also introduce remarkable improvements concerning noise emission reductions as the existing gaps between the flaps and the

slats with the main wing would be out of the equation. Thereby eliminating the complex aerodynamics that are created with conventional high-lift systems that may be followed by an airframe noise reduction. Experimental analysis have been developed in order to calculate the improvement in aerodynamic efficiency [34] and noise reduction [35] by morphing high-lift devices, but computational predictions for both fields are becoming necessary in order to comprehend the flow behaviour for reliable noise predictions and to optimize the design without unnecessary premature model testing.
The computation of the flow onto conventional and morphing high-lift devices in conjunction with the MDO framework developed by the IST [36, 37] from the NOVEMOR scope [38] and more specifically its noise prediction tool [39], will be adapted to the work's problem to enable the prediction of the benefits of the morphing concept for noise reduction.

1.2 State of the Art

Due to the importance of reducing the subsonic approach airframe noise, many researches have focused on locating the flow-induced noise sources. Experimental tests have been conducted to locate the flow-induced noise sources and to measure the far-field noise of the overall high-lift configuration [26, 28, 29, 40–46], specifically on the flap side-edge [29, 47, 48] and the component interaction effects on total radiated noise [49]. The noise data was acquired by fly-overs and microphone array displays and noise sources were mainly located unanimously in the slat and the flap side-edge. Two main noise generation mechanisms were identified at the slat: Noise generation caused by instabilities of the shear layer at the slat cusp and the vortex shedding behind the blunt trailing edge of the slat. Concerning the flap side-edge, the presence of a two-vortex system due to flow separation from each of the flap side-edges. Microphone array techniques have been a very important first step for acoustic data acquisition and consequent development of noise prediction semi-empirical models. The NASA Langley Research Center developed the high quality method DAMAS [50] in order to accurately quantify the position and strength of acoustic sources and minimize the microphone array technology data processing uncertainties.
The main goal to develop reliable computational results is the understanding of the flow features. Proceeded by experimental techniques such as hot wire anemometry [51, 52] or non-intrusive flow diagnostic systems such as Doppler velocimetry and particle image velocimetry [45, 53], CFD is taking the lead to supply details of this complex unsteady flow behaviour due to the limited data provided by the experimental techniques to clearly identify the noise sources. Several researches have investigated the quality of computational efforts of flow simulation and compared the results with experimental data in order to verify their functionality. Three-dimensional CFL3D [54, 55], developed by NASA, have been used by [56–58] combined with Spalart-Allmaras Turbulence model [59]. This code uses the unsteady, three-dimensional, compressible, thin layer Navier Stokes equations to model the flow, while this turbulence model is often employed for high-lift configurations involving multiple solid surfaces and wake/boundary layer interactions. Other works [60] used the INS3D-UP code [61] which solves incompressible Navier-Stokes equations, coupled with Baldwin-Barth turbulence model [62] which has shown to be properly

working with multi-element airfoil flows as well. Chasing the same goal but following another path, the flow computation [63] has been obtained by the Lattice Boltzmann method [64].

Concerning aeroacoustic purposes, computational slat aeroacoustic analysis have been developed [65, 66] by coupling Reynolds-Averaged Navier-Stokes (RANS) flow simulations with the Ffowcs Williams and Hawkings acoustic analogy [31], resulting on the identification of high amplitude, high frequency acoustic signals due to the slat trailing edge vortex shedding that correctly match with the experimental data [57]. Acoustic analogies are used in computational aeroacoustics in order to isolate the noise computation from the computation of the flow that is generating the noise, firstly proposed by the Lighthill's theory [67]. A study on the trailing edge of an airfoil, concluded that the coupling flow computations with the Ffowcs Williams and Hawkings analogy work properly if accurate flow information is given [68]. Other researches [69, 70] used the CFL3D (proven to give reliable results on the unsteady compressible flow and acoustics if appropriate grids and time steps are given [71]) in conjunction with the Two-equation Shear Stress Transport (SST) turbulence model [72] that concluded to obtain high intensity turbulent fluctuations near the reattachment location along the slat lower surface, and a strong vortex shedding behind the slat trailing edge resulting on high-amplitude acoustic waves, respectively.

Recent researches on CFD simulations have stated the better flow modelling with the use of hybrid RANS/LES methods to benefit from their different advantages and consequently becoming a predominant methodology. On one hand, RANS provide reliable information in the attached boundary layer, while LES (Large Eddy Simulations9 in separated flow regions. The most extended approximation to this methodology is presented by Spalart [73] and has been used to compute the flow-field [74, 75] and acoustic analysis by the different acoustic analogies (Ffowcs Williams and Hawkings and also Kirchoff [30] and Curle [76] methods).

Hence, a vast unsteady flow features have been identified as potential noise sources due to the complex geometry of conventional high-lift devices. Consequently, morphing structures may drastically reduce the flowfield instabilities by eliminating the regions responsible of this phenomena. The NASA Armstrong Flight Research Centre also tested the possible aerodynamic improvements the Flexsys technology [77] could bring with the Adaptive Compliant Trailing Edge (ACTE) flaps [34] on a Gulfstream III (GIII), but the computational predictions of aerodynamic benefits over-predicted the lift increment for large angles of attack. In the same direction and coordinated by AIRBUS, the SARISTU project [78] was born on 2010 and involved the design of both an adaptive leading and trailing edge proved the performance improvements in the Russian Aeronautical Research Centre's wind tunnel at low speed flow ($M = 0.3$). Other experimental researches with morphing flaps [35] stated a reduction on the flap side edge noise with their proposed design.

From a computational point of view, a NASA Common Research Model (CRM) was equipped with Variable Continuous Camber Trailing Edge Flap (VCCTEF) by two different researches [79, 80] and showed the capabilities of a morphing flap by reducing the induced drag from 1.3% up to 7.7% with the different configurations that were tested. Hence, in conjunction with the other researches, they may have flagged the beginning of a potential field.

Finally, the structural point of view must be taken into account. The availability of a material to be used

for the wing skin for changing its shape while resisting the aerodynamic loads is still a major challenge and the materials and structures sectors are chasing new technologies to make it possible [81–83] such as elastomer based skins and several studies have introduced different designs for a variable-camber trailing edge [84, 85].

1.3 Thesis Outline

This thesis is divided in 6 chapters, starting from the introduction to the present work, which gives an overview of the topics faced within it. Chapter 2 presents the background of all formulations used to develop a Computational Fluid Dynamics (CFD) simulation, as well as the Aeroacoustic noise prediction formulations, followed by chapter 3, in which the methodology to implement all the aforementioned tools is widely introduced, starting with a brief description of the software used, towards the computational set-up for accurate flow description, shape design optimisation and the aeroacoustic framework implementation. Chapter 4 presents the validation test-cases for the CFD set-up and the acoustic framework, compared to the present work's results. Finally, chapter 5 exhibits the optimisation and aeroacoustic results, that lead the way to chapter 6, with the main conclusions of the work done. Appendixes are also included, which complement some discussions.

Chapter 2

Theoretical Background

This chapter presents the necessary theoretical background that conforms the fundamental tools used in the present work to accomplish its objectives, accompanied with the reasoning behind their choice. The first part of this thesis will face the flow modelling around a high-lift configuration, composed by the main element together with a trailing edge flap, corresponding to take-off and landing performances. Subsequently, a gradient-based shape optimisation is undertaken in order to generate a morphing airfoil which reaches, or even surpasses, the performance requirements of the flapped configuration in terms of maximum lift, while avoiding significant penalisation onto the drag. This way, the hypothesis of airframe noise reduction via eliminating the existing gap between the flap and the main element can be addressed. Starting from section 2.1 to section 2.4, the flow equations that are utilised to computationally describe the flow behaviour around an airfoil geometry are exhibited, accompanied by the presentation of the turbulence model (which culminates the flow description together with the flow equations), as well as a proper selection of the boundary conditions so as to properly define the physical domain. These are presented whether analysing a high-lift configuration or a single morphed airfoil. The second part of the present work faces an aeroacoustic study, in which noise levels from both flapped and morphed airfoils are calculated at certain locations within the domain, emulating a microphone display. Section 2.5.1 introduces the airframe noise sources, followed by sections 2.5.2 to 2.5.5, in which there are presented the mathematical fundamentals of the acoustic formulations used to compute the airframe noise. It is within section 2.5.6, where the acoustic data post-processing tools are introduced, through which comprehensible acoustic results are generated, enabling us for discussion regarding both flapped and morphed airfoils' noise contributions.

2.1 Fluid Dynamics Flow Equations

Properly characterising the physical flow behaviour within the domain is of crucial importance for both aerodynamic and aeroacoustic studies, as they are fully related to each other. By an accurate description of the flow properties, reliable aerodynamic airfoil capabilities (in terms of lift and drag coefficients) are generated, resulting into comparable results to experimental studies that validate the methodology

within the present work. Consequently, reliable comparisons between the flapped and morphed airfoils' aerodynamic performances can be undertaken. Following this part, in order for the acoustic framework to properly predict the aeroacoustic noise, a detailed and accurate surface flow description is needed, as it is used as the input data for the acoustic framework, in the form of surface pressure distribution. Hence, it is conclusively evident that, for all purposes of this work, generating detailed aerodynamic data is fundamental for all subsequent steps.

The understanding of an aerodynamic flow around an object is based on the fundamental governing equations of fluid dynamics, which are the continuity, momentum, and energy equations. These are obtained by applying the principle of conservation laws to these three quantities, resulting into a system of partial differential equations (PDE) that model the physics of the problem. From a generic point of view, the governing equations expressed in their differential and conservation form should have the following structure on a domain $\Omega \subset \mathbb{R}^3$:

$$\frac{\partial \vec{V_s}}{\partial t} + \nabla \cdot \vec{F}^c - \nabla \cdot \vec{F}^v = Q \quad \text{in } \Omega, t > 0 \tag{2.1}$$

Let us identify each of the terms: $\vec{V_s}$ is a vector composed by the state variables, of which both convective fluxes ($\vec{F}^c$) and viscous fluxes ($\vec{F}^v$) are a function of: $\vec{F}^c = \vec{F}^c(\vec{V_s})$, $\vec{F}^v = \vec{F}^v(\vec{V_s})$. The vector of state variables is of the form:

$$\vec{V_s} = (\rho, \rho u, \rho v, \rho w, \rho E)^T \tag{2.2}$$

in where ρ is the air density, $\vec{U} = (u, v, w)$ is the velocity vector of the flow, and E is the total energy per unit of mass. It must be stated that this vector is space (x, y, z) and time t dependent. Lastly, with respect to Q, it is a source term. Applying the fundamental physical principles of conservation to the aforementioned quantities, in addition to considering a Newtonian fluid[1], the compressible Navier-Stokes continuity, momentum, and energy equations in conservation form, for a viscous flow arise:

$$\frac{\partial \rho}{\delta t} + \frac{\partial}{\partial x_i}(\rho u_i) = 0 \tag{2.3}$$

$$\frac{\partial}{\partial t}(\rho u_i) + \frac{\partial}{\partial x_j}(\rho u_j u_i) = -\frac{\partial p}{\partial x_i} + \frac{\partial \tau_{ij}}{\partial x_j} + \rho f_i \tag{2.4}$$

$$\frac{\partial}{\partial t}\left[\rho\left(e + \frac{1}{2}u_i u_i\right)\right] + \frac{\partial}{\partial x_j}\left[\rho u_j\left(h + \frac{1}{2}u_i u_i\right)\right] = \frac{\partial}{\partial x_j}(u_j \tau_{ij}) - \frac{\partial q_j}{\partial x_j} \tag{2.5}$$

where e is the specific internal energy, $h = e + p/\rho$ is the specific enthalpy, built with the specific internal energy, density and pressure p. τ_{ij} is the viscous stress tensor, q_j is the heat flux vector and f_i the body force per unit of mass acting on the fluid. The presented equations are formulated with Einstein's notation, where subscripts i, j refer to each of the Cartesian directions from the frame of reference. For

[1] A Newtonian fluid is that where there exists a linear relation between the shear stresses and the velocity gradients, which are equivalent to the time rate of strain.

further understanding about these equations, all their derivation is extensively covered in [86].

Regarding the physical properties of the atmospheric air, for most of the aeronautical applications it can be considered to behave as an ideal gas, in which the macroscopic variables (p, T, ρ) are related to each other via the expression

$$p = \rho RT = (\gamma - 1)\rho e \tag{2.6}$$

in which the air temperature T appears. Concerning the viscous stress tensor, it is defined as

$$\tau_{ij} = 2\mu\left(s_{ij} - \frac{1}{3}\frac{\partial u_k}{\partial x_k}\delta_{ij}\right) \tag{2.7}$$

composed by the strain-rate tensor, expressed as

$$s_{ij} = \frac{1}{2}\left(\frac{\partial u_i}{\partial x_j} + \frac{\partial u_j}{\partial x_i}\right). \tag{2.8}$$

The convective heat flux is built through the proportionality Fourier's law for heat conduction:

$$q_j = -k\frac{\partial T}{\partial x_j} \tag{2.9}$$

by means of the thermal conductivity, k. Lastly, the specific internal energy and specific enthalpy are of the form

$$e = c_v T, \qquad h = c_p T \tag{2.10}$$

which are driven by the specific heat coefficients: c_v and c_p, (where $\gamma = c_p/c_v$, and $R = c_p - c_v$). Hence,

$$q_j = -k/c_p\frac{\partial h}{\partial x_j} = -\frac{\mu}{Pr}\frac{\partial h}{\partial x_j} \tag{2.11}$$

where the Prandtl number arises, being

$$Pr = \frac{c_p \mu}{k} \tag{2.12}$$

2.1.1 Reynolds-Averaged Navier-Stokes Equations (RANS)

In the present work's upcoming computational simulations, high Reynolds numbers define the flow, which has a direct influence on the boundary layer's nature. Under these conditions, a large area of the boundary layer becomes turbulent, a flow regime characterised by chaotic particle trajectories due to the randomness of their velocity fluctuations (both in space and time) [87]. The limitation of nowadays available computational power makes its prediction via the exact solution of the Navier-Stokes equations unachievable, and alternatives must be undertaken. Here are introduced the so-called **Reynolds-Averaged Navier-Stokes** equations. They imply an approach to turbulence, in which all of the unsteadi-

ness is considered as part of the turbulence and is time-averaged, decomposing the flow variables into two contributions [88] in each volume of control: its mean value along time and its fluctuating contribution as

$$u_i = \overline{u_i} + u_i', \qquad p = \overline{p} + p' \tag{2.13}$$

for each velocity component and the pressure, respectively (called the Reynolds decomposition). It is of major importance that the averaging time is defined so as it only acts upon the turbulence time-scale, leaving other flow features belonging to different time-scales, untouched (such as flow recirculation due to adverse pressure-gradients belonging to stall conditions). Otherwise, the flow description would be impoverished and less information would be given. The next step is averaging each of the equations composing the whole system of equations. These two steps together add an unknown term within the system known as the Reynolds-stress tensor, which must be modelled by a proper turbulence model to allow the *RANS* system of equations to be closed and hence solved, introduced in the following section (2.2).

Regarding the time Reynolds average of a quantity ϕ, it is defined as

$$\overline{\phi}(x,t) = \frac{1}{T}\int_T \phi(x,t)\partial t \tag{2.14}$$

where, if compressibility effects are to be accounted, the density weighted Favre-averaging should be implemented [89]. However, its use is necessary for high compressible flows and hypersonic flows. As the present work is focusing on subsonic performances regarding take-off and landing, the flow can be assumed to be under an incompressible behaviour, meaning that turbulent fluctuations do not imply substantial density fluctuations, except for some slight local compressibility effects on the leading edges' flow acceleration points, where Mach numbers around $M = 0.6$ can be achieved. In any case, Favre-averaging is not necessary and Reynolds averaging (equation 2.14) is sufficient. Following these reasoning, and in order to be conservative and loyal to the flow characteristics, the RANS equations for a compressible, viscous flow will be considered:

$$\frac{\partial \overline{\rho}}{\partial t} + \frac{\partial}{\partial x_i}(\overline{\rho}\,\overline{u}_i) = 0 \tag{2.15}$$

$$\frac{\partial}{\partial t}(\overline{\rho}\,\overline{u}_i) + \frac{\partial}{\partial x_j}(\overline{\rho}\,\overline{u}_i\,\overline{u}_j) = -\frac{\partial \overline{p}}{\partial x_i} + \frac{\partial \overline{\tau}_{ij}}{\partial x_j} - \frac{\partial}{\partial x_j}(\overline{\rho u_i' u_j'}) + \overline{\rho} f_i \tag{2.16}$$

$$\begin{aligned}\frac{\partial}{\partial t}\left[\overline{\rho}\left(\overline{e} + \frac{1}{2}\overline{u}_i\,\overline{u}_i\right) + \frac{1}{2}\overline{\rho u_i' u_i'}\right] + \frac{\partial}{\partial x_j}\left[\overline{\rho}\,\overline{u}_j\left(\overline{h} + \frac{1}{2}\overline{u}_i\,\overline{u}_i\right) + \overline{u}_j\frac{\overline{\rho u_i' u_i'}}{2}\right] = \\ \frac{\partial}{\partial x_j}\left[\overline{u}_i\left(\overline{\tau}_{ij} - \overline{\rho u_i' u_j'}\right) - \overline{q} - \overline{\rho u_j' h'} + \overline{\tau_{ij} u_i'} - \overline{\rho u_j' \frac{1}{2} u_i' u_i'}\right]\end{aligned} \tag{2.17}$$

$$\overline{p} = (\gamma - 1)\overline{\rho}\,\overline{e} \tag{2.18}$$

in which the Reynolds-stress tensor arises, $\overline{\rho u_i' u_j'}$, adding unknowns to the problem. It is within this term where the effects of turbulent motions are added to the mean stresses. The consequent step, consists in expressing this term as a function of the mean-field and/or other variables, normally by means of turbulence models. In the particular case of eddy-viscosity models (which are discussed in the following section 2.2), this can be done directly as:

$$\overline{\rho u_i' u_j'} = \frac{2}{3}\overline{\rho}\kappa\delta_{ij} - 2\mu_T\left[\frac{1}{2}\left(\frac{\partial \overline{u}_i}{\partial x_j} + \frac{\partial \overline{u}_j}{\partial x_i}\right) - \frac{1}{3}\frac{\partial \overline{u}_k}{\partial x_k}\delta_{ij}\right] \tag{2.19}$$

where κ is the turbulent kinetic energy, and the concept of eddy viscosity appears, μ_T. Together with it, the need of determining its value also arises, which will be the task of the chosen turbulence model.

The use of the RANS equations in aerodynamics for high-lift configurations and single airfoils is well established and very wide, where several works such as [90–93] have proved their validity. For further understanding of the procedures and concepts of this section, the reader may be addressed to [87–89, 94].

2.2 Turbulence Model

Several experimental test cases have been gathered by the *Advisory Group for Aerospace Research & Development* (*AGARD*) with the objective of providing support for the validation of CFD codes [95]. In particular, there is one set that is of interest for this thesis, which consists of a low-speed two dimensional **NLR7301** airfoil together with a trailing edge flap, with an enormous supply of experimental data to validate computational results as well as accessible coordinates to generate its geometry. Table 2.1 summarises its set-up conditions:

Mach, *M*	0.185
Angle of attack, α	[6° , 13.1°]
Reynolds, *Re*	$2.51{\cdot}10^6$

Table 2.1: Set-up conditions of the experiment from [95].

As noticeable, the conditions are those of a take-off and landing performances, thus being a perfect target to be implemented within the present work. The results of this particular set were originally obtained by B. van den Berg [96] and have been used by many works such as [91, 97] in order to validate their correspondent computational models.

Regarding which turbulence model to implement, many works have provided detailed comparisons on the flapped *NLR7301*, as well as other high-lift configurations, between two important turbulence models: the one-equation **Spalart-Allmaras** turbulence model, and the two-equation **Menter SST** tur-

bulence model. Among the aforementioned comparative works, particularly two (very recommended) works are behind the reasoning of the definitive choice of the turbulence model for all subsequent computational simulations: [90, 91]. Both works' flow Mach and Reynolds numbers are within the range of B. van den Berg [96] experiments, testing different angles of attack leading to fully attached flows up to separation features. Both works suggest a good performance of the two models on fully attached flows, in comparison with experimental surface pressure distribution and skin-friction data. However, Spalart-Allmaras model shows higher robustness and efficiency, as well as good quality in handling the interaction between boundary layers and wakes (which is of great interest considering multi-element flow interactions). On the contrary, Menter's model provides better agreement on separated regions, although Spalart-Allmaras model does not excessively differ, in addition to a reasonable prediction of the separation point by the two models.

The first test developed in this thesis is the flapped *NLR7301* with fully attached flow (presented in section 3.2). Secondly, when facing the single-element shape optimisation, flow separation is not expected to occur within the first steps of its shape deformation evolution, leading to a clear predominance of attached flows within the upcoming simulations. In such a case where separation features would arise, considering Spalart-Allmaras' fair predictions for such flows, as well as its computational efficiency and robustness, makes it to be adequate for the present work, in addition to already having been validated by [90, 91] and [97]. Hence, Spalart-Allmaras is chosen in order to guarantee the closure of the *RANS* equations and is introduced in the following paragraphs.

In laminar flows, the transport mechanism of momentum between two adjacent layers is only achieved by molecular mixing or molecular diffusion. When turbulence arises, there is an increase of the momentum transport at a larger scale caused by the eddies that move between layers, and so the shear stresses cannot be simply modelled by the Newton's law of viscosity:

$$\tau = \mu \frac{\partial u}{\partial y} \tag{2.20}$$

In order to give a solution to this problem, the Boussinesq approximation was introduced [98], which states that the turbulence effect can be modelled by an increase of viscosity that can describe the motion of a turbulent flow from a larger scale than molecular. Hence, segregating the viscosity belonging to a laminar flow and to a turbulent flow gives the total viscosity of the fluid under a turbulent motion:

$$\mu_T = \mu + \mu_t \tag{2.21}$$

Spalart-Allmaras is a one-equation turbulence model. The particularity of one-equation models is to provide the calculation of the kinetic turbulent energy [88] via one transport equation expressed in terms of an eddy viscosity term $\tilde{\nu}$, while the turbulence length scale is defined empirically [87], being of the

following form:

$$\frac{D\tilde{\nu}}{Dt} = C_{b1}[1 - f_{t2}]\tilde{S}\tilde{\nu} + \frac{1}{\sigma}[\nabla \cdot (\nu + \tilde{\nu})\nabla\tilde{\nu}] + \frac{C_{b2}}{\sigma}(\nabla\tilde{\nu})^2 - \Big[C_{w1}f_w - \frac{C_{b1}}{\kappa^2}f_{t2}\Big]\Big(\frac{\tilde{\nu}}{d}\Big)^2 + f_{t1}\ \Delta U^2 \tag{2.22}$$

where the kinematic eddy viscosity is computed as

$$\nu_t = \frac{\mu_t}{\rho}, \qquad \nu_t = \tilde{\nu} f_{v1} \tag{2.23}$$

and

$$f_{v1} = \frac{\chi^3}{\chi^3 + C_{v1}^3}, \tag{2.24}$$

$$\chi = \frac{\tilde{\nu}}{\nu} \tag{2.25}$$

and the production term

$$\tilde{S} = S + \Big(\frac{\tilde{\nu}}{\kappa^2 d^2}\Big) f_{v2} \tag{2.26}$$

where *S* is the magnitude of the vorticity and *d* the distance to the closest wall. The term f_{v2} is computed as

$$f_{v2} = 1 - \frac{\chi}{1 + \chi f_{v1}} \tag{2.27}$$

The wall effect in the boundary layer region acts as a destructive factor on the Reynolds shear stresses and the term c_{w1} provides the balance between production and diffusion terms and the destruction term [59]:

$$C_{w1} = \frac{C_{b1}}{\kappa^2} + \frac{(1 + C_{b2})}{\sigma} \tag{2.28}$$

which must be corrected by the non-dimensional term f_w in order to ensure a correct decay of the destruction term towards the outer region of the boundary layer:

$$f_w = g\Big[\frac{1 + C_{w3}^6}{g^6 + C_{w3}^6}\Big] \tag{2.29}$$

where

$$g = r + C_{w2}(r^6 - r) \tag{2.30}$$

$$r = \frac{\tilde{\nu}}{\tilde{S}\kappa^2 d^2} \tag{2.31}$$

Finally, the boundary conditions must be addressed. The wall boundary condition on the solid surface

is satisfied when $\tilde{\nu} = 0$. This means there is no eddy production on the wall. On the other hand, a good assumption for the far-field condition could be assessed by imposing a decay of $\frac{1}{10}th$ of ν. To conclude, the value of all the coefficients that have been stated above can be found in [59].

2.3 Boundary Conditions

Once having introduced the tools to describe the flow, it is now a natural step to present where these are to be applied, while considering all specific physical considerations at certain locations of the domain $\Omega \subset \mathbb{R}^3$. Concerning to this matter, two different boundaries must be taken into account within the computational domain (see figure 2.1): the airfoil (S) and the far-field (Γ_∞). The physical boundary conditions to be set upon them are of great transcendence for the solutions obtained with the governing flow equations and vary from one specific problem to another. Consequently, there must be full certainty regarding the characteristics of the problem under study and the applicable assumptions to obtain realistic solutions.

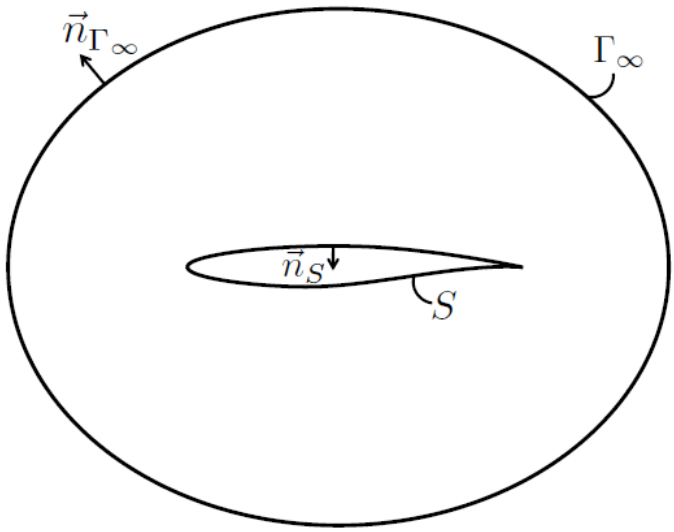

Figure 2.1: Boundaries from the simulation domain Ω [92].

Under the consideration of a viscous flow, the corresponding boundary condition on a stationary airfoil applies a zero relative velocity between the surface and the gas immediately at this surface [86],

$$\vec{U}_s = \vec{0} \tag{2.32}$$

which is known as the *no-slip* condition. Analogous to it, the temperature at the surface of the material can also be used as a no-slip boundary condition in case it is known, denoted as T_s. Hence, the temperature of the fluid layer (T) immediately in contact with this surface is also T_s:

$$T = T_s \tag{2.33}$$

However, the temperature at the airfoil surface is not always known, for example, because of changing as a function of time due to aerodynamic heat transfer whether emitted or received. Consequently, the boundary condition is ruled by the Fourier law of heat conduction at the surface:

$$\dot{q}_s = -\Big(k\frac{\partial T}{\partial n}\Big)_s \tag{2.34}$$

where $\dot{q}_s$ is the instantaneous heat flux to the surface and n its normal direction. A very common practice is to assume the airfoil surface as an adiabatic wall due to the simplicity of this set up, which means that there is no heat transfer to the surface ($\dot{q}_s = 0$),

$$\Big(\frac{\partial T}{\partial n}\Big)_s = \vec{0}. \tag{2.35}$$

With respect to the far-field boundary conditions, by definition, are those applied at an infinite distance from the surface where its perturbation upon the flow is null. Therefore, the values of the flow variables belonging to the free-stream are applicable to the flow variables of the far-field boundaries on the outer limits of the computational domain [86, 92]:

$$\vec{V_s}|_{\Gamma_\infty} = \vec{V_s}|_\infty \tag{2.36}$$

where $\vec{V_s}$ is the vector of state variables.

2.4 The Finite Volume Method (FVM)

Up to this point, the reader has been taken along the *what* to use so as to describe the flow behaviour through sections 2.1 and 2.2, where the RANS equations and the Spalart-Allmaras turbulence model have been introduced. Afterwards, in section 2.3, the *where* has been addressed, defining the physical characteristics of the domain's boundaries through boundary conditions, acting upon the airfoil's geometry and the computational domain's limits, or far-field. The following section develops the concept of the *how*, in terms of which strategies are implemented to use the RANS equations onto the flow domain.

The Finite Volume Method (FVM) is a discretisation method which is used for numerical simulations of conservation laws. Its use is broad in many engineering fields, specially this work's focus: fluid mechanics, due to the simplicity on its formulation. The feature that gives great versatility to this method is its adaptation to any kind of problem involving any arbitrary geometry, due to the fact that the discretisation is directly developed in the physical space, avoiding any coordinate transformation between this one's and the computational coordinate system [99]. In addition, it is applicable to both structured and unstructured grids and consequently, along time, its role in comparison with *finite difference* and *finite element* methods has become predominant. As it will be introduced in section 3.1, this work will use

the open-source computational software SU^2 [100] and hence the numerical algorithms will be the ones belonging to this tool.

First of all, it is mandatory to introduce where the finite volume method will apply the flow conservative equations onto the domain, which has previously been subdivided into several cells by means of a grid. Concerning these subdivisions, SU^2 defines a control volume as follows in figure 2.2:

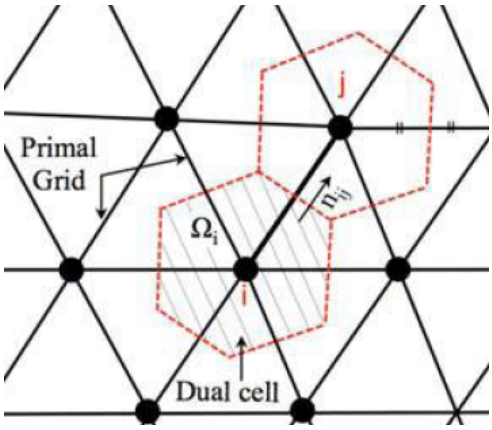

Figure 2.2: Illustration of both primal and dual meshes [100].

The primal grid locates the position of each node throughout the domain. The volumes of control are built using a median-dual, vertex-based scheme, where the centroids, faces and edge-midpoints of the cells sharing a particular node are interconnected, forming the dual grid, where the flow variables are stored at the grid points/nodes. Hence, an accurate resolution of face fluxes is achieved for all kinds of mesh, yielding, however, a lower order accuracy of element-based integrations since the vertex is not necessarily at the element centroid [99].
In the first step of the finite volume discretisation process, the governing equations are integrated over the volumes of control shown in figure 2.2, to subsequently applying the Gauss theorem to transform the volume integrals belonging to convective and diffusive terms, into surface integrals, giving birth to the semi-discretised PDE. Using the notation in [100] in a volume of control (Ω_i), it is of the form:

$$\int_{\Omega_i} \frac{\partial \vec{V_s}}{\partial t} \partial\Omega + \sum_{j \in N(i)} (\tilde{F}_{c_{ij}} + \tilde{F}_{v_{ij}}) \Delta S_{ij} - Q \mid \Omega_i \mid = \int_{\Omega_i} \frac{\partial \vec{V_s}}{\partial t} \partial\Omega + R_i(\vec{V_s}) = 0 \tag{2.37}$$

where $\vec{V_s}$ is the vector of state variables previously defined in section 2.1. Concerning $\tilde{F}_{c_{ij}}$ and $\tilde{F}_{v_{ij}}$, these are the projected numerical approximations of the convective and viscous fluxes, respectively, onto the $\vec{n}_{ij}$ direction and Q is a source term. The area of the face associated with the edge ij is denoted by ΔS_{ij} whereas $N(i)$ are the neighbours surrounding node i. The FVM method evaluates the surface fluxes at the faces of the volume of control, which guarantees the local conservativity of the numerical fluxes, as they are conserved from one volume of control to another [99]. The next step is presenting the numerical algorithms that are implemented for both spatial and time discretisations of the terms in equation 2.37. Along this procedure, a segregation of the numerical schemes for the discretisation of the spatial and temporal terms, allows different numerical schemes to be implemented

that best suit the characteristics of the problem, each of them having their own order of accuracy.

2.4.1 Spatial Discretisation

The following sections will describe the methods used for the discretisation of convective ($\tilde{F}_{c_{ij}}$) and viscous fluxes ($\tilde{F}_{v_{ij}}$) from equation 2.37. Their evaluation is carried out at the midpoints of each volume's of control edges (f_i), as shown in figure 2.3:

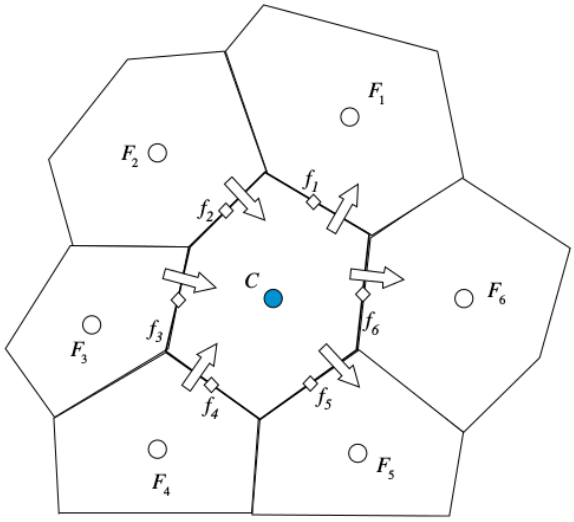

Figure 2.3: Fluxes computed at the midpoint of the volume of control's edges [99].

The preferred methodology to be conducted within the present work for the convective fluxes is the upwind flux-difference-splitting scheme by *Roe* [101], instead of the also available Jameson-Schmidt-Turkel (JST) scheme [102], which is more suitable to use for transonic and supersonic simulations, for example in cases involving flow discontinuities such as shock waves. Roe scheme evaluates the convective fluxes from flow quantities reconstructed separately on both sides of the face of the control volume from values at the surrounding nodes:

$$\tilde{F}_{c_{ij}} = \tilde{F}(\vec{V}_{si}, \vec{V}_{sj}) = \left(\frac{\vec{F}_i^c + \vec{F}_j^c}{2} \right) \cdot \vec{n}_{ij} - \frac{1}{2} P \mid \Lambda \mid P^{-1}(\vec{V}_{si} - \vec{V}_{sj}) \tag{2.38}$$

Again, $\vec{V}_{si}$ refers to the vector of conserved variables and $\vec{F}_i^c$ is the convective flux, both at node i. The characteristic unit normal direction of node i is pointing outwards and refers to the shared face between nodes i and j. Regarding P, it is the matrix of eigenvectors of the flux Jacobian matrix, built using the Roe averaged variables and projected in the $\vec{n}_{ij}$ direction. Lastly, $\mid \Lambda \mid$ is a diagonal matrix composed by the absolute value of the previous Jacobian matrix's eigenvalues.

As a consequence of the upwind space discretisation, Roe a is first-order accurate scheme. However, increased resolutions up to second-order can be achieved by the use of Monotone Upstream-centered Schemes for Conservation Laws (MUSCL) [103] by data reconstruction, although it must be constrained

in order to avoid oscillations [104] (wiggly solutions) via flux limiters. SU^2 has implemented several of them, being the Venkatakrishnan flux limiter [105] the most common used within all available test cases of the software.

Regarding the viscous fluxes using a FVM, flow quantities and their first derivatives must also be computed at the faces of each control volume. The values of the flow variables such as the velocity vector, the dynamic viscosity (μ) and the heat conduction coefficient (k) are obtained from averaging their values at the cell faces. The gradients of the flow variables can be calculated using two different alternatives implemented within the SU^2 code: Green-Gauss or Least-Squares methods.
For flow solutions on quadrilateral mesh elements, the Least-Squares gradients are recommended in order to obtain higher accuracy on the solution [99] and ensures a monotonic solution over the domain. Moreover, regarding the stencil (*i.e.* number of neighbour nodes considered for the interpolations) it implies more flexibility than Green-Gauss. What characterises this method is the consideration of linear variation of the solution field ϕ from one node C to its neighbour F, thus being expressed as

$$\phi_j = \phi_i + (\nabla\phi)_j \cdot (\vec{r}_j - \vec{r}_i) \tag{2.39}$$

where $\vec{r}_{ij} = \vec{r}_j - \vec{r}_i$ is the vector from node i to its neighbour j. In the majority of cases, the cell gradient will not be exact, which means there are more neighbours than number of gradient vector components. The procedure followed by the Least-Square method is computing the gradient by an optimization that finds the minimum of the function G_i

$$G_i = \sum_{k=1}^{NB(i)} \Big(w_k[\phi_{j_k} - (\phi_i + \nabla\phi_i \cdot \vec{r}_{ij_k})] \Big)^2 \tag{2.40}$$

and is minimised by imposing the following conditions:

$$\frac{\partial G_i}{\partial\Big(\frac{\partial\phi}{\partial x}\Big)} = \frac{\partial G_i}{\partial\Big(\frac{\partial\phi}{\partial y}\Big)} = \frac{\partial G_i}{\partial\Big(\frac{\partial\phi}{\partial z}\Big)} = 0 \tag{2.41}$$

where w_k is a weighting factor that solely depends on geometrical parameters and measures the influence of each node onto the calculations. It can be computed as

$$w_k = \frac{1}{(\mid \vec{r}_{j_k} - \vec{r}_i \mid)^n} \tag{2.42}$$

in which n can vary from 1 to greater values. After having obtained the gradients of the flow variables, they are averaged so as to obtain the gradients at the cell faces, where they will be used. However, due to non-orthogonality between the cell grids [99], the computed gradients require the use of a correction in order to reduce the truncation error of the scheme:

$$\nabla\phi \cdot \vec{n} = \frac{\phi_j - \phi_i}{\mid \vec{r}_j - \vec{r}_i \mid}\alpha_f + \frac{1}{2}(\nabla\phi|_i + \nabla\phi|_j) \cdot (\vec{n} - \alpha_f\hat{\vec{r}}_{ij}) \tag{2.43}$$

That is, because of a misalignment between the face normal $\vec{n}$ and the unit vector connecting the nodes

i and j, $\hat{\vec{r}}_{ij}$. Lastly, the factor α_f corresponds to $\alpha_f = \hat{\vec{r}}_{ij} \cdot \vec{n}$.

2.4.2 Temporal Discretisation

Temporal discretisation plays a fundamental role within the present work. Two types of simulations will be undertaken: **steady** and **unsteady**. Steady simulations on the flapped NLR7301 airfoil will be performed in order to be compared to experimental data, as stated in section 2.2. Its purposes are 1: Validation of the present work's computational set-up, and 2: Acquisition of its aerodynamic capabilities (lift and drag coefficients). Parallel to this, another steady simulation will be run considering only the main element NLR7301, which will be used as a flow input for its shape optimisation computation, with the aim of achieving the aforementioned steady aerodynamic coefficients from the flapped configuration. After having obtained the aerodynamic data of the two high-lift configurations to be compared (flapped and morphed NLR7301), unsteady simulations along a certain time-span will be performed in order to obtain the fluctuations in surface pressure distributions of both geometries, an unsteadiness that is only reproduced by unsteady simulations. It is of vital importance for the acoustic formulation of section 2.5.4 in order to calculate their noise contribution, as these are the airframe noise sources considered by the present work's implementation.

Hence, the chosen schemes for the temporal discretisation of the governing equations regarding both steady and unsteady simulations are presented in the following sections.

i. Steady Simulations

The existing methods are classified in two classes: *explicit* and *implicit* methods. An explicit numerical method computes directly the dependent variables through known values. In this case, any discretization operator can be evaluated *ipso facto* on the actual variable values (*i.e.* $R_i(U)$ evaluated at t^n).
On the contrary, an implicit method treats the dependent variables as unknowns leading to a system of equations that must be solved by an iterative algorithm ($R_i(U)$ evaluated at t^{n+1}). Due to the non-linear nature of *CFD* conservation laws, the implicit methods are rather implemented than explicit ones and SU^2 particularly focuses on *Implicit Euler Scheme*. Reasons are due to its implementation simplicity and being unconditionally stable, whereas explicit methods can show some issues in order to maintain stability depending on the chosen time-step [86]. The discretised system is of the form

$$\int_{\Omega_i} \frac{\partial \vec{V_s}}{\partial t} \partial\Omega + R_i(\vec{V_s}) \approx |\Omega_i| \frac{d\vec{V}_{si}}{dt} + R_i(\vec{V_s}) = 0 \qquad \longrightarrow \qquad \frac{|\Omega_i^n|}{\Delta t_i^n} \Delta \vec{V}_{si}^{\,n} = -R_i(\vec{V}_s^{\,n+1}) \tag{2.44}$$

having $\Delta \vec{V}_{si}^{\,n}$ as ($\Delta \vec{V}_{si}^{\,n} = \vec{V}_{si}^{\,n+1} - \vec{V}_{si}^{\,n}$). Since the residuals at time t^{n+1} are of unknown value, a linearisation at t^n is necessary:

$$R_i(\vec{V_s}^{n+1}) = R_i(\vec{V_s}^{n}) + \frac{\partial R_i(\vec{V_s}^{n})}{\partial t}\Delta t_i^n + \mathcal{O}(\Delta t^2) = R_i(\vec{V_s}^{n}) + \sum_{j \in N(i)} \frac{\partial R_i(\vec{V_s}^{n})}{\partial \vec{V}_{sj}}\Delta \vec{V_{sj}}^{n} + \mathcal{O}(\Delta t^2) \quad (2.45)$$

By means of the previous equations, one leads to having the following linear system of which solution is the updated solution:

$$\left(\frac{|\Omega_i|}{\Delta t_i^n}\delta_{ij}\frac{\partial R_i(\vec{V_s}^{n})}{\partial \vec{V}_{sj}}\right) \cdot \Delta \vec{V_{sj}}^{n} = -R_i(\vec{V_s}^{n}) \quad (2.46)$$

where the subscript j refers to a neighbouring cell. Besides the inherent unconditionally stability which the Euler Implicit method provides, the problem must be relaxed by using a certain value of Δt_i^n. The implemented technique by SU^2 is *local-time-stepping*, which allows mesh cell to advance in time at a different local step. Consequently, convergence is accelerated. For such an objective, each local time step calculation requires the estimation of the eigenvalues and first-order approximations to the Jacobian at every node i by means of the Courant-Friedrichs-Lewy number (CFL) and the integrated convective and viscous spectral radius ($\lambda_i^{conv}, \lambda_i^{visc}$) [100]:

$$\Delta t_i = CFL min\Big(\frac{|\Omega_i|}{\lambda_i^{conv}, \lambda_i^{visc}}\Big) \quad (2.47)$$

ii. Unsteady Simulations

The strategy adopted by SU^2 concerning unsteady simulations is the *dual time-stepping method* [106] so that higher order accuracy in time can be reached. The unsteady problem is converted into a steady problem in each physical time step so that all convergence techniques belonging to steady problem simulations can be then applied. The problem attacked by the dual-time stepping approach is of the form

$$\frac{\partial \vec{V_s}}{\partial \tau} + R^*(\vec{V_s}) = 0 \quad (2.48)$$

where

$$R^*(\vec{V_s}) = \frac{3}{2\Delta t}\vec{V_s} + \frac{1}{|\Omega|^{n+1}}\left(R(\vec{V_s}) - \frac{2}{\Delta t}\vec{V_s}^{n}|\Omega|^n + \frac{1}{2\Delta t}\vec{V_s}^{n-1}|\Omega|^{n-1}\right) \quad (2.49)$$

where Δt is the physical time step, τ is a fictitious time used for convergence of the steady problem, $R(\vec{V_s})$ is the residual of the governing equations. Once the steady problem is satisfied, $\vec{V_s} = \vec{V_s}^{n+1}$.

2.5 Aeroacoustics

As the aerodynamics sections are covered, the following section addresses the aeroacoustic part of the present work. It is now necessary first to recapitulate the chief points in the study. At this stage, the computational set-up must have already been validated to guarantee a good description of the flow in both steady and unsteady simulations around the two geometries under study:

$$\textbf{Geometry}_1 = \begin{cases} \textit{NLR7301} \text{ airfoil with Trailing Edge flap} \end{cases} \tag{2.50}$$

$$\textbf{Geometry}_2 = \begin{cases} \text{Morphed } \textit{NLR7301} \text{ airfoil} \end{cases} \tag{2.51}$$

This section is focused on presenting the mathematical formulations that enable to translate the unsteady surface pressure distributions (coming from the aforementioned unsteady simulations) of these geometries, into noise. Firstly, section 2.5.1 goes through the different airfoil self-noise mechanisms, followed by section 2.5.2, which presents the fundamental acoustic analogy of Lighthill, which serves as the starting point for the derivation of the Ffowcs Williams-Hawkings acosutic prediction formulation from section 2.5.3, followed by the derivation of Farassat 1A formulation from section 2.5.4, being in charge of the noise calculations of the present work. Lastly, section 2.5.6 exhibits the post-processing tools that enable the noise contributions to be displayed into a comprehensible manner, thus providing of acoustic readable data ready for comparison.

2.5.1 Airframe Noise Sources

By definition, sound is a pressure oscillation that propagates as a wave of pressure through a medium. At sea level air conditions (*SL*) sound travels at a speed of approximately 340 m/s and is perceived by the human ear if its frequency lays within the audible range, starting at 20 Hz until 20 KHz [107]. Different noise aerodynamic sources from an airfoil arise due to particular flow behaviours, becoming of great interest due to its large contribution to the overall noise of an aircraft at take-off and landing performances, in which airframe noise matches or exceeds the engine noise. Hence, what the next section proceeds with, is the understanding of the aerodynamic phenomenon that create such intense noise sources.

Turbulent-Boundary-Layer-Trailing-Edge (*TBL-TE*) Noise

Regarding an isolated airfoil into a uniform stream at high Reynolds numbers, the nature of the boundary layer becomes mostly turbulent in both the suction and pressure sides along the surface of the airfoil until reaching its trailing edge. It is in this sharp edge location where both turbulent flows convect into the wake and thus originate high pressure fluctuations that emit non-negligible noise [108].

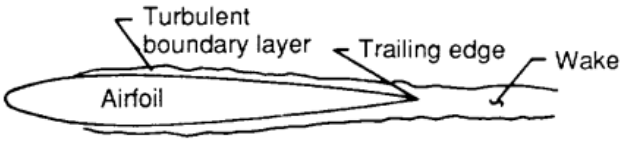

Figure 2.4: *TBL-TE* noise sources [109].

Considering a high lift airfoil geometry composed by two lifting surfaces (the main wing and the flap), reference [49] states that the interaction between elements do not have a considerable impact on the far-field spectrum and noise predictions are within the calculations made for isolated components. However, convected turbulent flow on the flap trailing edge causes the noise levels to be increased with respect to more upstream positions. An interesting work that examines the influence of an incident turbulent flow discharging over a rigid surface of finite extent, show that a strong noise mechanism arises from their interaction [110] and could be strongly related to what reference [49] obtains.

Separation-Stall Noise

When the critical angle of attack of an airfoil is exceeded, separation of the boundary layer occurs at the suction side, the stall condition. This is due to an adverse pressure gradient from the trailing edge towards the leading edge which leads to vortex shedding towards the trailing edge and consequently causing considerable flow instabilities that originate noise [111].

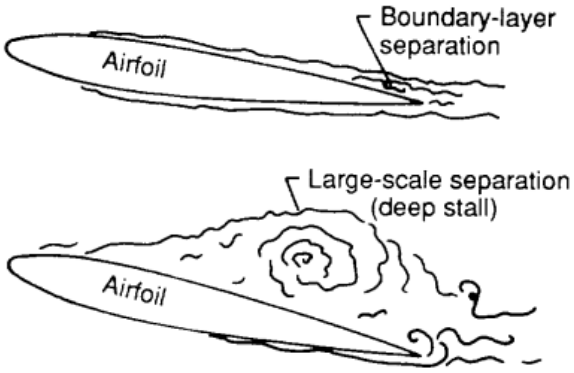

Figure 2.5: Stall noise sources [109].

Laminar-Boundary-Layer-Vortex-Shedding (*LBL-VS*) Noise

Due to an unstable laminar boundary layer on the pressure side of the airfoil, when merging with the boundary layer of the suction side, disturbances in the form of large-scale unstable waves arise causing a vibration of the wake (or loop) and consequently emitting acoustic waves [112]. As long as the disturbances travel downstream, their amplitude also increases.

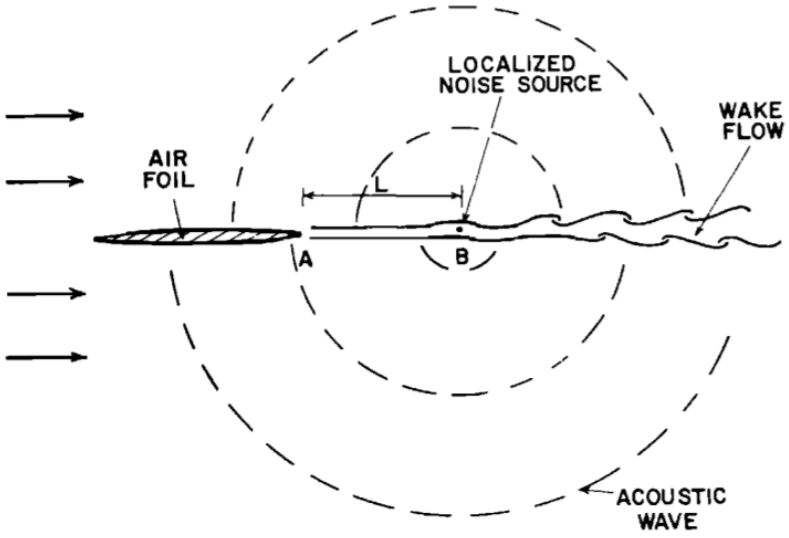

Figure 2.6: *LBL-VS* noise sources [112].

As stated previously, high Reynolds numbers are characteristic from this work, and hence turbulent boundary layers are predominant which means that the contribution of this specific noise will not be relevant.

Tip Vortex Formation Noise

The geometrical discontinuity belonging to the tip of the wing creates a tremendous pressure difference between the pressure and suction sides which leads to the creation of tip vortexes. After propagating along the surface, this turbulence passes over the tip trailing edge and leads to the emission of noise. This phenomenon can be observed in the discontinuity at the tip of the flap section of the wing and has been found to be one of the main sources of airframe noise [28, 29, 42, 47, 113].

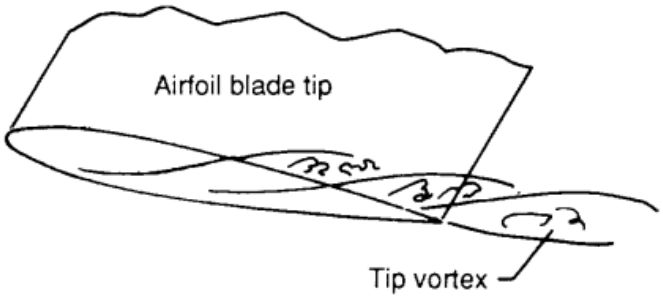

Figure 2.7: Tip Vortex noise sources [109].

Trailing-Edge-Bluntness-Vortex-Shedding Noise

This noise source is a strong geometrical function of the trailing edge bluntness. A blunt shape originates vortex shedding which consequently creates pressure fluctuations that travel with the wake and lead to noise emission.

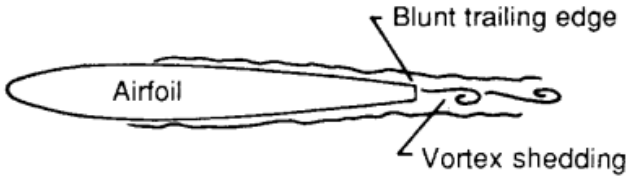

Figure 2.8: Blunt trailing edge noise sources [109].

2.5.2 Airframe Noise Prediction

The aim of airframe noise prediction is, given a fluctuating fluid flow, to estimate the sound radiated from it. For this purpose, there exist different methods to face the problem using analytical solutions, semi-empirical models or acoustic analogy-based methods.

The noise prediction methodology that will be followed in this work is based on acoustic analogy-based methods, as the implemented code to obtain such results belongs to the master thesis [114] which developed an aeroacoustic, analogy-based prediction tool for wind turbine noise (widely introduced in section 3.4). These methods are characterised by first obtaining the flow properties in the simulation domain by computational fluid dynamics methods. Afterwards, these results are fused to an acoustic code that predicts the noise emissions by means of the Lighthill's acoustic analogy [67].

As stated in this reference, the principle of the analogy is the comparison between the equations governing the turbulence or fluctuations of density in the real fluid with the equations belonging to a uniform acoustic medium at rest, whose difference will dictate the noise radiation in a domain with rigid boundaries. In terms of momentum, it is analogous to considering that the momentum contained within a defined spatial region is changing at exactly the same rate as if the gas was at rest under the action of two effects' contributions:

- p_{ij}: Hydrostatic pressure ($p\delta_{ij}$) and viscous stresses,
- $\rho v_i v_j$: Momentum flux tensor or the fluctuating Reynolds stresses (*i.e.* momentum rate in the x_i direction that crosses unit surface area in the x_j direction).

where the second can be understood as an additional stress system to the medium at rest. With respect to the uniform acoustic medium at rest, the only stresses considered would be those belonging to the hydrostatic pressure field ($a_o^2 \rho \delta_{ij}$). Hence, the real density fluctuations would be caused by an external stress system obtained from the difference between the stresses acting on the real flow and the stresses on the uniform acoustic medium:

$$T_{ij} = \rho v_i v_j + p_{ij} - a_o^2 \rho \delta_{ij} \tag{2.52}$$

with T_{ij} and a_o being the Lighthill's stress tensor and the speed of sound, respectively.

2.5.3 The Ffowcs Williams-Hawkings Equation

As an extension to the Lighthill's acoustic analogy and most common used governing equation in acoustic models, is the Ffowcs Williams-Hawkings equation, which now includes a surface in arbitrary motion [31].

So that the aerodynamic sound theory can be built, both mass and momentum equations of a compressible fluid must be considered. However, the validity of these equations are only belonging to the fluid regions outside any closed surface that may be present in the domain. Hence, these equations encounter an inhomogeneity in space. The concept behind the Ffowcs Williams-Hawkings sound theory is to consider a fluid without boundaries in which different regions are considered. These are defined by mathematical surfaces that emulate and match the real ones and so the fluid on and outside these regions behave exactly equally to the real flow. In contrast with the classical equations, an internal fluid motion has been now created inside the closed surface and it is normally specified arbitrarily and simple for simplicity reasons. Consequently, it induces discontinuities in which the internal flow motion does not match the exterior flow on the boundaries and thus makes effective the presence of the surfaces. In order to maintain such discontinuities at the boundaries, mass and momentum sources must be introduced which therefore act like sound generators.

By means of this concept, new mass and momentum conservation equations with sources are able to describe the whole domain (*i.e.* there is homogeneity in space) while handling the discontinuities. The derivation of the resulting Ffowcs Williams-Hawkings equation is handled in [31] giving birth to the expression:

$$\Box^2 p' = \frac{\partial}{\partial t}[\rho_0 v_n \delta(f)] - \frac{\partial}{\partial x_i}[p n_i \delta(f)] + \frac{\partial^2}{\partial x_i \partial x_j}[H(f) T_{ij}] \tag{2.53}$$

This expression introduces several variables and mathematical operators. The wave or D'Alembertian operator in the three dimensional space ($\Box^2 \equiv \nabla^2 - \frac{1}{c^2}\frac{\partial^2}{\partial t^2}$) and p' the acoustic pressure or noise pressure perturbation, also expressed as $p' = c^2(\rho - \rho_0)$, which it is seen how it is due to a density fluctuation. The density in the undisturbed medium ρ_0, the speed of sound c and v_n is the velocity component normal to the surface. With respect to $\delta(f)$ and $H(f)$, these are the Dirac delta and the Heaviside functions, respectively. Both of them are applied to the moving surface described by $f(\vec{x}, t) = 0$ ruled by the condition $\nabla f = \vec{n}$, where $\vec{n}$ is the outward normal direction to the surface. As a consequence, $f > 0$ outside the moving surface and $f < 0$ inside. Figure 2.9 illustrates its geometrical variables.

Lastly, T_{ij} is the Lighthill's-stress tensor (2.52), where its last term can be expressed as

$$T_{ij} = \rho v_i v_j + p_{ij} - c^2(\rho - \rho_0)\delta_{ij}. \tag{2.54}$$

where δ_{ij} is the Kronecker delta.

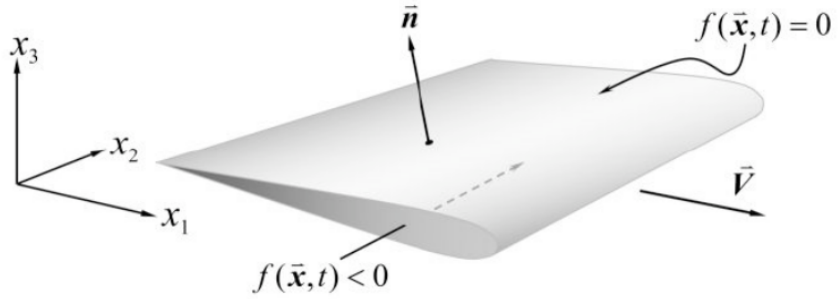

Figure 2.9: Ffowcs Williams-Hawkings' surface definition [115].

It is in equation 2.53 where two notorious noise source terms arise in the form of two wave equations:

$$\Box^2 p'_T = \frac{\partial}{\partial t}[\rho_0 v_n \delta(f)] \tag{2.55}$$

$$\Box^2 p'_L = -\frac{\partial}{\partial x_i}[p n_i \delta(f)] \tag{2.56}$$

Equation 2.55 is the equation of **thickness noise** whereas equation 2.56 is the **loading noise** equation. By definition, thickness noise is caused by the displacement that the surface exerts onto the fluid by its movement, also known as the **monopole** source term, while the loading noise comes from an aerodynamic point of view, which is the acceleration that surface induces to the fluid, or **dipole** term. This term is the contribution of the net force acting on the fluid from the viscous stresses and the pressure distribution along the surface. Concerning the third term of equation (2.53), it is the so called **quadrupole** term due to turbulence.

The acoustic code that is used in this thesis [114] is formulated using a specific solution of Ffowcs Williams-Hawkings equation (2.53), know as *Formulation 1A* developed by F. Farassat, introduced in the following section.

2.5.4 Formulation 1A of Farassat

Farassat's formulation 1A [116] gives a solution for both the thickness and loading noise wave equations above, propagating the pressure fluctuations caused by all terms from equation 2.53, along the continuum medium (atmospheric air) until a certain desired location. However, regarding the quadrupole terms, a Lighthill's general theory extension was implemented by N. Curle [76] which incorporates the influence of solid boundaries upon the sound field. After a dimensional analysis, this showed that dipole sources are more efficient generators of sound in comparison with quadrupoles if the Mach number is within a subsonic regime. Farassat's formulation 1A is neglecting the effect of quadrupole sources for this purpose as well as because of the high computational effort that their calculation would demand. This, together with the fact that all simulations within this work are within a subsonic regime, makes it be in natural agreement.

The formulation allows the observer to be within an arbitrary location and trajectory (or moving-observer). As quadrupoles are neglected, just surface data is needed for noise calculations as both thickness and loading noise are surface's business, thus reducing considerably the computational cost while being fairly robust. Its detailed derivation can be accessed in reference [115] where the total pressure perturbation at the observer's position at a certain time is obtained by the summation of the thickness and loading pressure perturbations, respectively:

$$p'(\vec{x},t) = p'_T(\vec{x},t) + p'_L(\vec{x},t) \tag{2.57}$$

The corresponding solution of these two wave equations proposed by this formulation is as following:

$$4\pi p'_T(\vec{x},t) = \int_{f=0} \left[\frac{\rho_0 \dot{v}_n}{r(1-M_r)^2} + \frac{\rho_0 v_n \hat{r}_i \dot{M}_i}{r(1-M_r)^3} \right]_{ret} dS + \int_{f=0} \left[\frac{\rho_0 c v_n (M_r - M^2)}{r^2(1-M_r)^3} \right]_{ret} dS \tag{2.58}$$

$$4\pi p'_L(\vec{x},t) = \int_{f=0} \left[\frac{\dot{p} cos\theta}{cr(1-M_r)^2} + \frac{\hat{r}_i \dot{M}_i p cos\theta}{cr(1-M_r)^3} \right]_{ret} dS + \int_{f=0} \left[\frac{p(cos\theta - M_i n_i)}{r^2(1-M_r)^2} + \frac{(M_r - M^2) p cos\theta}{r^2(1-M_r)^3} \right]_{ret} dS \tag{2.59}$$

for the thickness and loading perturbations, respectively. The solutions are segregated by near field terms $\left(\text{order } \frac{1}{r^2} \right)$ and far field terms $\left(\text{order } \frac{1}{r} \right)$.

The particularity of this formulation is the introduction of a reference frame $\vec{\eta}$ which is fixed relative to the wing surface. Consequently, the wing can be discretised in panels whose coordinates are expressed within this reference frame so that, via equations (2.58) and (2.59), given a panel physical characteristics, each of their noise contribution can be calculated separately to latter compute the overall. Hence, in order to calculate the perturbations at a certain observer location, two different time discretisations must be undertaken, one belonging to the perturbation emission time of a certain panel and another one for the reception of such perturbation at the observer location. The notation for the first one is the so called *retarded time* $(ret; \tau_e)$. Secondly, the perturbation will travel along the medium at the speed of sound c until reaching the observer's position $(\vec{x})$ at time t. This feature makes Formulation 1A to be classified as a *retarded-time formulation*. The relative position between each emission panel and the observer (or the radiation direction) is denoted by $\vec{r}$. The Mach number of each panel at the emission time in the radiation direction is M_r $(M_r = \vec{M} \cdot \hat{\vec{r}})$, which leads to the definition of the local angle between the normal to the surface and the radiation direction at the emission time, θ. With respect to physical quantities, ρ_0 is the density in the undisturbed air region whereas p is the surface pressure of the panel under consideration whose surface normal and normal velocity are defined by $\vec{n}$ and v_n $(v_n = \vec{v} \cdot \vec{n})$, respectively.

2.5.5 Numerical Integration of Retarded-Time Formulations

So that the integral formulation of equations (2.58) and (2.59) can be solved, a numerical evaluation must be undertaken. As previously stated, Formulation 1A is a retarded-time formulation and there exist several retarded-time algorithms that provide a solution to them.

Retarded-Time formulations face the following generic wave equation:

$$4\pi\phi(\vec{x},t) = \int_{f=0} \left[\frac{Q(\vec{y},\tau)}{r \mid 1 - M_r \mid} \right]_{ret} dS \tag{2.60}$$

where the source strength Q is a function of the source position and time: $Q = Q(\vec{y},\tau)$. The integration of equation (2.60) is evaluated at the emission time: $\tau_e = t - r/c$. Due to the robustness and efficiency of retarded-time formulations, most of noise prediction implementations are using them [117] and will be presented in the following paragraphs.

i. Midpanel Quadrature

This is the most widely used method, which approximates the integral 2.60 as follows:

$$4\pi\phi(\vec{x},t) \approx \sum_{i=1}^{N} \left[\frac{Q(\vec{y}_i, t - r_i/c)}{r_i \mid 1 - M_r \mid_i} \right]_{ret} \Delta S_i \tag{2.61}$$

The procedure is dividing the surface S into N panels and thus evaluating the integrand at each of the panel's centre, $\vec{y}_i$. In order to guarantee enough accuracy to the solution, the panel size must be sufficiently small so that the source strength is approximately linear over the panel so that its midpoint really represents the mean value [117].

ii. High-Accuracy Quadrature

This numerical method acts as a refinement of the previous one (2.61) in the form of the following approach:

$$4\pi\phi(\vec{x},t) \approx \sum_{i=1}^{N} \left(\sum_{j=1}^{n_i} \alpha_j \left[\frac{Q(\vec{y}_j, t - r_j/c)}{r_j \mid 1 - M_r \mid_j} \right]_{ret} \mid J \mid_j \right) \Delta S_i \tag{2.62}$$

What is done in this formulation is replacing the evaluation of the integrand belonging to the Midpanel Quadrature Formulation at the panel centre by adding more points and thus overcoming the limitations of the Midpanel algorithm. The new variables introduced, say α_j and $\mid J \mid$, are the quadrature weight coefficient and the determinant of the Jacobian of the transformation, respectively. By introducing more points, one can play with their location in the panel in order to increase the order of polynomial approximation used for the panel quadrature and hence increasing its accuracy [117].

Another topic that is of great interest is whether considering a ***Source Time-Dominant Algorithm*** or, on the contrary, an ***Observer Time-Dominant Algorithm***. In other words, the first involves selecting an emission time for a certain panel followed by determining when the signal will reach the observer. On the other hand, the latter involves selecting the observer time at first and proceed oppositely.

In case the observer is stationary, then it is simply found analytically:

$$t = \tau + r_i/c \tag{2.63}$$

but if not, then the root of the following expression must be found [115]:

$$t - \tau - \frac{\mid \vec{x}(t) - \vec{y}(\tau) \mid}{c} = 0 \tag{2.64}$$

Considering that the motion of the observer is usually simple, most of the times t is found analytically and hence easily. However, a sequence of source times leads to unequally spaced observer times. That means that, in order to obtain the contribution of all panels at a certain observer time, an interpolation in time must be undertaken in the form of

$$4\pi\phi(\vec{x}, t^*) \approx \sum_{i=1}^{N} \mathbf{I}[K_i(t), t^*] \tag{2.65}$$

in which appears an interpolation operator ($\mathbf{I}[, t^*]$) and t^* which is the desired observer time for computing the perturbations. Moreover, the approximation integral over the panel K is defined as

$$K_i(t) = \frac{Q(\vec{y}, \tau)}{r_i \mid 1 - M_r \mid_i} \Delta S_i \tag{2.66}$$

In favour of the source-dominant algorithm, if aerodynamic input data is provided, emission times and geometry of the wing are known (*i.e.* $\vec{y}, \tau$), hence directly determining t^* and avoiding interpolations on the input data.

To sum up, table 2.2 summarises the chosen methods:

Time-Dominant Algorithm	Source
Noise prediction implementation	Mid panel Quadrature

Table 2.2: Chosen methodology for Retarded-Time Formulation used in [114].

2.5.6 Noise Signal Post-Processing

Having reached the present section means that all necessary tools for generating acoustic data from aerodynamic data have been presented. The only matter that remains to explain are the post-processing procedures to elaborate easily understandable noise mappings, to latter being analysed. Farassat 1A gives the acoustic pressure signal at a certain observer's location, in which noise levels are obtained.

The following tools, which are the Fast Fourier Transform (FFT) and One-Third Octave Bands, are in charge of converting such signal.

Fast Fourier Transform (FFT)

The Fourier Transform decomposition states that any continuous periodic signal can be represented by the sum of different sinusoidal waves [118]. The acoustic pressure signal from Farassat 1A is stored at discrete time steps in a finite time length within the time domain. Decomposition by the Discrete Fourier Transform (DFT) decomposes it to obtain its frequency spectrum, and so obtaining information of the sinusoids within the signal regarding frequency, phase, and amplitude. Consequently, the information is said to be in the **frequency domain** and provide information about each of the frequencies' noise contribution. The corresponding expression of the DFT is as following:

$$X(k) = \sum_{n=0}^{N-1} x(n) W_n^{kn} = \sum_{n=0}^{N-1} x(n) e^{-j\frac{2\pi kn}{N}} \quad , \quad k \in [0, N-1] \tag{2.67}$$

where X is the signal in the frequency domain after the transformation, N the number of samples and x the original discrete signal belonging to the time domain.

However, the calculating speed of DFT is not very competitive. Fortunately, there are ways of speeding the process up. The most relevant one is the **Fast Fourier Transform**, which provides as accurate results as the other methods with an added value: reducing the computational time dramatically [118]. The execution time for DFT and FFT are, respectively:

$$t_{DFT} = k_{DFT} N^2, \tag{2.68}$$

$$t_{FFT} = k_{FFT} N log_2 N. \tag{2.69}$$

It is visible at first sight, besides the proportionality constants (k_{DFT}, k_{FFT}) how the order of magnitude from FFT is lower than DFT's. Figure 2.10 illustrates the FFT transformation applied onto the acoustic pressure signal from a validation case of a NACA 0018, which will be introduced later in section 3.4.

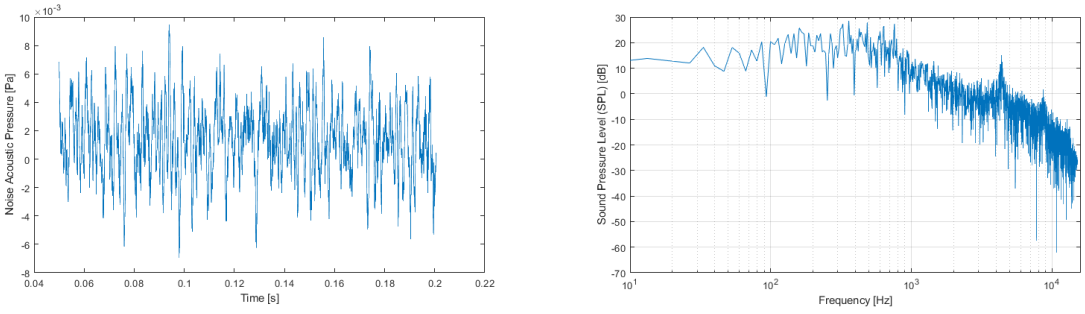

Figure 2.10: Total noise acoustic signal (left) and FFT frequency spectrum (right) from the Data obtained by TU Delft [119].

The original acoustic pressure signal is expressed in Pascal (Pa) units. After applying the FFT transformation and thus jumping onto the frequency domain, the frequency spectrum arises (figure 2.10), where each of the frequencies within the input signal comes with an assigned amplitude of its noise contribution, the **Sound Pressure Level** (SPL). It is expressed on a logarithmic scale where the units are decibels (dB):

$$SPL(dB) = 20log\left[\frac{p}{p_{ref}}\right] \tag{2.70}$$

in which p is the pressure value in Pascals, and the reference pressure being ($p_{ref} = 2 \cdot 10^{-5}$ Pa), which is a human ear threshold, corresponding to zero decibels.

One-Third Octave Bands

One third octave bands are frequencies defined by splitting the continuum frequency spectrum into a set of frequency bands (see Appendix B) to allow a compression of the information displayed, and so making it more easily readable in comparison with the frequency spectrum (figure 2.10). Each of the bands is characterised by its middle frequency (f_c) and its lower and upper frequency limits (f_l, f_u), which are defined as

$$f_c = \sqrt{f_u \cdot f_l}, \tag{2.71}$$

$$f_l = f_c/2^{1/6} \quad , \quad f_u = 2^{1/6} f_c \tag{2.72}$$

leading to the relation between the upper and lower band frequency limits:

$$f_u = 2^{1/3} f_l. \tag{2.73}$$

The SPL values related to each frequency of the continuum spectrum must be added to the corresponding one third octave bands so that the total SPL at each band is obtained. In order to do so, each contribution cannot be added as a conventional summation due to begin expressed in a logarithmic scale, hence

$$SPL_T = 10log\Big(\sum_k 10^{\frac{SPL_k}{10}}\Big), \tag{2.74}$$

where the subscript k refers to each of the frequencies within the considered band. Furthermore, if one needs the compute the total energy contained in the spectrum, the **Overall Sound Pressure Level** (OASPL) is computed:

$$OASPL = 10log\Big(\sum_k 10^{\frac{SPL_{f_i}}{10}}\Big), \tag{2.75}$$

in which the sound pressure levels of each of the one-third octaves bands are summed. Figure 2.11

shows the one-third octave bands obtained from the acoustic pressure signal in the frequency domain (figure 2.10):

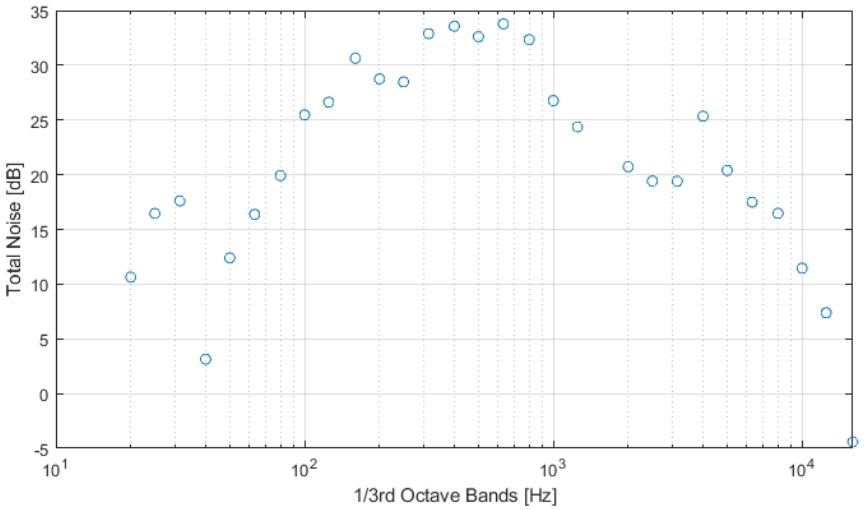

Figure 2.11: Acoustic pressure one-third octave bands from acoustic data from TU Delft.

By means of these processing tools, the noise levels from both the flapped and the morphed NLR7301 can be compared.

Chapter 3

Methodology

Chapter 2 has presented the mathematical background to describe the behaviour of a flow, going from the RANS equations, to their numerical discretisation by means of the Finite Volume Method (FVM), together with the turbulence model Spalart-Allmaras, all within a well defined domain ruled by proper boundary conditions, and discretised in several volumes of control in where to apply the governing flow equations. Within the present chapter, section 3.1 is dedicated to explain which software are in charge to apply such tools. At first, section 3.1.1 presents the SU^2 open-source software, which will perform the flow analysis for both steady and unsteady simulations, as well as the airfoil shape optimisation design. Afterwards, section 3.1.2 introduces the PointWise software, used to built the domain's mesh, followed by section 3.1.3, presenting the Paraview open-source software, which allows to visualise the flow results, used to enrich the post-processing analysis. Section 3.2 introduces a detailed description of the high-lift configuration test case: NLR7301 with trailing edge flap, which will be used to validate the computational implementation developed in this thesis, as well as to obtain its aerodynamic capabilities regarding lift and drag coefficients. Subsequently, it is within section 3.3, where the shape optimisation design steps of the NLR7301 airfoil will be presented to achieve a maximisation of its lift, up to the flapped configuration one. Lastly, the implementation of the Farassat 1A acoustic framework is presented, followed by introducing a NACA 0018 test case, that will prove the acoustic code's validity, so that reliable noise level calculations for both flapped and morphed NLR7301 airfoils are guaranteed.

3.1 Software Description

3.1.1 Flow Solver

Stanford University Unstructured (SU^2) [100] is an open-source, computational analysis and design software in constant development by the Aerospace Design Laboratory (ADL) at Stanford University (its original developer) and the world's community. It is incorporated with a collection of C++ software tools to discretise and solve Partial Differential Equation-based (PDE) problems as well as PDE-constrained optimisation problems. Although the software has been designed to face Computational Fluid Dynamics (CFD) and aerodynamic shape optimisation, its functionality goes beyond to other governing equations, such as the wave equation. As an important fact, the aim of the active development is the integration and coupling of different physical problems into one multi-disciplinary solver, so that the problem analysis and its outcome optimisation can be achieved easily. To do so, the different software modules of SU^2 are coupled using several Python scripts, thus more complex analysis and design procedures are performed. Last but not least, a common feature of all modules is that they share the same C++ class structure, consequently lowering the effort of the coding coupling and allowing, for example, mesh deformation capabilities to be integrated into the flow solver. Here lies the potential of SU^2.

The most important tools that will be used within the computational simulations are the following:

- **SU2_CFD**: This code solves all the necessary problems that are fulfilled in the present work, concerning both steady and unsteady solutions of the direct and adjoint problems by means of the RANS equations. A competitive feature is its availability to be run in parallel using a Message Passing Interface (MPI), speeding up the time-consuming simulations. OpenMPI is a freely accessible implementation and hence used. The python script that is in charge of computing parallel analysis on multi-core jobs is *parallelcomputation.py*;

- **SU2_AD**: Performs the adjoint flow simulations by means of automatic differentiation (AD). The strategy to be followed is gradient-based optimisation. Gradients of the objective function to be minimised will be calculated by adjoint methods. More specifically, the discrete adjoint method [120, 121] (introduced in section 3.3), will be chosen for the geometry optimisation, executed by SciPy's library sequential least squares programming (SLSQP) optimizer algorithm;

- **SU2_DOT**: Computes the gradient of the objective function by projecting the surface sensitivities into the design space of the optimisation job. The Python script that dictates the shape optimisation procedure is *shape_optimization.py*;

- **SU2_DEF**: Deforms both the airfoil geometry and the mesh during an optimisation job, which is also ruled by the *shape_optimization.py* Python script.

3.1.2 Mesh Generation

A crucial preprocessing step is the generation of a geometrical framework: the domain's mesh. This process divides the continuous domain into non-overlapping elements or cells delimited by their corresponding faces. It is within this primal mesh where the finite volume method with dual-grid (section 2.4.1) will be applied to latter solve the governing equations.

The generic characteristics that must be suited by a mesh for it to provide a proper spatial discretisation of the domain, and so to achieve a reasonable level of accuracy in the flow solution, are the following:

- **Skewness**: A fundamental mesh quality measure. Skewness provides information about how close a cell is to the ideal cell (*i.e.* equilateral or equiangular). A value above 0.75 defines a poor quality mesh, while a skewness below this value can be considered as fair. In general, a value closer to 0 will always imply a better mesh quality.

- **Continuity**: Continuity refers to two important aspects. The first one is related to grid spacing. In order to guarantee a proper translation of the information from cell to cell or conservation of fluxes (by means of the cell gradient), the cell dimensions between two adjacent cells must not abruptly differ. On the other hand, grid line continuity must also be guaranteed so that non-orthogonality errors are reduced as much as possible.

- **Alignment with the flow**: In critical domain regions such as the boundary layer or wakes, the flow properties must be well captured and translated downwards due to their crucial influence onto the aerodynamic coefficients and the skin friction. Among others, the final solution will strongly depend on how the flow perturbation dissipates towards the boundaries through the wake. For that, guaranteeing cell alignment with the flow avoids major non-orthogonality errors and its proper follow-up in downwards direction so that dissipation is properly described. Moreover, this is also traduced to a better solution convergence.

- **Resolution**: In order to capture all physical length scales in the flow (from small scales as the boundary layer to larger scales as flow vortices), sufficient grid resolution must be implemented.

- **Dimensionless wall-distance** (y^+): This value is related to mesh spacing at the airfoil boundary. It gives information about the mesh quality near the walls, hence within the boundary layer. Spalart-Allmaras turbulence model requires a $y^+ < 1$ so that all viscous effects are well captured.

Many papers have faced this grid generation problem on a multi-element airfoil configuration [91, 122–126]. The most used strategy is the multi-block mesh with quadrilateral elements aligned with the flow. The overall nature of the mesh is considered unstructured due to the existence of cells with different number of neighbours with respect to other quadrilateral cells, more specifically on the boundaries of each block. This allows more mesh adaptability to complex geometries and local refinement, being penalised by the need to define local connectivity between cells, which adds computational complexity. However,

structured local regions are predominant in the whole domain. Structured cells are surrounded by the same number of neighbours, hence easing their localisation. Resulting locally near-1D flow means numerical diffusion can be reduced (*i.e.* better accuracy is achieved [99, 127]). Figure 3.1 illustrates how a multi-block mesh is built:

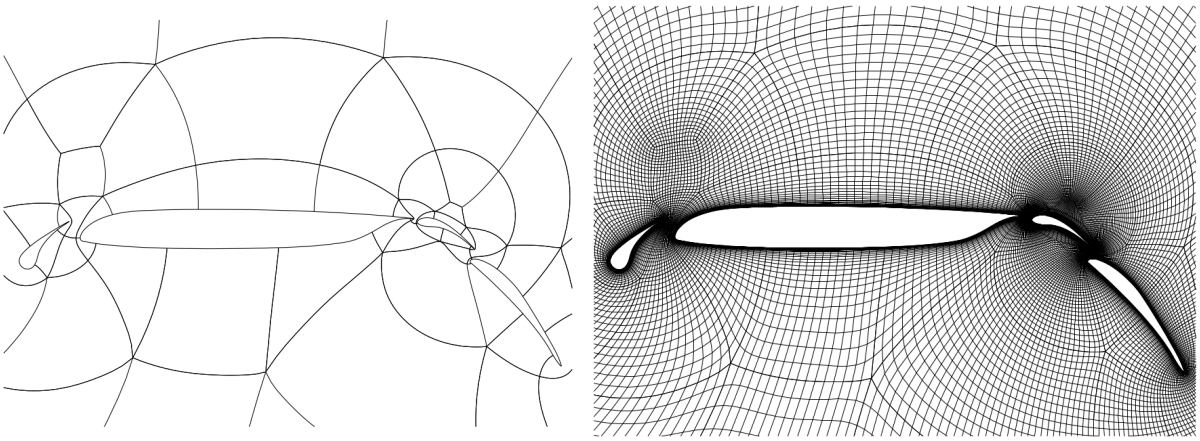

Figure 3.1: Mesh blocks and the resulting mesh on a multi-element airfoil configuration [127].

3.1.3 Flow Visualisation Tool

Once the results are obtained, huge data files are generated containing all the flow properties on the computational domain. In order for us to visualise it, the open-source visualisation tool Paraview 5.5.0 available for the current Ubuntu operative system 16.04 LTS is used. Its entry format is an output format from SU^2: *.vtk*.

3.2 Computational Fluid Dynamics: Steady Simulations Set-up

This section is exclusively dedicated to show the procedure from the mesh generation until the accomplishment of the desired aerodynamic results, following the design flow illustrated in figure 3.2:

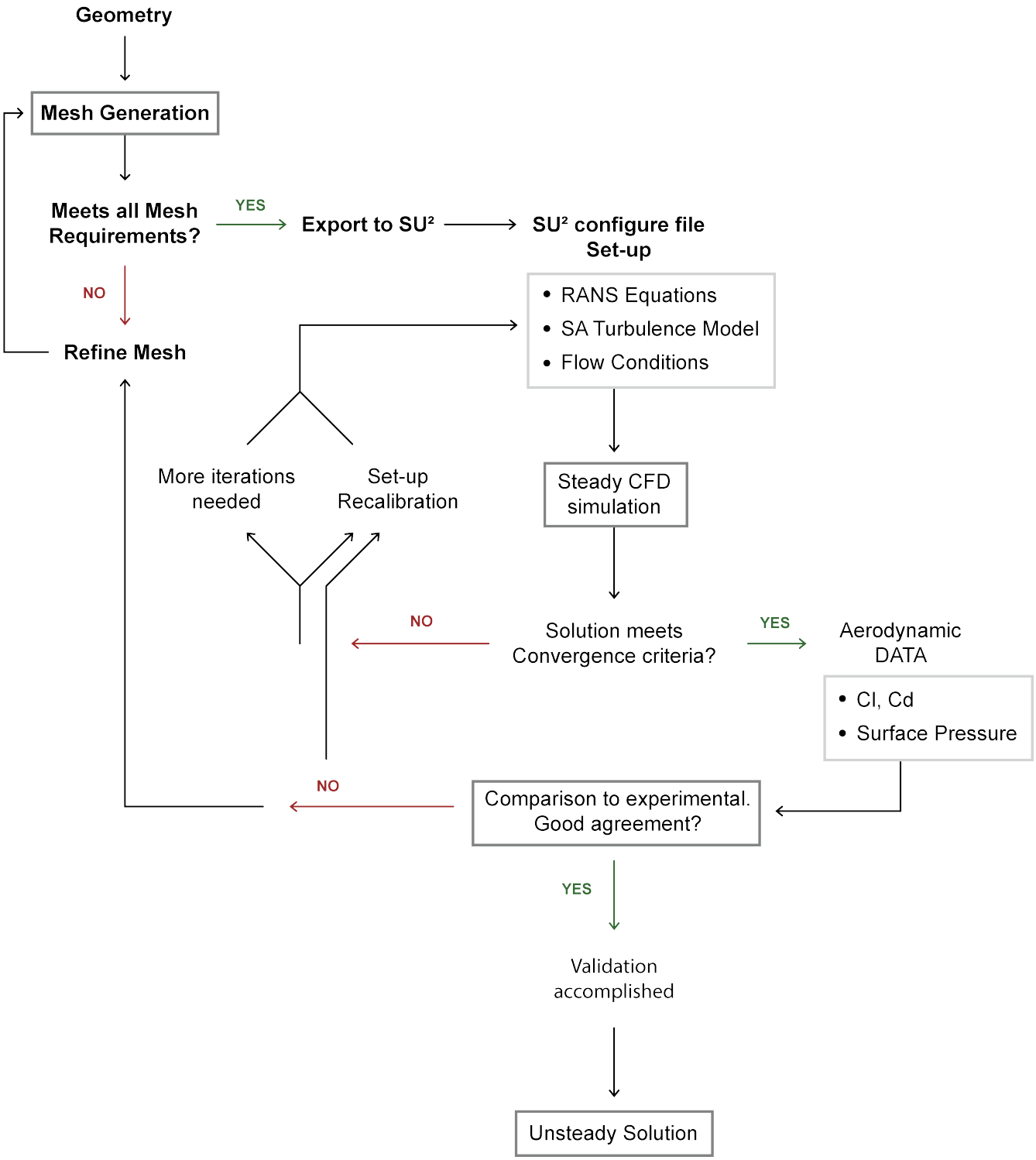

Figure 3.2: Procedure flow chart for the steady CFD simulations.

As it has previously been explained, the first step that must be undertaken is the discretisation of the physical space by means of a mesh, using the PointWise mesh software. Before being exported to SU^2 flow solver, the mesh generation will be under a design-loop until all quality requirements from section 3.1.2 are fulfilled. It is then when it can be exported to SU^2, and the computational set-up within its flow solver scripts is defined, choosing the physical problem by means of the RANS equations and turbulence model, as well as calibrating the available parameters for each spatial and temporal discretisation schemes, in order to adjust them to our problem. With all set-up done, the CFD steady simulation will be run until matching the established convergence criteria to subsequently compare the resulting aerodynamic data (**lift** and **drag coefficients**, and **surface pressure distribution**) against experimental results. For the present work, close agreement to experimental is chased, meaning that the whole process is within a general design-loop, where recalibration of the parameters of the numerical schemes, or even further refinement of the mesh, will be carried out until acceptable margins between computational and experimental results are reached. In that case, this thesis' CFD model can be considered as valid for further analysis regarding: Unsteady and Shape Optimisation Design simulations.

3.2.1 Validation Case: NLR7301 Airfoil with Trailing Edge Flap

Geometry Description

The present work will be focused on the NLR7301 supercritical[1] airfoil with a trailing edge flap. Due to being tested at take-off and landing flow conditions, plus the existing wide available comparative data, it has shown to be a potential candidate which fulfils this work's aim. As stated in section 2.2, the National Aerospace Laboratory (NLR) has developed wind tunnel tests [96] on this particular two-dimensional, high-lift configuration, shown in figure 3.3. Its coordinates have been obtained from [97].

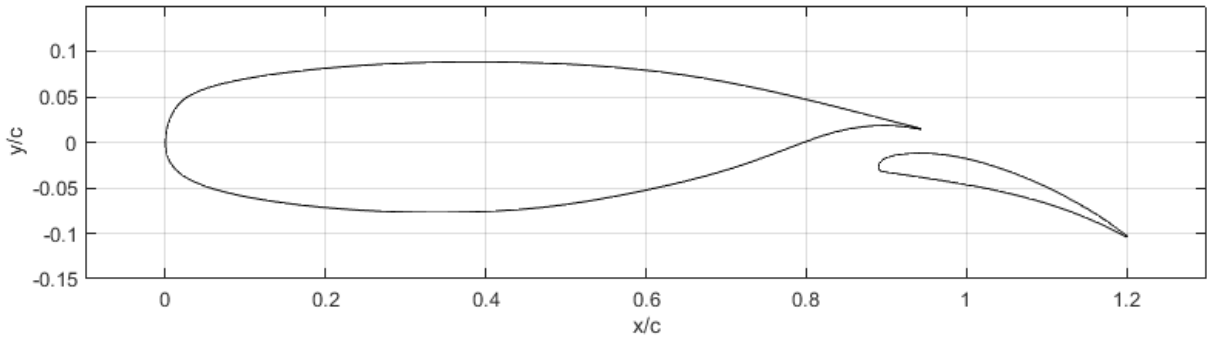

Figure 3.3: NLR7301 Airfoil with trailing edge flap deflected 20° .

The dimensions of the flap with respect to the main element's chord, are $c_f = 32\%c$, and is deflected $\delta_f = 20°$. Lastly, the existing gap width between the two elements is, also expressed with respect to the main element's chord, $gw = 2.6\%c$.

[1] A supercritical airfoil is designed to delay the formation of a supersonic shock wave in the transonic regime.

Experimental Flow Conditions

The flow conditions, concerning Reynolds and Mach numbers, that characterise these tests are summarised in table 3.1:

Reynolds, (Re)	$2.51 \cdot 10^6$
Mach (M)	0.185

Table 3.1: Flapped NLR7301 experimental flow conditions performed by [96].

As noticeable, tests were performed at a subsonic Mach speed, at fairly high Reynolds number regime conditions, which match those of take-off and landing performances. The geometry was so designed that the flow is fully attached (despite of a laminar small separation bubble on the wing nose) for the set of angles of attack in which it was tested, going from zero up to beyond stall, at an angle of attack increment of $\Delta\alpha(^\circ) = 1^\circ$. More extensive data has been presented in [96] for the angles of attack: 6.0°, 10.1°, and 13.1°, for which aerodynamic coefficients (lift and drag), surface pressure distributions, transition positions, and extent and position of the laminar separation bubble have been exhibited.

Regarding the aforementioned angles of attack, even on the limit case of $\alpha = 13.1^\circ$, the flow is still fully attached. However, it is not far from the critical angle of attack for which stall conditions begin to occur ($\alpha \approx 14^\circ$). For this reason, some **retrospective thinking must be done**:

Let us consider the flapped NLR7301 configuration and its inherit physics. Taking out of the equation the aeroacoustic noise penalties within the gap between the main element and the flap [26–29], it supplies a beneficial aerodynamic effect. Here, the flow is accelerated, and consequently energises the boundary layer on the suction side of the flap. This increase in kinetic energy comes to be beneficial, as it leads to a delay of the boundary layer separation and thus enlarging its performance range (*i.e.* no loss of lift due to stalled conditions at high angles of attack). This reasoning is strictly related to the subsequent step of the present work, which implies the NLR7301 design optimisation, morphing its shape in order to accomplish the maximum lift coefficient from the equivalent conventional flapped configuration. In this case, there is no existing gap, and consequently this aerodynamic benefit vanishes.

It is, as a result, reasonable to think that, at limit angles of attack such as 13.1° and without such feature, a hypothetical stall condition on the trailing edge of the morphing airfoil may arise. This, together with the fact that landing performances do not reach such high angles of attack (typically operating around 4° [91]), in addition to typical take-off angles of attack ranging from 10° to 13°, this case will be dismissed in order to consider a more conservative and equally valid case, with the aim of avoiding deep stall conditions on the morphing airfoil: $\alpha = 10.1^\circ$.

Eventually, following this reasoning, the experimental coefficients regarding the flapped NLR7301 high-lift configuration at an angle of attack of 10.1°, immersed in the aforementioned flow characteristics are

exposed in table 3.2:

c_l	2.877
c_d	0.0567

Table 3.2: Flapped NLR7301 Experimental Aerodynamic coefficients at $\alpha = 10.1°$.

In parallel, the experimental surface pressure distribution corresponding to these conditions are displayed in figure 3.4:

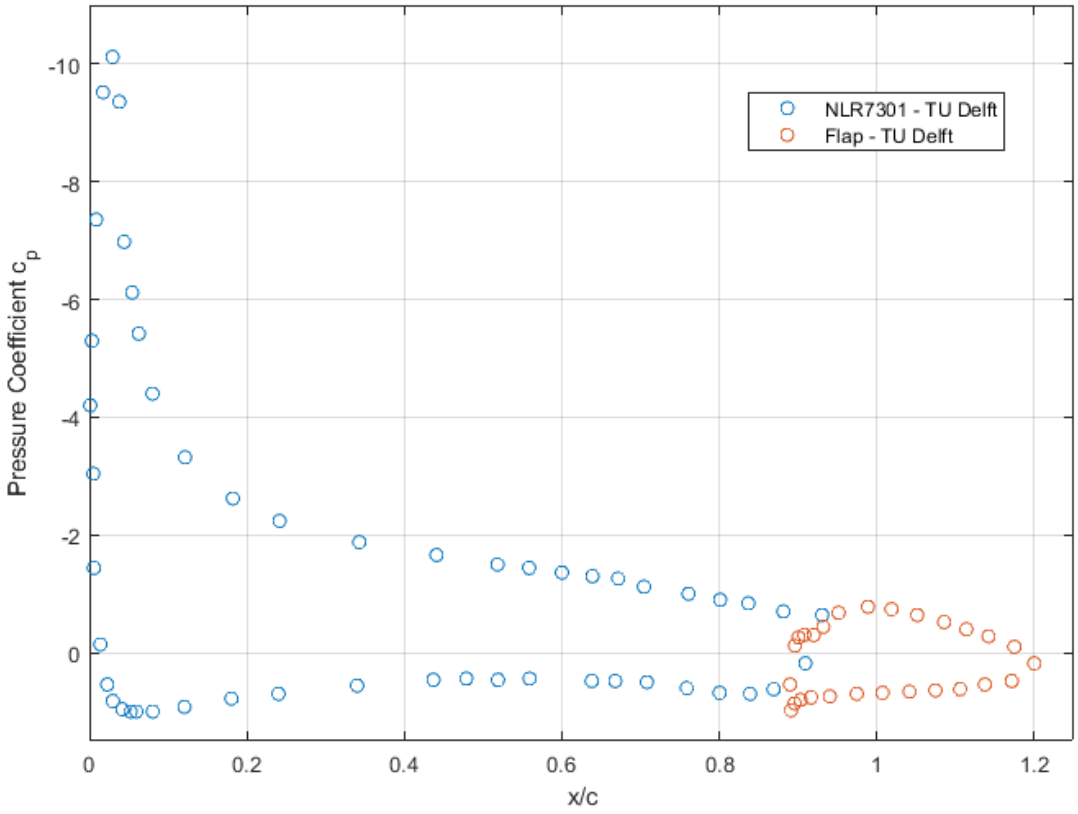

Figure 3.4: Flapped NLR7301 experimental surface pressure distribution at $\alpha = 10.1°$.

Hence, these are the targets of the steady simulation that will validate the CFD implementation of this work. Moreover, the obtained results can also be compared to a Master Thesis developed at the very TU Delft University, in which the same case was performed [97].

Present Work's Computational Set-up

The subsequent Computational Fluid Dynamics simulations are undertaken considering International Standard Atmosphere (ISA) *Sea Level Conditions (SL)*, which strictly define the atmospheric air properties for its worldwide unified use, hence easing the unification and comparison of results undertaken at

any location of the globe:

Density (ρ_∞)	$1.225\ \frac{Kg}{m^3}$
Temperature (T_∞)	$288.15\ K$
Static Pressure (P_∞)	$101325\ Pa$
Viscosity (μ_∞)	$1.8 \cdot 10^{-5}\ \frac{Kg}{m \cdot s}$

Table 3.3: Atmospheric air Sea Level conditions.

The Mach number will be that of the experimental test case, $M = 0.185$, which together with the velocity of sound at the previous SL conditions, using the adiabatic index (γ), and the universal gas constant (R):

$$a_o = \sqrt{\gamma RT} = \sqrt{1.4 \cdot 287\,\frac{J}{Kg\,K} \cdot 288.15\,K} \cong 340\,m/s \tag{3.1}$$

leading to a velocity of

$$M = \frac{U_\infty}{a_o} \quad \longrightarrow \quad U_\infty = M \cdot a_o = 0.185 \cdot 340 \cong 63\,\frac{m}{s} \tag{3.2}$$

Consequently, if a unit reference chord is taken, the corresponding Reynolds number is computed as

$$Re = \frac{\rho_\infty U_\infty c}{\mu_\infty} = \frac{1.225 \cdot 63 \cdot 1}{1.8 \cdot 10^{-5}} = 4.3 \cdot 10^6 \tag{3.3}$$

slightly differing from the experimental ($Re = 2.51 \cdot 10^6$). However, it is not expected to have a major influence on the results as it does not on the surface pressure distribution along both airfoil and flap obtained by [97], using $Re = 4 \cdot 10^6$.

The proper flow solver set-up for this steady simulations is implemented with all capabilities stated in section 2. Reynolds-Averaged Navier-stokes equations (section 2.1.1) will be describing the flow behaviour, accompanied by the one-equation Spalart-Allmaras turbulence model (section 2.2) to guarantee the system of equations' closure and a proper description of the turbulent boundary layer. The upwind flux-difference-splitting scheme by *Roe* will perform the discretisation of the convective fluxes, together with Monotone Upstream-Centred Schemes for Conservation Laws (MUSCL) for second-order accuracy in the spatial domain (section 2.4.1), constrained by the Venkatakrishnan flux limiter to avoid oscillations in the solution (or *wiggle* solutions). With respect to the viscous fluxes, they are implemented by means of the Least-Squares method (section 2.4.1). Regarding the time domain, the discretisation will be undertaken by the Euler Implicit Scheme (section 2.4.2). Lastly, the boundary conditions applied onto the domain's boundaries are defined as section 2.3:

$$\text{Airfoil } (S) = \begin{cases} \textbf{No-slip condition} : \vec{U}_S = \vec{0}; \\ \textbf{Adiabatic} : \left(\frac{\partial T}{\partial n}\right)_s = 0; \end{cases} \tag{3.4}$$

$$\text{Far-field } (\Gamma_\infty) = \begin{cases} \textbf{Free-stream state variables} : \vec{V_s}|_{\Gamma_\infty} = \vec{V_s}|_\infty. \end{cases} \tag{3.5}$$

3.2.2 NLR7301 with Flap: Mesh Implementation

During the development of the previous sections, insistence has been put on the importance of how the domain has to be discretised by means of a mesh, for a good coupling between the computational formulations and where are to be applied is determining the accuracy of the final results. Regarding the case within this section, which is the flapped configuration of the NLR7301 airfoil, attention must be paid on several important regions, name

- **Boundary Layers**: The velocity gradients on the airfoil surface are produced by important shear stresses caused by the viscosity effects, happening at small scales that aim fine mesh resolution to be captured. For high Reynolds numbers as $4.3 \cdot 10^6$, the boundary layer becomes turbulent, a feature that is reproduced by the Spalart-Allmaras turbulence model. Hence, for proper flow description, it is necessary to ensure high resolution on these regions (*i.e.* $y^+ < 1$). Moreover, the aeroacoustic section is focusing on the surface pressure distribution, adding importance to the need of high resolution on the very surfaces.

- **Flow interactions between the two elements**: The trailing edge of the main element is discharging turbulent airflow towards the suction side of the flap. As this may cause instabilities on the flap boundary layer, refinement must be guaranteed to capture such feature. In addition, the gap between the main element and the flap is also of significant sensitivity. Firstly, the inlet section joins the boundary layer of the main element with the gap incoming flow. Here the flow is accelerated by the flap's leading edge, creating a wall jet [128] at its outlet region where it is mixed with the trailing edge turbulent wake from the main element, as well as the boundary layer from the suction side of the flap altogether.

- **Wakes**: The overall wake of the whole configuration must be well-captured in downstream direction, for a proper description of the perturbation's dissipation, as within a subsonic regime, its perturbation also propagates in upstream direction, influencing the solution directly on the surfaces.

With this in mind, the first step is placing an adequate number of nodes on the surfaces that will enable the creation of the boundary layer meshes. Nodes are clustered in both main and flap elements' leading edges, so as to capture the high flow acceleration that is originated (left figure from figure 3.5). Regarding their trailing edges[2], another node clustering is needed to capture the wake mixing flow coming from pressure and suction sides (right figure from figure 3.5). Lastly, regarding the gap region, another high concentration of nodes has been placed (figure 3.6). As a result, the implemented surface nodes are:

Element	***Surface nodes***
NLR7301	498
Flap	492

Table 3.4: Nodes discretisation on the airfoil and flap surfaces.

[2]The trailing edges of both elements have been rounded using SolidWorks [129], thanks to its versatility in splines design. Afterwards, the geometry is importable to PointWise through *.igs* format.

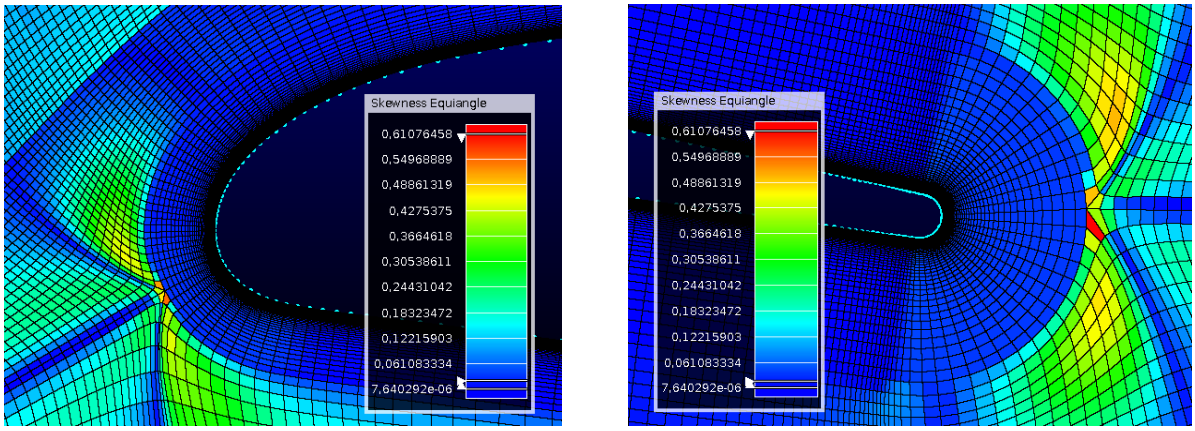

Figure 3.5: Skewness mapping of the flap's leading edge (left) and main element's trailing edge (right).

The boundary layers of the two elements are created by algebraic extrusion of quadrilateral elements on each of the surface's normal directions, with a wall grid-spacing of $1 \cdot 10^{-6} c$ and a growth rate of 1.05, which guarantees what the Spalart-Allmaras turbulence model requires: $y^+ \leq 1$, so that viscous effects are well captured (previous tests with a value of $1 \cdot 10^{-5} c$ were not satisfying it), in addition to ensuring cell alignment with the boundary layer flow and grid smoothness in the vertical direction. Taking advantage of these plots, the skewness values have also been displayed. It is observable that just a unique cell regarding the trailing edge of the main element is reaching the highest value of skewness: ≈ 0.61, in the junction between the two mesh domains, surrounded by cells with a skewness value around ≈ 0.36, whereas the rest of the domain's skewness is below ≈ 0.1. According to this and the quality criteria established in section 3.1.2, the mesh is considered to not compromise its quality in terms of skewness.

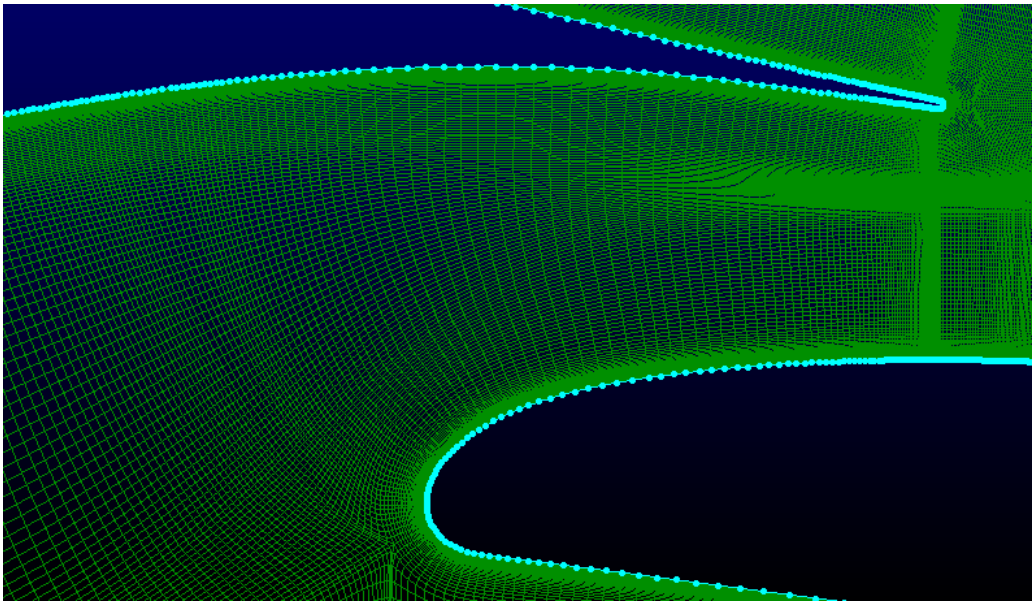

Figure 3.6: Mesh structure on the gap region between the main and flap elements.

The gap mesh shown in figure 3.6 illustrates how the node clustering belonging to both surfaces is dis-

tributed, and smoothly interconnected within this region. It is visually clear that it has been built so as to follow the air motion from inlet to outlet sections, thus chasing the aforementioned flow alignment. In order to create this second mesh in the outer regions of the boundary layers, several connectors have been built using SolidWorks' capabilities, in order to generate three zones within the domain similarly to the procedure followed by [123]: Upper, lower, and inner zones, as illustrated in figure 3.7:

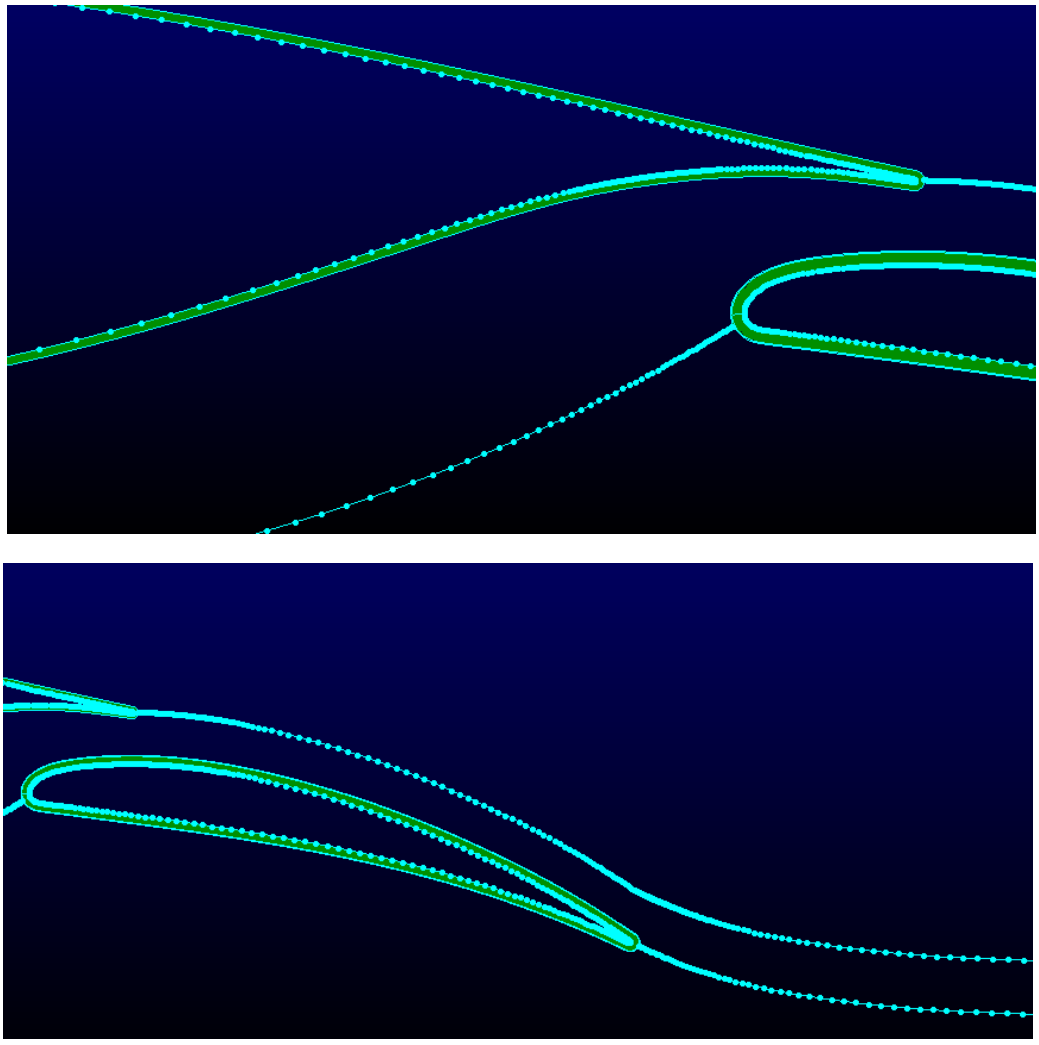

Figure 3.7: Multi-zonal mesh created by several connectors.

The connectors are equipped with nodes that are clustered towards the intersection with the boundary layer meshes. The adjacent cells belonging to the two different meshes are dimensionally equalised. This way, cell continuity is ensured. The inner mesh is built by discretising it in several partitions in downstream direction, to afterwards be filled manually with quadrilateral cells. This procedure has been necessary to calibrate the nodes clustering at each of the partitions in order to smoothly interconnect the upper and lower walls. The connector on the flap's trailing edge is extended up to the limits of the computational domain, matching the real direction of the wake. This has been done by previous coarser analysis in which to obtain the wake's direction to finally direct the connector towards it. The objective of doing so, is to generate a refined region on the wake to capture all its flow features.

Once the inner zone has been properly meshed, both the lower and upper zones are meshed using a hyperbolic extrusion with a growth rate of 1.1, filling the mesh domain up to 14 chord lengths after the flap trailing edge, and 10 chord lengths towards the upper, lower and upstream directions. Consequently, the mesh is of C-type, as illustrated in figure 3.8:

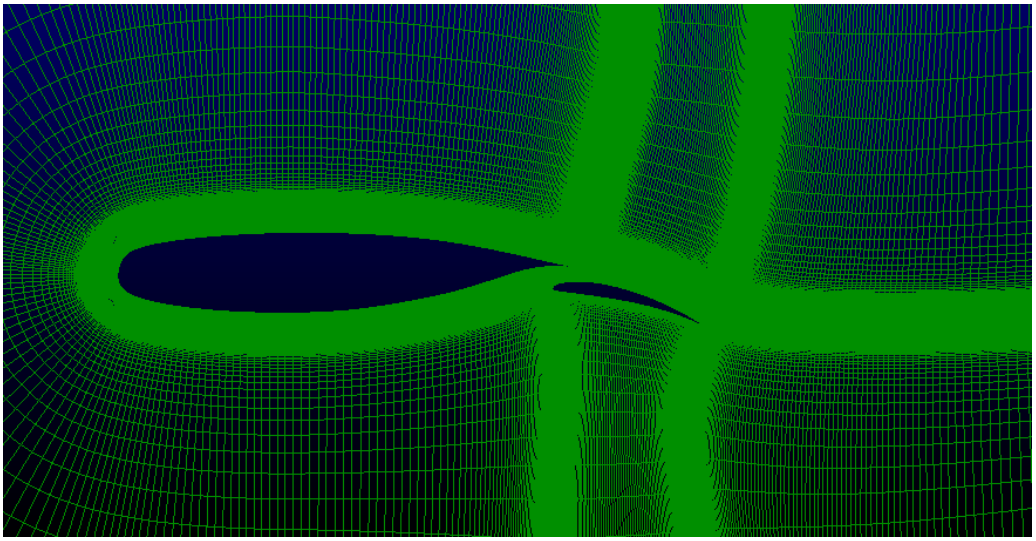

Figure 3.8: C-mesh topology for the flapped NLR7301.

From figure 3.8, it can be observed that highly refined areas are set on the boundary layers and the gap. Moreover, the existence of a wide refined area on the flap's suction side provides accurate resolution on the interaction of the wall jet from the gap region, the main element trailing edge's wake, and the flap's boundary layer, all convecting towards the flap's trailing edge, where the overall wake is followed towards its real direction.

With respect to the total nodes number that have been necessary, a comparative table with values from the present and other works concerning high-lift configurations is displayed. As a conclusion, the total value used in the present work is in accordance with these works presented in table 3.5:

Work	***Geometry***	**Total Nodes**
[91]	NLR7301 and Flap	$182.295 \cdot 10^3$
[91]	GA(W)-1 Airfoil and Flap	$106.0 \cdot 10^3$
[97]	NLR7301 and Flap	$400.0 \cdot 10^3$
[92]	Three-element McDonnell-Douglas 30P30N Airfoil	$700.0 \cdot 10^3$
Present	NLR7301 and Flap	$233.462 \cdot 10^3$

Table 3.5: Comparison of implemented mesh nodes from different works on the NLR7301 airfoil with flap.

3.3 NLR7301 Shape Design Optimisation

Following the same pattern of the previous section, the shape optimisation procedure, starting from the mesh generation until achieving the optimised geometry, is summarised in the following flow chart:

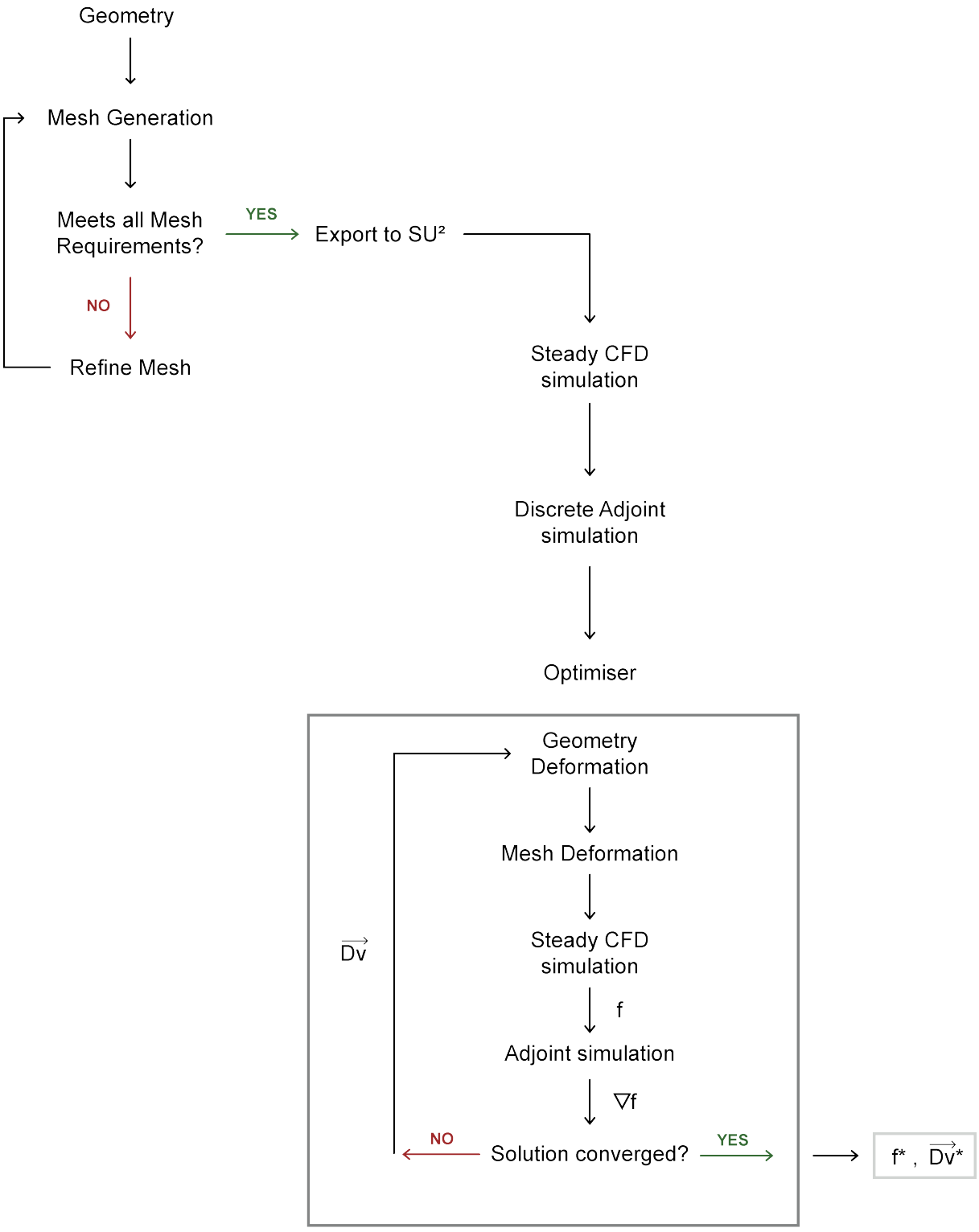

Figure 3.9: Procedure flow chart for the Shape Design Optimisation.

The optimisation part requires the mesh generation of its baseline geometry target: the **single element NLR7301** airfoil, which will be subjected to the same procedure and quality requirements as the high-lift configuration from the previous section. Following this step, a steady simulation will be utilised to perform a discrete adjoint simulation (widely introduced in section 3.3.1), both serving as starting solutions for the optimiser. Once inside the optimisation loop, both geometry and mesh are deformed accordingly to the selected objective function and constraints, which define the line of search of the whole process. At each optimisation iteration, steady CFD flow simulations are performed to analyse the flow behaviour around the new geometry, as well as discrete adjoint simulations in order to compute the gradients of the objective function (earning the classification of gradient-based shape design optimisation), leading to the next geometry design. This design-loop is exited when the convergence criteria is accomplished, eventually providing the optimised version.

3.3.1 Optimisation Problem Formulation

The aim of shape design optimisation is to improve the aerodynamic performances of an airfoil by means of modifications on its shape. Typical aerodynamic performances such as lift, drag, and lift-to-drag ratio, can be used either as a function to be mathematically minimised, as well as constraints to the problem, which define the direction the user wants the optimisation procedure to be headed to. In order to do so, the aerodynamic optimisation requires the definition of a set of design variables which, at each iteration, are manipulated to carry out the shape design procedure. As previously stated, a gradient-based optimisation technique is employed onto the present work, in which the shape optimisation is carried out by computing the gradients of the objective function with respect to the aforementioned design variables, named sensitivities, thereby directing the airfoil shape towards its optimised version.

The general formulation of a constrained optimisation problem is as follows:

$$\begin{aligned} &\text{minimise} && f(\vec{D_v}) \\ &\text{with respect to} && \vec{D_v} \\ &\text{subject to} && h_i(\vec{D_v}) = 0, \quad i \in \{1, ..., n_i\} \\ & && g_j(\vec{D_v}) \leq 0, \quad j \in \{1, ..., n_j\} \end{aligned} \tag{3.6}$$

The ingredients are the objective function, denoted by f, which must be derived with respect to the design variables vector, $\vec{D_v}$. Regarding the constraints, each of the equality-based constraint functions is denoted as h_i whereas the inequality-based ones as g_j. The conjunction between the design variables and the constraint functions will influence the optimiser's line of search, which means they must be accurately and carefully defined.

The methodology of the optimisation process in order to reach a new design for next iterations, is by computing the sensitivities by means of gradient computation. In charge of such task, Adjoint methods are considered, and are introduced in the next sub-section.

Sensitivity Computation

The line of search of the optimisation process is directed by the sensitivities, obtained from the objective function derivation with respect to the design variables defined by the user. SU^2 software has been implemented to solve the adjoint RANS equations and with two of the most popular methods for gradient computing: the continuous [130] and discrete adjoint methods [120]. Concerning the continuous methodology, the adjoint equations are obtained from deriving the governing PDE, to latter be discretised. On the other hand, the adjoint equations from the discrete methodology are directly obtained from deriving the already discretised governing equations. Their significant advantage among others is that the computational cost of deriving the derivatives is comparable to solving the governing PDEs of the flow [100].

Let us comprehend **how the adjoint approach works**:

The present work's problem is restricted to optimising objective functions defined on the solid wall (S) of the NLR7301 airfoil, say lift and/or drag coefficients. By means of a previous flow analysis, the surface flow properties regarding temperature (T), pressure (P), and viscous stresses ($\overline{\sigma}$), are used to parametrise the surface flow properties along the surface, with which the lift and drag coefficients can be obtained by its integration, and hence defining the objective function. The adjoint approach adds the flow equations as constraints to the objective function by means of a Lagrange multiplier [100] for each equation, thus obtaining a single function in which surface flow properties and the domain's flow equations are coupled.
By a an infinitesimal, arbitrary perturbation along the normal direction of the boundary S (δS, at each of the mesh surfaces nodes), a new deformed surface is obtained. Assuming a regular flow solution and a smooth boundary S, the variation of the objective function, regarding variations in the surface flow properties and flow equations due to the deformation, results on a new system of equations where deformations are accounted. The surface sensitivities are obtained by evaluating this resulting adjoint system. Within these sensitivities, there is stored the magnitude of the influence that a deformation applied on the very surface mesh nodes has got on the objective function. Recall, though, that the optimisation problem aims to perform the gradients/sensitivities of the objective function, with respect to a set of design variables ($\vec{D}_v$). Hence, a way of translating this surface sensitivities onto the design variables is needed.

Up to this point, here lies the appearance of a parametrisation method, which is particularly in charge of computing the previous surface sensitivities with respect to the design variables, and will be chosen and introduced in latter sections. We are just one step ahead from obtaining the desired objective function sensitivities with respect to the design variables: By means of a dot product operation involving the first, and second sensitivities, their computation is finally accomplished.

By way of a summary, the present work will consider the ***discrete adjoint method***, based on Auto-

matic Differentiation [131]. Once a flow solution is given by the SU2_CFD module, the SU2_AD module runs the adjoint with respect to the objective function so as to obtain the surface sensitivities, to latter be projected onto the design variables by the SU2_DOT module. When the gradients are computed, the optimisation algorithm makes the line of search apply the proper deformations through the SU2_DEF module onto the design variables to seek for the optimum solution.

3.3.2 Present Work's Computational Set-up

Once one of the main optimisation pillars is understood and processed, the focus of attention must be set on the implementation of the present work's optimisation. The starting point is presenting the mesh corresponding to the NLR7301 airfoil, followed by presenting an optimisation guideline on how to perform its shape deformation, and its objectives.

NLR7301: Mesh Implementation

The mesh regarding this case is significantly simpler to built, as the most challenging part has been meshing the gap from the flapped NLR7301 configuration. Even though there is just a single element, same quality requirements from section 3.2.2 must be accomplished.

The nodes placed on the airfoil's surface have been clustered towards both leading and trailing edges, eventually leading to a total number of surface nodes of:

Element	***Surface nodes***
NLR7301	351

Table 3.6: Nodes discretisation on the NLR7301 airfoil surface.

The boundary layer is created by quadrilateral elements algebraic extrusion in the surface normal direction, with a wall grid-spacing of $1 \cdot 10^{-6}$, implemented with a growth rate of 1.05. Once again, the Spalart-Allmaras condition is fulfilled ($y^+ < 1$) by this sufficient grid resolution:

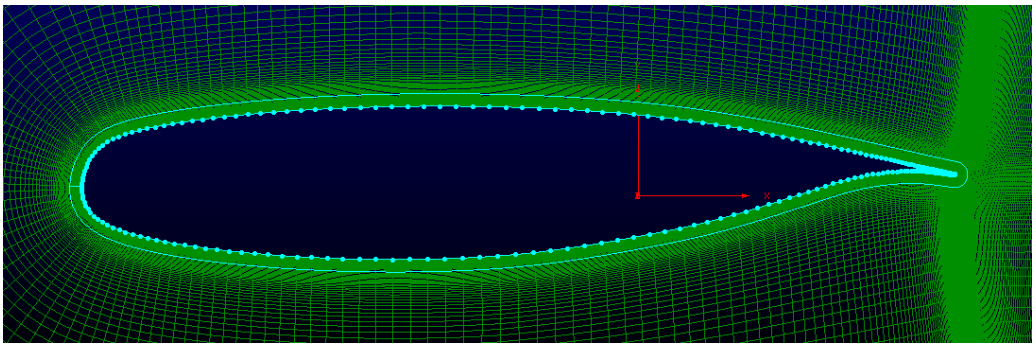

Figure 3.10: NLR7301 airfoil boundary layer mesh close-up.

The rounded trailing edge's boundary layer mesh is linked with a connector built *a posteriori*, following the same previous idea of refining the wake, in addition to allow for the second hyperbolic mesh

extrusion. Nevertheless, for this occasion, there is no clue towards which direction the wake will be directed to after some iterations of the optimisation process, in which the geometry will be modified, and so the wake. As a result, the wake's refinement connector is built on a straight line from the trailing edge, slightly accommodated through a curvilinear connector until reaching the downstream limits of the mesh's domain:

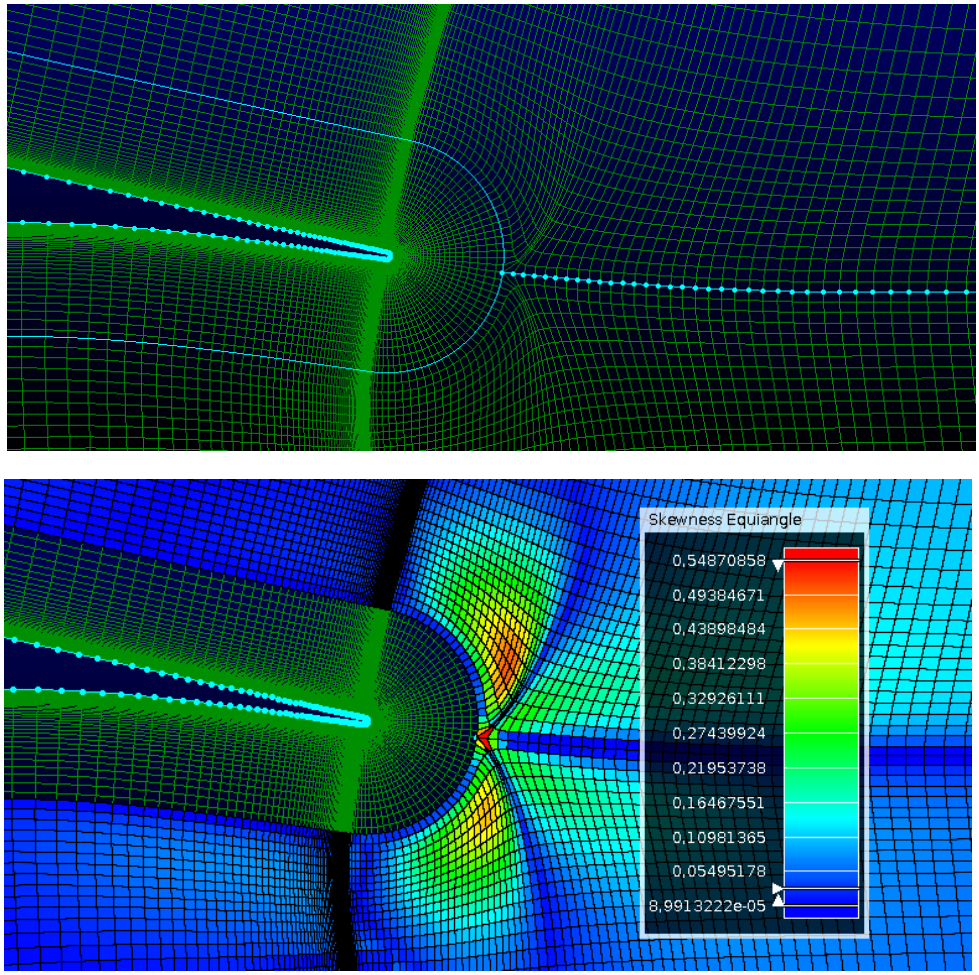

Figure 3.11: Boundary layer and trailing edge connector junction (upper), and its skewness mapping (lower).

With respect to this mesh junction on the trailing edge, the maximum skewness value is of ≈ 0.54, surrounded by cells with values around ≈ 0.3, following the same pattern as the flapped configuration (section 3.2.2). Parallel to it, the rest of the cells from the domain are within skewness values lower than ≈ 0.1, conclusively meaning that the mesh presents high quality in terms of skewness. This second mesh is built by hyperbolic extrusion using the outer limit of the boundary layer mesh, together with the trailing edge connector at a growth rate of 1.1 to ensure grid smoothness in the vertical direction.

This features altogether, compose the ultimate C-type mesh for the NLR7301 single element configuration, where the downstream boundary is located at 14 chord lengths after the airfoil's trailing edge, and 10 chord lengths towards the upper, lower and upstream directions; a very similar mesh to that of

the flapped configuration, as figure 3.12 illustrates:

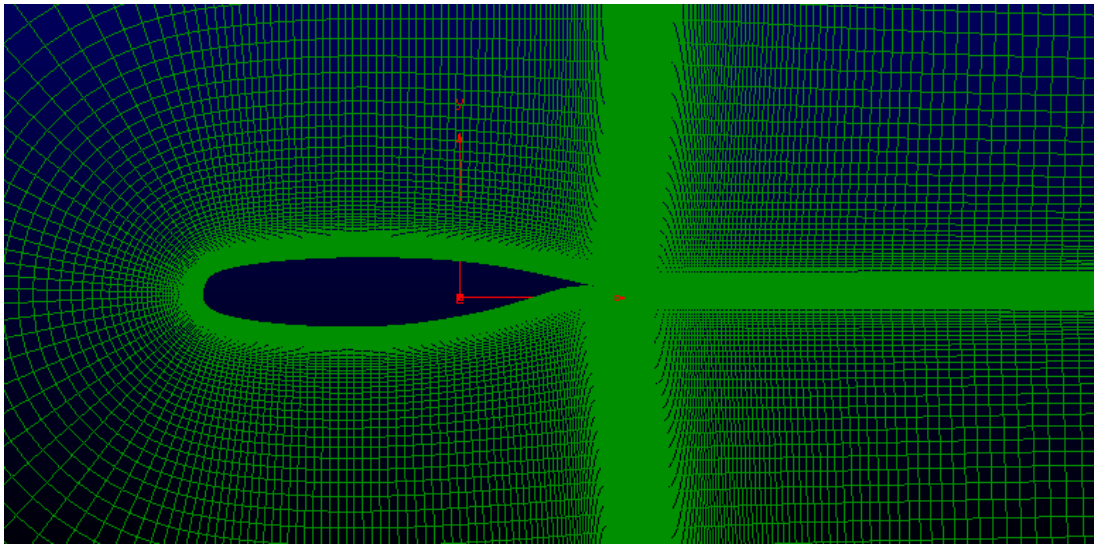

Figure 3.12: C-mesh topology for the baseline NLR7301 airfoil.

To officially bring the mesh generation section to an end, the total number of nodes that have been required to mesh all the domain is:

Geometry	**Total Nodes**
NLR7301 Airfoil	$84.650 \cdot 10^3$

Table 3.7: Implemented mesh nodes for the baseline airfoil NLR7301.

Flow Conditions

The flow properties around this geometry will be obtained by an SU^2 steady simulation at the same *Sea Level* conditions, with Mach and Reynolds numbers of $M = 0.185$ and $Re = 4.3 \cdot 10^6$, to that of the flapped configuration from section 3.2.1. The computational tools to compute the flow are the compressible RANS equations, accompanied by the Spalart-Allmaras one-equation turbulence model.

Once a proper solution is obtained, this will be used to run a discrete adjoint simulation in which the surface sensitivities will be computed. These two simulations serve as the starting solution for the optimisation cycle.

NLR7301 Optimisation Set-up

The shape optimisation analysis will be performed on the NLR7301 airfoil. It is very important to be aware of the main objective of this section: "**Gradient-based shape optimisation is undertaken in order to generate a morphing airfoil which reaches, or even surpasses, the performance requirements of the flapped configuration in terms of maximum lift, while avoiding significant penalisation onto the drag**".

However, this will not be allowed to be reached at any cost since realistic designs are chased, thereby suggesting the need to introduce several geometrical constraints to have control on the geometry deformations, so that from the nowadays (or short-term future) structural point of view, the optimised morphing airfoil can be as close as possible to a feasible design.

The methodology in charge of the shape geometry deformations will follow the aforementioned parametrisation methods, which have gained popularity in airfoil design optimisation. On the area of deformation methods, the primal airfoil geometry is altered so that a new shape is accomplished. The preferred technique for this section will be the **F**ree **F**orm **D**eformation (FFD) parametrisation method [132], which is very intuitive to use and can provide the deflection behaviour that is chased. In a general manner, FFD defines a parametric space by means of different control points so to envelop the airfoil geometry within it (the so-called *FFD box*). These control points will be taken as design variables ($\vec{D_v}$) and will impose the deformations onto the geometry at each optimisation step. With respect to other parametrisation methods implemented within SU^2 (such as Hicks-Henne's "bump" method [133]), one major advantage is its versatility in deforming any kind of complex geometries, which is due to a complete independence of its formulation from the geometry's mesh topology. Moreover, it allows to freeze multiple control points where no deformations are wanted or needed (*i.e.* local deformation), enlarging the availability for structural constraints. A recommended reading is the Master Thesis from Jõao Lourenço [134], in which a wide comparative study of different parametrisation methods is performed, on an optimisation study regarding the *RAE 2822* airfoil in transonic viscous flow.

In order to face the structural limitations that ought to be imposed in the subsequent designs, one must consider the wing structural layout of commercial jets along their wingspan, essentially composed by a wing-box structure, ribs, and some secondary structures such as the mechanisms to actuate the control surfaces or high-lift devices, all enclosed by the wing skin. Nowadays, the wing-box represents the main structural element and has been, along time, carefully designed and out of significant design changes. Considering this matter's sensibility, we encounter the need of defining a virtual wing-box, that must remain unchanged along all optimisation designs towards the definitive one. This prevents us from exploring in the full extent the design space for unconstrained designs that might, eventually, reach similar lift coefficients, or even better lift-to-drag ratios. However, these designs might imply very difficult shapes hard to reach, as well as to return to its original supercritical shape for cruise conditions. Consequently, **structural feasibility has been set as a priority for the present work**.

It is at this point, where the potential from the Free Form Deformation parametrisation method arises. The concept is well understood if it is firstly illustrated:

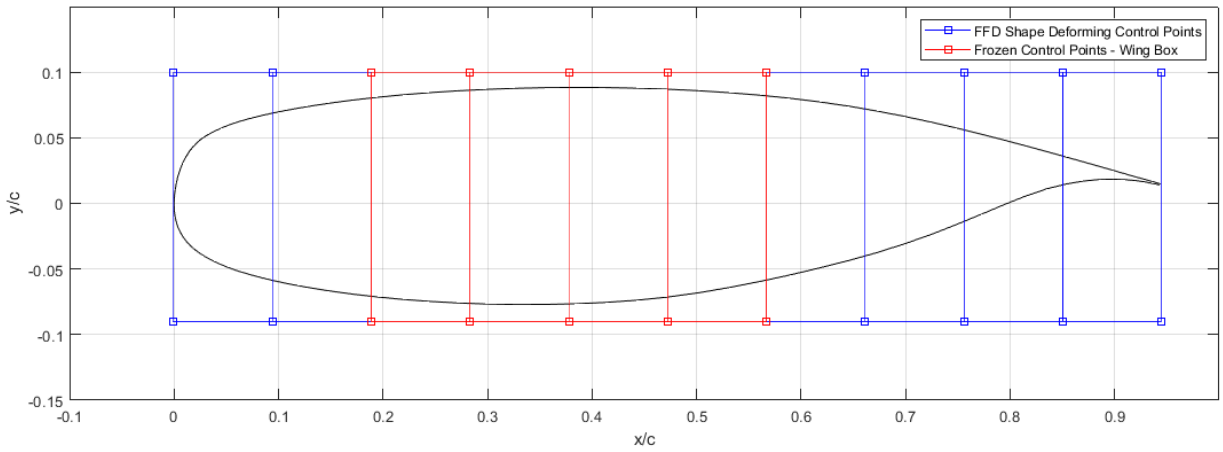

Figure 3.13: Design Variables located on the Free Form Deformation box.

The *FFD box* is defined within a set of 22 control points equally divided on the suction and pressure sides, as shown in figure 3.13, which are taken as the problem's design variables ($\vec{D_v}$). As a superficial advance of the results from section 5, it has been found that significantly increasing the number of design variables adds complexity to achieve the desired deformations, as well as adding more computational time to the simulations. On the contrary, small increases from 22 design variables showed to have non-profitable results compared to 22, which have proved to be supplying a total control of the shape deformations, as well as not being excessive time-consuming simulations.

The wing-box typically ranges from $\approx 0.2c$ to $\approx 0.6c$, a feature accomplished by freezing the control variables that are red-coloured in figure 3.13, leaving the rest (blue-coloured $\vec{D_v}$) in charge of the shape optimisation design. Nevertheless, the FFD formulation also focuses on the conjunction between fixed and non-fixed design variables, in which ensures a smooth continuity of the surface in the transition between one to another. Under the action of this methodology, design irregularities are avoided.

A last remark of how the *FFD box* is built, is that due to the possibility of selecting the location of the design variables within the SU^2 optimisation configure file, figure 3.13's distribution guarantees the enclosure of the NLR7301 airfoil with narrow margins between its geometry and the *FFD box* boundaries, so that the translation of the control points is in maximum coordination with the airfoil nodes.

It is defined by specifying the two-dimensional coordinates of the four box corners, starting at the leading edge on the suction side, towards the leading edge on the pressure side, on a clock-wise motion:

Tag, (I_{ind}, J_{ind})	**x/c**	**y/c**
$(0, 0)$	$-5 \cdot 10^{-4}$	-0.09
$(10, 0)$	0.945	-0.09
$(10, 1)$	0.945	0.1
$(0, 1)$	$-5 \cdot 10^{-4}$	0.1

Table 3.8: Coordinates from *FFD Box* limits.

to afterwards subdivide the box into the desired number of $\vec{D_v}$. The implementation of FFD design variables in SU^2 comes as follows:

$$DEFINITION\_DV = (15, 1.0 \quad | \quad AIRFOIL \quad | \quad AIRFOIL\_BOX, I_{ind}, J_{ind}, x_{mov}, y_{mov}) \tag{3.7}$$

where $AIRFOIL$ refers to the geometry of the NLR7301 defined in the boundary conditions, and $AIRFOIL\_BOX$ to the FFD box tag. With respect to I_{ind} and J_{ind}, they are the design variables identification tag. From left to right in figure 3.13, they range from $I_{ind} = 0$ to $I_{ind} = 10$, whereas $J_{ind} = 0$ for the pressure side, and $J_{ind} = 1$ for the suction side.

The key point lays on the vector (x_{mov}, y_{mov}), which are the *scale factors* of each of the design variables in both x and y directions. Their value acts directly upon the amplitude and direction of the surface deformation to be applied at each optimisation step: the higher the absolute value, the higher the achievable deformation. For a proper definition of each design variable, we need to know which is the desired behaviour of the deformations that are about to be applied on the non-fixed $\vec{D_v}$ of the airfoil, and the aerodynamic benefits that would supply.

In order to achieve a significant lift increase, two features from high-lift configurations must be pursued: ***chord*** and ***camber*** increase. In conventional high-lift configurations, this is achieved by the *slat* and the *flap*. Figure 3.14 illustrates a typical surface pressure distribution by a three-element high-lift configuration.

With respect to a **camber increase**: Due to the positive deflection of the slat and flap, the surface pressure difference between the suction and pressure sides of all elements also increases, and so the lift. From figure 3.14, it is very clear that there is a significant suction peak on the leading edge of the slat, double the amplitude of the main element's. This means there is a dramatic flow acceleration that lowers the pressure on the suction side of all elements. Moreover, it becomes an aerodynamic benefit, as the boundary layers of the two other elements are energised, thus contributing to a delay on stall effects. For the morphing airfoil, it must be reminded that possible stall effects may arise on its trailing edge, due

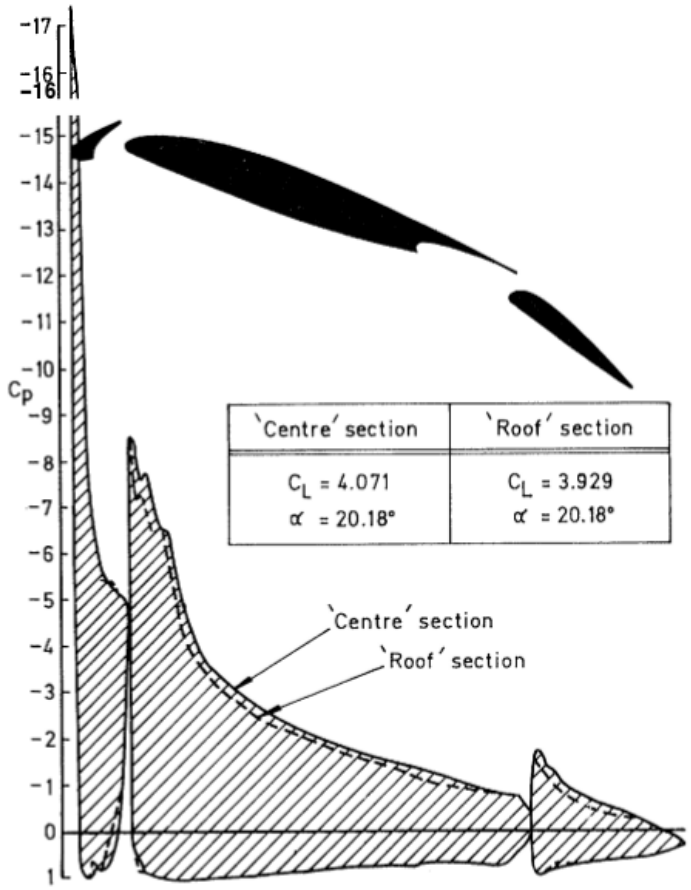

Figure 3.14: Typical surface pressure distribution for a three-element high-lift configuration [95].

to the lack of the flow acceleration provided by the main element-flap gap (section 3.2.1), which also energises the flap's boundary layer. With this in mind, the present work will explore the deformation of both leading and trailing edges of the morphing airfoil for camber increase, particularly focusing on the obvious aerodynamic benefits that a leading edge deflection supplies to delay stall effects.

With respect to **chord increase**: Deflecting the slat and the flap results in an inherent increment on the chord, and sectional area. As lift is directly proportional to chord:

$$l = \frac{1}{2}\rho_\infty U_\infty^2 c C_l \tag{3.8}$$

this feature will also be explored on both leading and trailing edges of the morphing arifoil. Moreover, it can also be helpful to develop a smooth deflection of its leading and trailing edges.

Lastly, it is of major importance to impose **geometrical constraints** to the shape optimisation design cycle, apart from the wing-box, which are adding structural feasibility to the ultimate morphing airfoil. Concerning the conventional high-lift configuration of the NLR7301 airfoil with trailing edge flap, the flap chord is of $c_f = 32\%c$, expressed with respect to the main element's chord. Consequently, the present

work will limit the chord growth on the NLR7301 baseline airfoil (c_B), to a maximum morphed chord value (c_M) of:

$$c_M \leq c_B + 0.32 \cdot c_B \tag{3.9}$$

Another important feature that is to be accomplished with the chord increase, is the subsequent sectional area increase. The main reason is regarding the minimum allowed airfoil thickness. If just surface stretching is imposed to achieve a chord increase, it is probable that large areas of the morphed airfoil are below the manufacturable thickness, specially on the trailing edge, where it is already of low values. As a result, this would imply that the morphing airfoil's surface can not withstand the aerodynamic loads, eventually breaking. Hence, a minimum thickness constraint is applied, in which a 5% of the airfoil's baseline maximum thickness (t_B) must not be surpassed in the morphed design (t_M):

$$t_M \geq 0.05 \cdot t_B \tag{3.10}$$

In addition, an area constraint is implemented to help support this concept, in which the morphed airfoil's area (A_M) is forced to grow at least a 50% of the area increase that the flap adds to the baseline airfoil in the conventional configuration ($\approx 30\%$):

$$A_M > A_B + 0.5 \cdot (0.3 \cdot A_B) = A_B + 0.15 \cdot A_B \tag{3.11}$$

Having achieved this structural analysis for a realistic design optimisation, what is left now is the definition of a proper objective function (say lift, drag, or lift-to-drag ratio), in order to achieve a morphed airfoil for which the lift is significantly increased, while respecting the aforementioned geometrical, structural impositions, to finally emulate the deflection of a slat and flap devices, just as illustrated in figure 3.15:

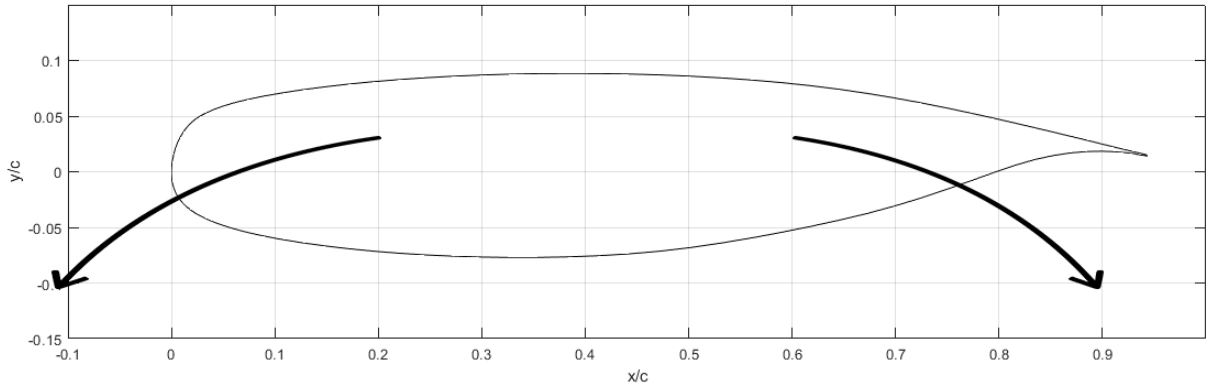

Figure 3.15: Desired deflection directions of leading and trailing edges of the morphing airfoil.

in conjunction with a proper definition of the scale factors (x_{mov}, y_{mov}) on each design variable out of the wing-box ($\emptyset$), to reach a smooth design:

Design Variable: (I_{ind}, J_{ind})	x_{mov}	y_{mov}
(0,0)	x_1	y_1
(0,1)	x_2	y_2
(1,0)	x_3	y_3
(1,1)	x_4	y_4
(2,0)	$\emptyset$	$\emptyset$
(2,1)	$\emptyset$	$\emptyset$
(3,0)	$\emptyset$	$\emptyset$
(3,1)	$\emptyset$	$\emptyset$
(4,0)	$\emptyset$	$\emptyset$
(4,1)	$\emptyset$	$\emptyset$
(5,0)	$\emptyset$	$\emptyset$
(5,1)	$\emptyset$	$\emptyset$
(6,0)	$\emptyset$	$\emptyset$
(6,1)	$\emptyset$	$\emptyset$
(7,0)	x_5	y_5
(7,1)	x_6	y_6
(8,0)	x_7	y_7
(8,1)	x_8	y_8
(9,0)	x_9	y_9
(9,1)	x_{10}	y_{10}
(10,0)	x_{11}	y_{11}
(10,1)	x_{12}	y_{12}

Table 3.9: Scale factors at each FFD design variables.

Chapter 5 will present the subsequent attempts regarding the definition of an objective function (f) and design variables ($\vec{D_v}$), that have let the way to the ultimate design.

3.4 Aeroacoustic Framework

The last of the three main modules concerning this work is the Aeroacoustic section, which follow the presented procedure:

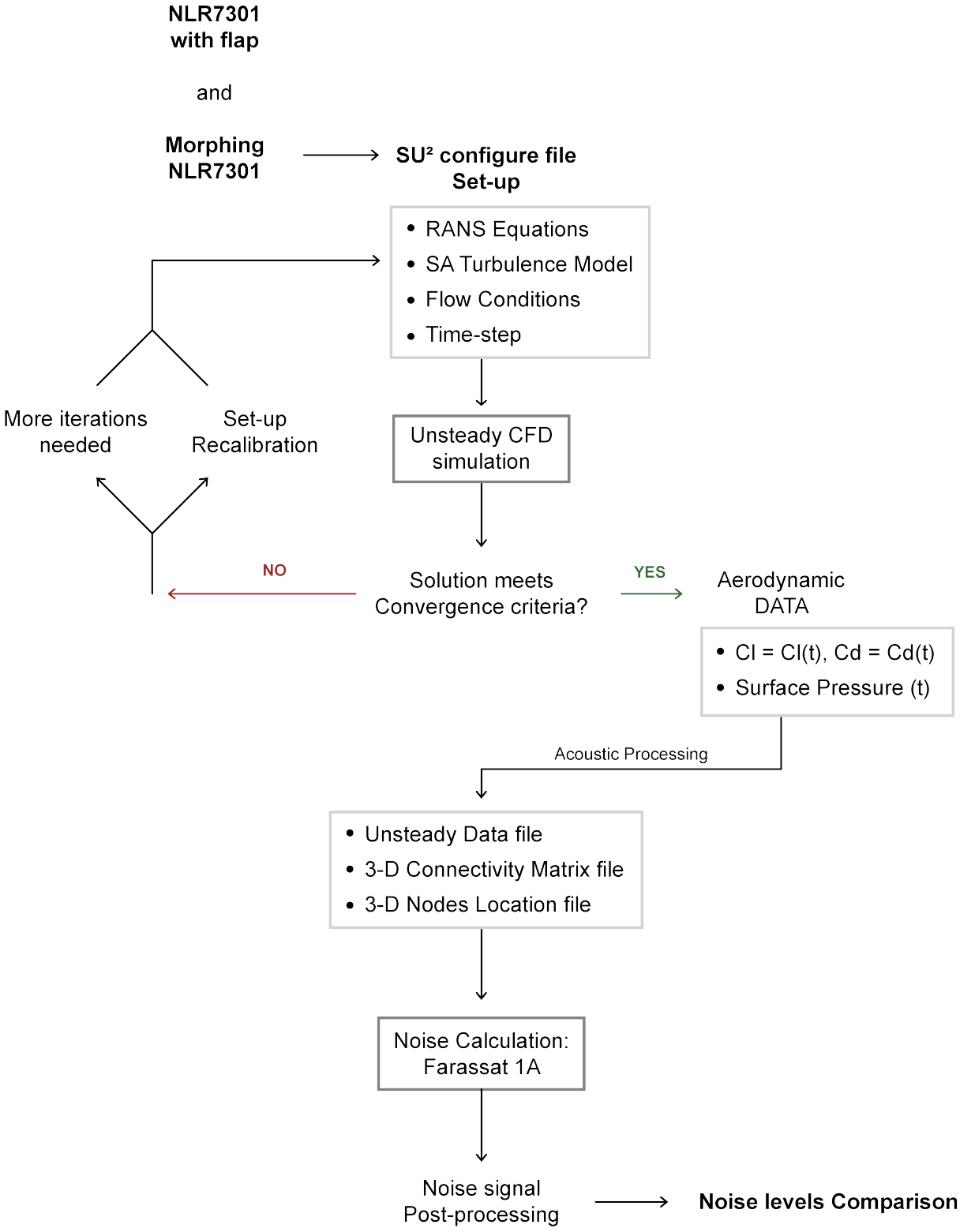

Figure 3.16: Procedure flow chart for the Aeroacoustic section.

Once the morphing airfoil is obtained, the acoustic framework will take the lead. Firstly, unsteady simulations will be performed for a certain time-span, obtaining the surface pressure distribution at each time-step, which will be properly manipulated to generate the format in which the input files of the aeroacoustic framework are formulated to read the data. Afterwards, by means of the Farassat 1A formulation, the acoustic signal will be calculated at a certain position, to latter be post-processed, conclusively determining the noise levels of the flapped and morphed NLR7301 airfoils for comparison.

3.4.1 Acoustic Framework Implementation and Verification

The verification of the Farassat 1A acoustic code provided by [114] was made against data supplied by *Delft University of Technology* on a NACA 0018 [119] at zero angle of attack. The wing geometrical characteristics and airflow conditions are summarised in tables 3.10 and 3.11, respectively:

chord, ***c***	$20\,cm$
span, ***b***	$8\,cm$

Table 3.10: Chord and span from NACA 0018.

Mach, ***M***	0.06
Reynolds, ***Re***	$2.8 \cdot 10^5$

Table 3.11: Mach and Reynolds numbers from NACA 0018.

This test-case was implemented only for bi-dimensional effects, providing the airfoil of a slight thickness. Unsteady surface pressure data was generated for a time-span of 0.2 seconds by means of solving the discrete Lattice-Boltzmann equations, at a sampling frequency of 30069 Hz. The unsteady surface pressure refers to local gage pressure in Pascal units, expressed as

$$p_{gage} = p - p_{\infty}, \tag{3.12}$$

which is the difference between the instantaneous pressure (at a certain time and node) and the undisturbed air pressure. The acoustic code calculates the thickness and loading noises by means of the Farassat 1A formulation (section 2.5.4) to obtain the total noise at a certain observer's location, defined by the user. Its original purpose was set to wind turbines acoustic applications, but it is adaptable to a bi-dimensional flow motion by neglecting the rotational speed.

Aeroacoustic Framework Input Data Structure

In order to be loyal to the validation procedure that was previously undertaken to validate the supplied acoustic code, the present work will reproduce the test-case's geometrical set-up from [119]. Hence, both configurations (flapped and morphed NLR7301) will be provided of the same thickness: $b = 8\,cm$.

The acoustic code needs the implementation of three files in order to be run, which are the unsteady data, the connectivity, and the nodes files.

$$\text{Aeroacoustic Framework } \textbf{Input files} = \begin{cases} \text{Unsteady Data} \\ \text{Wing Nodes Coordinates} \\ \text{Wing Connectivity Matrix} \end{cases} \tag{3.13}$$

First of all, the acoustic framework needs to be provided of geometrical information regarding the wing, which is built by extruding each airfoil section towards the z axis.

The procedure for creating the nodes is simply replicating the airfoil's section coordinates, defined in the two-dimensional domain (x, y), by adding a third coordinate (z). The definition of the nodes follows a strict order, starting at a reference node, which in the case of the flapped configuration, they are located at their corresponding trailing edges:

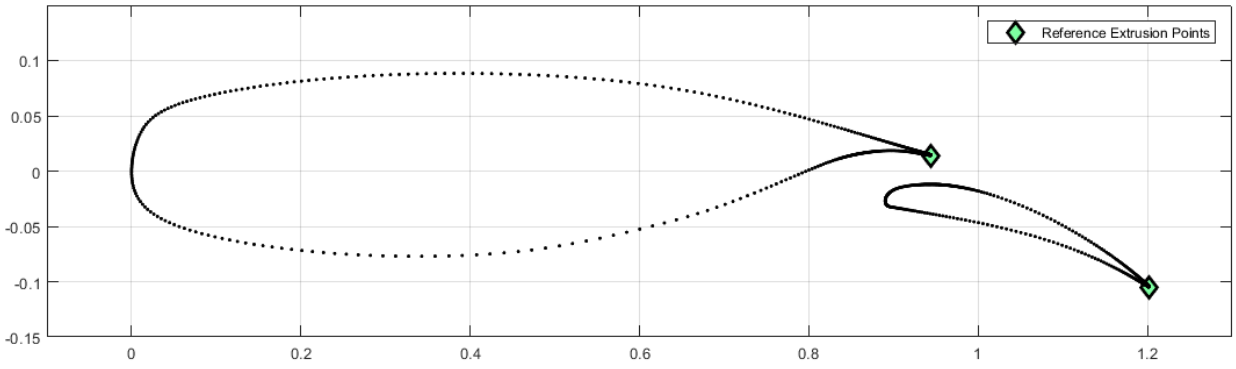

Figure 3.17: Starting indexing nodes for the NLR7301 airfoil and the flap.

Regarding the wing's discretisation (equivalent to a surface mesh), the maximum value of sections in which the acoustic code allows the wing to be discretised in z direction is 89. The nodes on each airfoil are indexed on a clockwise loop, starting from the reference nodes from figure 3.17 until reaching the previous adjacent one, and develop in the same order from negative half wingspan ($z = -b/2$) to positive half wingspan ($z = +b/2$), thus creating a symmetric wing with respect to the xy plane, indexing all the wing nodes in a spin-like motion along the wing airfoil sections which leads to indexing values ranging from $n_1 = 1$ up to $n_N = 1 + k \cdot 89$, where k is the number of nodes defining an airfoil section.

The format of the nodes file requires three columns for each direction, where the nodes are stored within each row:

$$Nodes = \begin{bmatrix} x|_{n_1} & y|_{n_1} & z|_{n_1} \\ x|_{n_2} & y|_{n_2} & z|_{n_2} \\ \vdots & \ddots & \vdots \\ x|_{n_N} & y|_{n_N} & z|_{n_N} \end{bmatrix}$$

Once indexed and identified, the connectivity matrix file is built by creating four-nodes-based panels,that link two adjacent wing sections with two consecutive nodes from one section, and their projections onto the adjacent one, following the same order as the nodes file, resulting in a surface mesh as illustrated in figure 3.18:

$$Connectivity = \begin{bmatrix} n_1 & n_2 & n_{2+k} & n_{1+k} \\ n_2 & n_3 & n_{3+k} & n_{2+k} \\ \vdots & & \ddots & \vdots \\ n_{1+k\cdot(89-2)+(k-1)} & n_{1+k\cdot(89-2)} & n_{1+k\cdot(89-2)+k} & n_{1+k\cdot(89-2)+2k-1} \end{bmatrix}$$

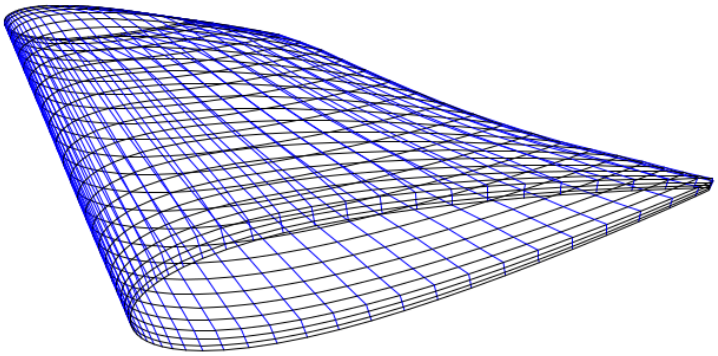

Figure 3.18: Four-nodes-based panel surface discretisation.

The present work will generate the unsteady data by setting up unsteady simulations on both original and optimised airfoils at this work's flow conditions ($Re = 4.3 \cdot 10^6$ and $M = 0.185$). So that a second-order accuracy is reached in the solution, a dual time-stepping simulation will be implemented (section 2.4.2). Spalart-Allmaras will again be the selected turbulence model (section 2.2). The starting flow solution at $t = 0s$ will be the previous Steady simulations, thereby causing a transient towards a stable flow fluctuation within the desired unsteadiness. Hence, the data sampling starts when reaching that point, for a time-span of $t = 0.2s$ and a certain sampling frequency f_s.

The required unsteady data for the subsequent acoustic calculations belongs to **surface pressure** unsteadiness, stored at each of the nodes previously defined, as the SU^2 software stores the flow properties at the nodes (section 2.4). Analogously to their extrusion, the surface pressure data will be replicated in the z direction along each of the wing's discretisation airfoils.
The required format for the unsteady file stores the data at each time-step (specified in the first column), at each row and for all wing's discretisation nodes as

$$Unsteady = \begin{bmatrix} t_1 & P_{n_1}|_{t_1} & P_{n_2}|_{t_1} & \dots & P_{n_N}|_{t_1} \\ t_2 & P_{n_1}|_{t_2} & P_{n_2}|_{t_2} & \dots & P_{n_N}|_{t_2} \\ \vdots & & \ddots & & \vdots \\ t_{end} & P_{n_1}|_{t_{end}} & P_{n_2}|_{t_{end}} & \dots & P_{n_N}|_{t_{end}} \end{bmatrix}$$

Output Acoustic Signal Computation and Observer's Location Display

The acoustic framework executes the Farassat 1A formulation to obtain the **Thickness** and **Loading** noises emitted as acoustic pressure signals from the very surfaces of the considered geometries. Regarding single element calculations such as the morphing airfoil, no assumptions must be done regarding the noise computation. However, some considerations must be exposed in this section concerning the flapped configuration.

The procedure for computing the total noise coming from separated sources, say the NLR7301 airfoil and the flap, is to sum their contributions to the same observer's location, which have been obtained from two different runs of the acoustic code. Consequently, influences on their pressure signals propagation due to the presence of neighbouring solid walls has not been accounted within the results. Even though this it thought to not significantly influence on the final results, it may lead to slight deviations on Sound Pressure Levels at some observer locations, compared to acoustic results in which this feature is implemented.The next step is locating a set of microphones-like display around the wing in order to calculate the corresponding Sound Pressure Levels, each of them specified within the acoustic input files. Previous acoustic mapping works [40] have placed the microphones at an azimuthal location with a radius of 1.6 meters around an airfoil at high-lift configuration. For the present work, as the airfoil will change its shape in the optimisation part, microphones will be placed at 2 meters radius to prevent possible excessive geometry close-ups, taking its origin at the mid-chord of the flapped NLR7301, spaced 10° from each other:

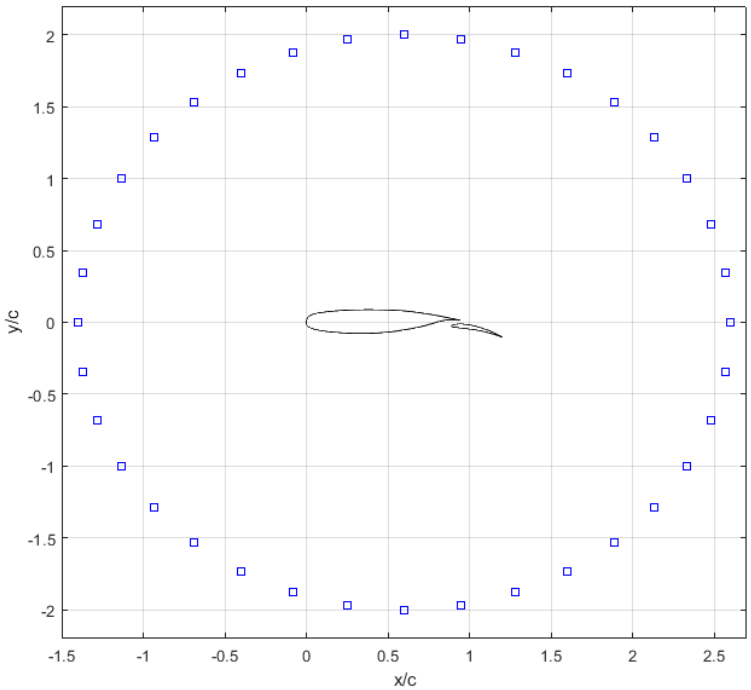

Figure 3.19: Microphone's deployment around the flapped NLR7301.

which will also be used for the morphing wing.

Once the Thickness and Loading noises are computed at each time-step and observer's location, computing the Total noise is simply a sum of these two contributions, all three quantities being written to an output text file in three columns.

Acoustic Signal Post-processing

The output acoustic signals in the time domain will be post-processed via applying the Fast Fourier Transform (FFT), which will provide its frequency spectrum, to latter display the one-third octave bands (2.5.6), where the dominant noise frequencies with their corresponding Sound Pressure Levels (SPL) will be easily readable. In addition to this, Overall Sound Pressure Levels (OASPL) will be plotted for each azimuthal location, providing of a spatial noise directivity mapping. These will be the tools that allow for comparison between the high-lift and morphed configurations' airframe noise emissions.

Chapter 4

Test-Cases Validation Results

This chapter presents a comparative analysis between the results obtained by the present and several works regarding the same test cases. The objective is to validate the Computational Fluid Dynamics and Aeroacoustics implementations.

4.1 Computational Fluid Dynamics (CFD): Aerodynamics

4.1.1 CFD Validation on the NLR7301 Airfoil with Trailing Edge Flap Test-case

The test-case that is used to validate all the computational CFD set-up implemented in the present work focuses on the wind tunnel tests developed at the National Aerospace Laboratory (NLR) on the flapped NLR7301 airfoil [96], at flow conditions of $Re = 2.51 \cdot 10^6$ and $M = 0.185$ (widely detailed in section 3.2.1).

In a way of summary, let us shortly remind the set-up of the present work for the subsequent **steady** CFD simulation:

Flow Equations	Compressible RANS
Turbulence Model	Spalart-Allmaras
Reynolds, **Re**	$4.3 \cdot 10^6$
Mach, **M**	0.185

Table 4.1: Summary of main CFD formulations used to describe the flow in the present work.

which will perform the flow description of the NLR7301 high-lift configuration at an angle of attack of $\alpha = 10.1°$ to latter compare the resulting surface pressure distribution and aerodynamic coefficients against the corresponding experimental results.

The convergence criteria of the present simulations corresponds to a density residual reduction of 5 orders of magnitude with respect to the initial value, which has been accomplished with $40 \cdot 10^3$ iterations for a Courant number of $CFL = 2$, guaranteeing the Spalart-Allmaras condition on its surface ($y^+ < 1$).

Following this set-up presentation, figure 4.1 displays a comparison between the surface pressure distributions from the present work against the experimental data obtained by *van den Berg* [96]:

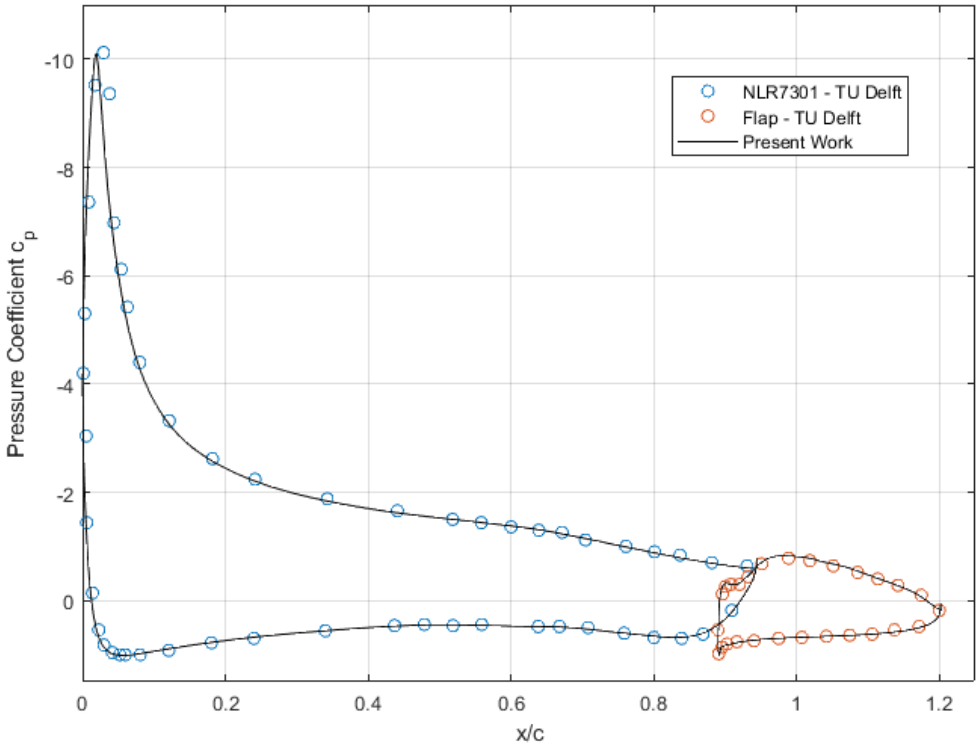

Figure 4.1: Surface pressure distribution along the flapped NLR7301 at an angle of attack of $\alpha = 10.1°$.

The obtained results show an excellent agreement with experimental values in terms of surface pressure distribution, corroborating the hypothesis on unnoticeable differences in the results due to using a different Reynolds number (section 3.2.1). It is important to emphasise on the adequate reproduction of the main element's leading edge pressure drop, which presents a peak at $C_p \approx -10$ due to the induced high flow acceleration. It is of vital importance to accurately capture this feature as the development of the flow in downwards direction will be strictly influenced by it, and consequently the surface pressure distribution that defines the aerodynamic coefficients, exhibited in table 4.2 together with the coefficient of moment:

	C_l	C_d	C_m
Experimental [96]	2.877	0.0567	0.463
Spalart-Allmaras [97]	2.766	0.0734	0.459
Spalart-Allmaras (Present work)	2.875	0.0597	0.481

Table 4.2: Comparison of numerical and experimental aerodynamic and moment coefficients for the flapped NLR7301 high-lift configuration.

achieving closer to experimental results than [97]. With respect to the present work's results, the relative

error from the experimental values concerning lift, drag, and moment coefficients are calculated and displayed in the following set of expressions:

$$\varepsilon|_{C_l} = \frac{|2.875 - 2.877|}{2.877} = 0.069\%,$$

$$\varepsilon|_{C_d} = \frac{|0.0597 - 0.0567|}{0.0567} = 5.29\%, \tag{4.1}$$

$$\varepsilon|_{C_m} = \frac{|0.481 - 0.463|}{0.463} = 3.88\%.$$

where the highest and lowest relative errors belong to the drag and lift coefficients, respectively, slightly overestimating the drag coefficient. This leads to conclude that the computational set-up with respect to flow equations, numerical discretisations, and boundary conditions, are well executed within the implemented mesh domain together with the Spalart-Allmaras turbulence model, proving their validity. Hence, this set-up will be subsequently used for further unsteady and optimisation simulations.

4.2 Aeroacoustics

4.2.1 Aeroacoustic Framework Verification on the NACA 0018 Test-case

The acoustic framework used within the present work [114] has previously been validated against a test-case involving a NACA 0018 airfoil at zero angle of attack (section 3.4.1). The unsteady surface pressure provided by [119] was processed by the Farassat 1A formulation to calculate the corresponding Loading and Thickness acoustic pressure signals (expressed in Pascal units in the time domain) at a selected observer's location during an analysis's time-span of 0.2 seconds, as illustrated in figures 4.2:

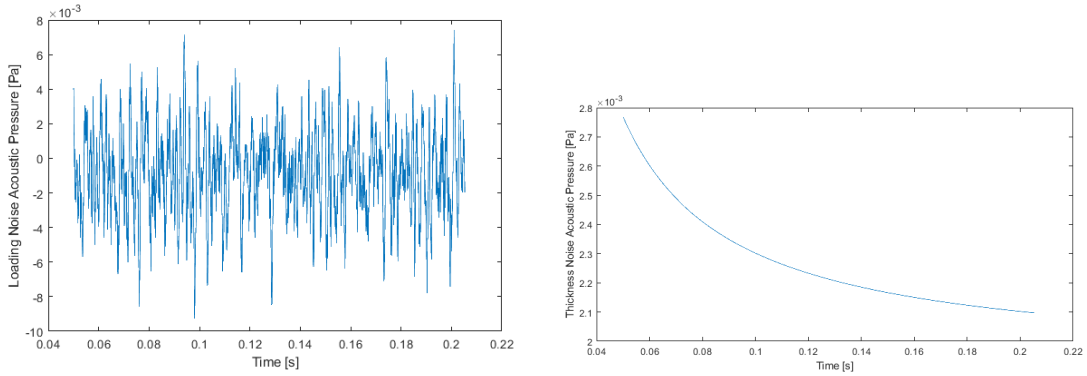

Figure 4.2: Loading (left) and Thickness (right) noise acoustic pressure signals from TU Delft experimental unsteady data.

It is interesting to point out the similar order of magnitude from both signals($\approx 10^{-3}$), although the loading noise is slightly higher in amplitude than the thickness noise. This balance between them are due to the low Mach number of the incoming flow ($M = 0.06$), which lowers the aerodynamic effects onto

the fluid, together with the zero angle of attack. In terms of noise, this means that the displacement that the wing exerts onto the fluid (monopole term) has a similar contribution at certain frequencies to that of the aerodynamic noise (dipole term) caused by the acceleration that the wing induces onto the fluid. On the contrary, as the present work is considering significantly higher free-stream conditions in terms of Reynolds and Mach numbers ($Re = 4.31 \cdot 10^6$ and $M = 0.185$), as well as a dramatic increase in angle of attack of $10.1°$, a considerable positive increment in order of magnitude regarding the loading noise is expected, as the aerodynamic acceleration effect onto the fluid is obviously of greater magnitude.

Once Farassat 1A has provided the acoustic signals, the present work has developed its own Fast Fourier Transform (FFT) and One-third Octave Bands codes by means of Matlab software for their post-processing, thus having the need of verification. For that purpose, the subsequent sound pressure levels for the Total noise are compared to those obtained by *TU Delft* [119] and the acoustic framework developed at IST [114], exhibited on one-third octave bands in figure 4.3:

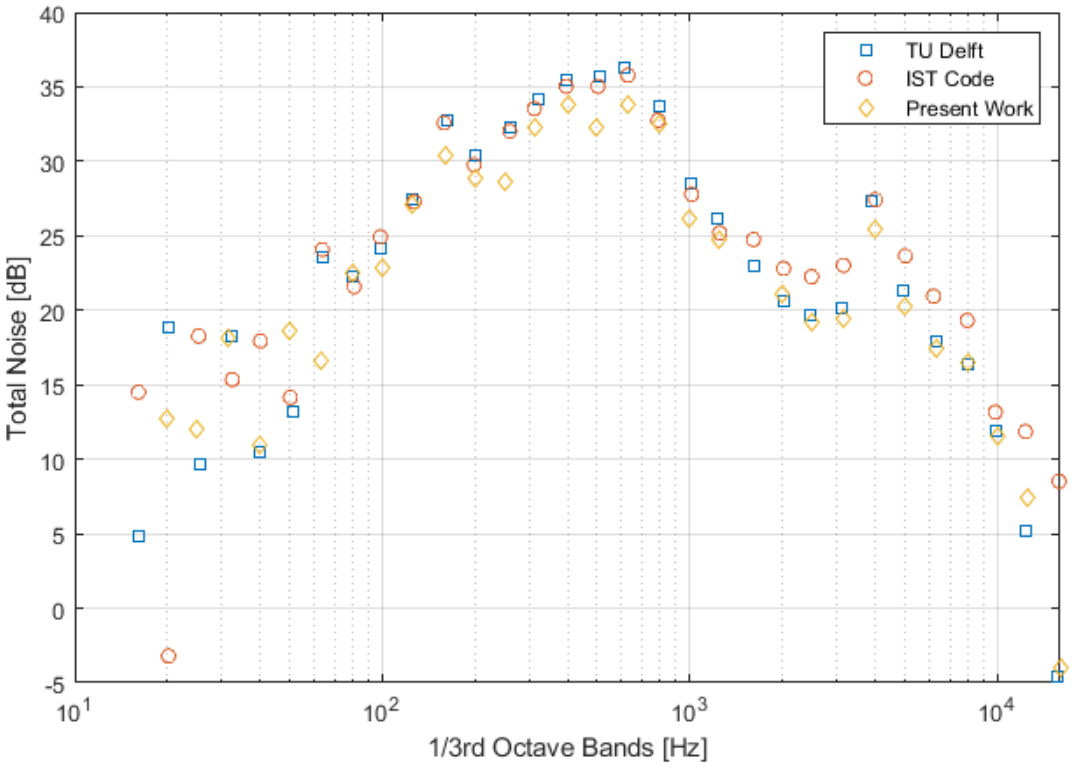

Figure 4.3: Total Noise sound pressure levels obtained by different works.

In a general basis, the sound pressure levels follow the experimental trend with fair agreement, specially after $f = 10^3 Hz$, conclusively proving the validity of the acoustic framework and its output results' post-processing implementations.

Chapter 5

Optimisation and Aeroacoustics Results

This chapter is entirely focused on the shape design optimisation results of the baseline NLR7301 airfoil, followed by the noise calculations of the high-lift configuration composed by the NLR7301 airfoil with a trailing edge flap, and the optimised morphing airfoil.

5.1 NLR7301 Steady Simulation Results

The previous step to the shape design optimisation of the NLR7301 airfoil is to know its aerodynamic capabilities within the aforementioned flow conditions of the present work: $Re = 4.3 \cdot 10^6$ and $M = 0.185$, at an angle of attack of $\alpha = 10.1°$. In order to do so, a steady simulation has been set, with the already validated computational set-up from previous sections: the flow is described by the compressible RANS equations, accompanied by the Spalart-Allmaras turbulence model within the mesh domain defined in section 3.3.2. Again, the convergence criteria corresponds to a density residual reduction of 5 orders of magnitude, having achieved such feature within $15 \cdot 10^3$ iterations, significantly lower than the flapped configuration from section 4.1.1, for a Courant number of $CFL = 2$. Together with the residuals evolution at each iteration, figure 5.1 also exhibits the surface pressure distribution along the airfoil, on which the Spalart-Allmaras condition ($y^+ < 1$) is guaranteed.

The obtained aerodynamic capabilities in terms of lift and drag coefficients are presented in the following table:

Lift coefficient, C_l	1.149
Drag coefficient, C_d	0.0216

Table 5.1: Lift and drag coefficients from the baseline NLR7301 airfoil.

At this point, it is necessary to recapitulate the results from section 4.1.1, in which the obtained lift coefficient belonging to the flapped configuration is $C_l = 2.875$. Considering the lift coefficient from the

single NLR7301 airfoil, it is now possible to specify that the main objective of the shape optimisation design is achieving or surpassing a positive lift increment of

$$\Delta C_l(\%) = \frac{C_l|_{opt} - C_l|_B}{C_l|_B} \cdot 100 = \frac{2.875 - 1.149}{1.149} \cdot 100 = 150.2\% \tag{5.1}$$

which is a major lift increase. Consequently, the optimisation set-up must be chosen wisely if such difficult challenge is to be accomplished, while respecting the structural limitations imposed onto the design.

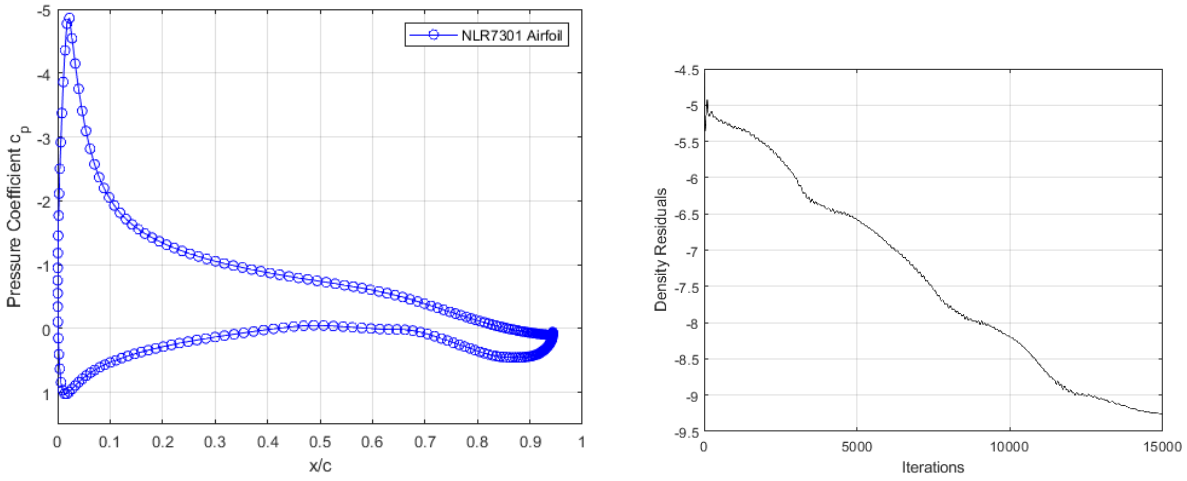

Figure 5.1: Surface pressure distribution (left) and density residuals (right) for the steady simulation of the NLR7301 airfoil.

5.2 Shape Design Optimisation of the NLR7301 Airfoil

This section comes with a big challenge: increasing the lift coefficient of the baseline NLR7301 airfoil by 150%. In order to do so, different combination sets regarding objective function and scale factors from the design variables have been tested.

5.2.1 Sensibility Analysis Overview on the Optimisation Set-up

Significant number of tests have been carried out to obtain sufficient sensibility for a good definition of the objective function (f) and the design variables ($\vec{D_v}$). For that reason, just conclusive discussions from this experience are presented within the following section. For further understanding of their background, the reader may be addressed to Appendix A, where two of the most determining tests and the resulting extracted conclusions are exhibited.

- **Objective function**, f: The ultimate optimisation set-up that leads the way to the desired morphing airfoil must be implemented with the lift as the objective function to force an abrupt increase of its value. Otherwise, setting the drag or lift-to-drag as the objective functions lead the line of

search into a loop with no exit, where no changes are applied to the baseline geometry due to the impossibility of severally increasing the lift while avoiding a drag penalisation.

- **Design variables set-up**, $\vec{D_v}$: The deflection direction is forced to emulate a slat and a flap for the leading and trailing edges' $\vec{D_v}$ by the sign of their scale factors. With respect to the leading edge, the movement directions are $(x_i < 0, y_i < 0)$, whereas for the trailing edge $(x_i > 0, y_i < 0)$. In order to ensure a smooth camber and chord increase on the trailing edge, a gradual decrease of the scale factors' amplitude from inner (closer to the wing-box) to outer $\vec{D_v}$ is implemented. If not, the line of search excessively deflects the trailing edge, overusing the outer $\vec{D_v}$ and avoiding a chord increase.

- **Aerodynamic constraints**: Setting up a maximum limit drag constraint within the optimisation set-up leads to structurally unreachable geometries, which also violate the geometrical constraints. For that reason, the minimisation on the drag penalisation will be faced by increasing the scale factors on the leading edge, or in other words, supplying more movement freedom in order to search for a deflection that leads to high flow acceleration, consequently delaying stall effects in such case.

5.2.2 Definitive Morphing NLR7301 Airfoil

With all the obtained sensibility, the ultimate design's optimisation set-up is mathematically formulated as:

$$\begin{aligned} &\text{maximise} && C_l \\ &\text{with respect to} && \vec{D_v} \\ &\text{subject to} && c_M \leq c_B + 0.32 \cdot c_B = 1.32 \\ & && t_M \geq 0.05 \cdot t_B = 0.00825 \\ & && A_M \geq A_B + 0.15 \cdot A_B = 0.1245 \end{aligned} \tag{5.2}$$

with an optimum set of scale factors for the non-fixed design variables ($\vec{D_v}$) (*i.e.* out of the wing-box ($\emptyset$) defined in the *FFD box*) as shown in table 5.2:

Design Variable: (I_{ind}, J_{ind})	x_{mov}	y_{mov}
(0,0)	-1.0	-1.0
(0,1)	-1.0	-1.0
(1,0)	-1.0	-1.0
(1,1)	-1.0	-1.0
(7,0)	0.6	-0.75
(7,1)	0.6	-0.75
(8,0)	0.5	-0.75
(8,1)	0.5	-0.75
(9,0)	0.4	-0.6
(9,1)	0.4	-0.6
(10,0)	0.225	-0.375
(10,1)	0.225	-0.375

Table 5.2: Definitive scale factors at each FFD design variables for the NLR7301 optimisation.

The specified constraints are of geometrical nature (widely introduced in section 3.3), expressed with respect to the NLR7301 baseline airfoil (denoted by the subscript B), ruling the ultimate morphing chord, minimum thickness, and area (c_M, t_M, A_M). The flow conditions remain fixed ($Re = 4.3 \cdot 10^6$ and $M = 0.185$) as well as the computational set-up, mainly composed by the compressible RANS equations and the Spalart-Allmaras turbulence model. The previous steady solution of the baseline airfoil (section 5.1) will be utilised to execute the sensitivities of the objective function (C_l) with respect to the design variables defined in table 5.2 by means of the discrete adjoint method. Following this step, the computed flow properties and sensitivities will serve as the starting point for the shape optimisation design cycle. Using a Courant number of $CFL = 2$, the convergence criteria will follow the previous statements, considering the solution as converged after achieving a density residual decrease of 5 orders of magnitude for both flow and adjoint simulations, at each optimisation iteration. Moreover, a maximum number of iterations is set to $20 \cdot 10^3$, in case unsteady features such as stall arise, which are out of reach for the steady simulations done by the optimiser, compromising the residuals. The definitive morphing NLR7301 airfoil is illustrated in figure 5.2, accompanied by its previous optimisation designs:

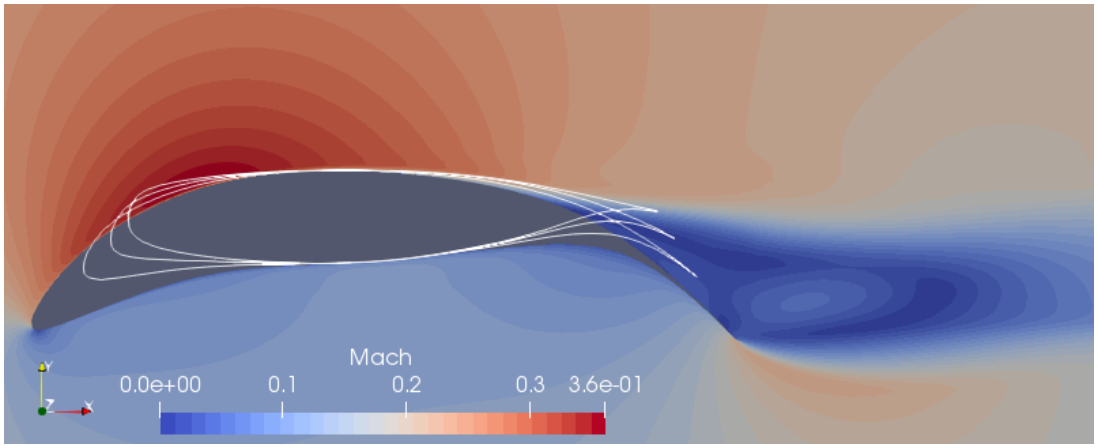

Figure 5.2: Definitive geometry of the morphing NLR7301 airfoil; Visualised with Paraview.

defined by the dimensionless geometrical characteristics exposed in table 5.3:

Chord, c_M	1.2528
Area, A_M	0.1342

Table 5.3: Dimensionless chord and area from the morphing airfoil.

which have both increased as well as respected the optimisation geometrical constraints. From a general point of view, smooth deflections have been achieved towards the desired directions thanks to the scale factors' sign convention and amplitudes, fairly emulating the deflection of a slat and flap devices. It is visible that given a higher scale factor to the design variables from the leading edge, these have explored towards a higher increase of camber through an addition of chord and sectional area. This is a clear sign of the strategy of cambering the leading edge for higher flow accelerations on the suction side to delay stall conditions, on which it has been reached a Mach number peak of $M = 0.36$. Moreover, there is a higher sectional area concentration within the leading edge, making it hard to reach problem-

atic thickness values below the manufacturable ones, allowing us to define less limiting scale factors than the trailing edge's ones. Concerning the trailing edge, camber increase by means of chord and area increases have also been achieved thanks to limiting the *FFD box* boundary design variables to power the inner ones, which have pushed the deflection in downstream direction. From the structural point of view, this part might be the most challenging due to the low thickness area on which the aerodynamic loads will be applied, although it does not surpass the established minimum thickness value of 5%.

The objective of this section is regarding the aerodynamic performance of this morphing airfoil. From figure 5.2, it is very noticeable that a separation bubble has formed on its trailing edge, an indicator of stall conditions which validates the hypothesis from section 3.3 concerning high probabilities of this feature's appearance, by neglecting the existing gap between the main element and the flap from the conventional high-lift configuration, for unchanged flow conditions. Consequently, both lift and drag coefficients are driven into an oscillatory motion due to significant unsteadiness induced by a locally stalled boundary layer, easily observed in figure 5.3:

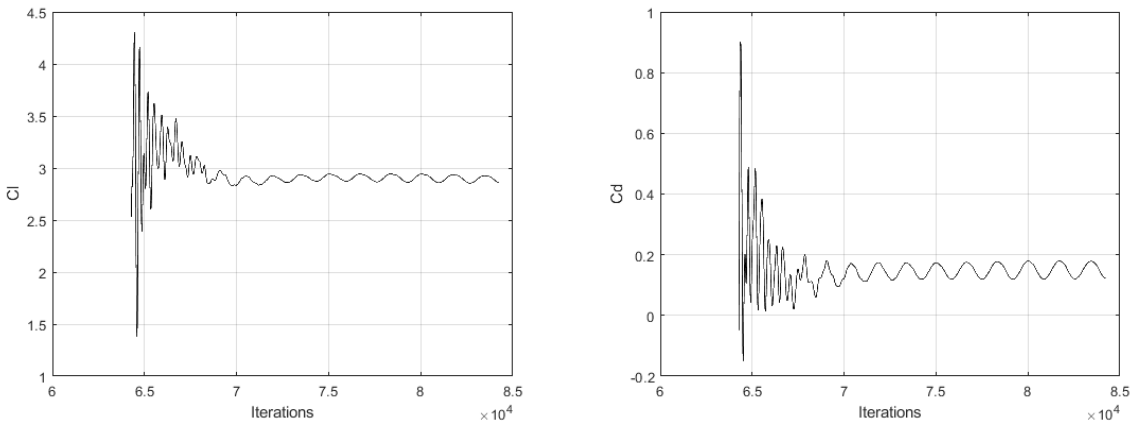

Figure 5.3: Lift (left) and drag (right) coefficients oscillations within the morphing airfoil steady simulation.

where the amplitude regarding the oscillations of the lift and drag coefficients are $\Delta C_l = 0.078$ and $\Delta C_d = 0.06$, where the mean values of these oscillations are placed at $\overline{C_l} \approx 2.85$ and $\overline{C_d} \approx 0.14$, respectively.

With respect to the lift increase, a comparable lift to that of the flapped NLR7301 configuration has been achieved, where the morphed airfoil's lift coefficient is just 0.09% below, thus not expected to compromise the noise calculations. On the other hand, the drag has been significantly penalised with a dramatic increase of 133% with respect to the flapped configuration. However, these values are relatively trusted, since the real characterisation of the aerodynamic coefficients will be properly set by the corresponding unsteady simulations, developed as a previous step for noise levels calculations in the following section, which will ensure a better capture of these unsteady features.

5.3 Aeroacoustic Noise Levels

The noise levels from the flapped NLR7301 and Morphing airfoils are obtained from surface pressure data provided by dual-time stepping unsteady simulations along a certain time-span, solving the compressible RANS equations together with the Spalart-Allmaras turbulence model. The starting flow solutions will be the ones provided from the steady simulations from section 4.1.1 for the flapped case, and from section 5.2.2 for the morphing airfoil, resulting into a transient state until the unsteady simulation evolves towards a stable solution. For that, unsteady simulations have been run for $t = 0.7s$ for both cases, reaching a stable unsteady state for which the surface data sampling has been carried out for a time-span of $t_s = 0.2$ seconds, at a sampling frequency of $f_s = 1000\,Hz$, or in other words, implementing a time-step of $\Delta t = 1ms$, resulting into a Strouhal number of:

$$St_l = \frac{f_s\, c}{U_\infty} = 15.87 \tag{5.3}$$

From a time-consuming point of view, this time-step was the minimum in order for the simulations to become feasible in time. Regarding the aerodynamic performances of the morphing airfoil after the unsteady simulations, its values slightly diverged from the corresponding ones within the previous steady simulation inside the optimisation cycle:

Lift coefficient, C_l	2.827
Drag coefficient C_d	0.155

Table 5.4: Morphing airfoil lift and drag coefficients from the unsteady simulation.

Consequently, the morphing airfoil represents a lift coefficient 1.73% lower than that of the flapped configuration, where the drag is significantly penalised by the presence of local stall conditions. However, the small difference in lift coefficient is not expected to have noticeable effects on the total noise computations. The acoustic framework processes the unsteady surface pressure data into an acoustic pressure signal by means of the Farassat 1A formulation which outputs two different typologies of noise contributions: the Thickness and Loading noises, which are summed to compute the Total noise. For an illustrative case, both Loading and Thickness acoustic pressure signals of the main element of the flapped configuration are displayed in figure 5.4 at an observer's location of $90°$:

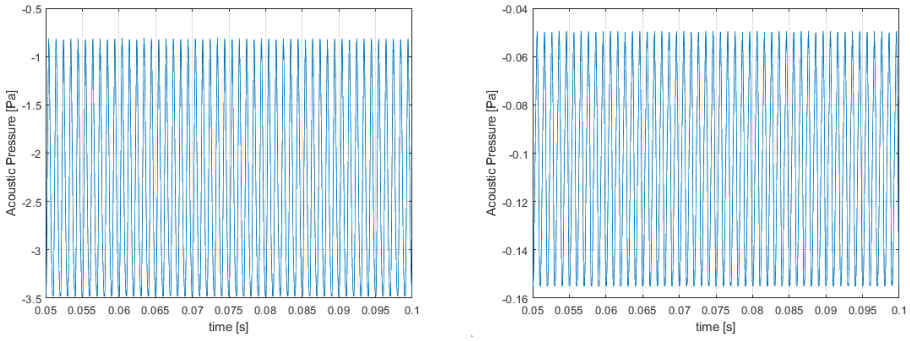

Figure 5.4: Loading noise (left) and Thickness noise (right) acoustic pressure signals.

providing one-third octave bands plots as

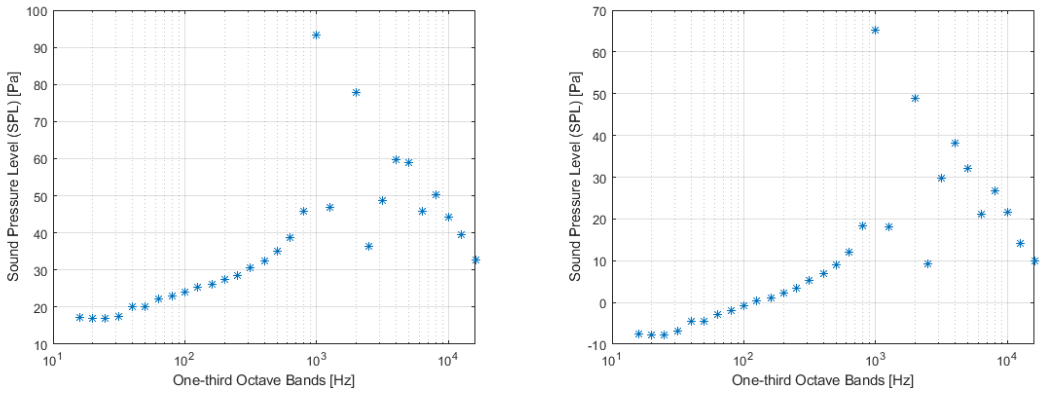

Figure 5.5: Loading (left) and Thickness (right) noise contributions on one-third octave bands at $90°$

clearly showing that the acoustic pressure signal is of greater amplitude than the Thickness noise's as stated in section 4.2, subsequently translated into higher SPL values from the Loading noise, as seen in the one-third octave bands. The following results are expressed in terms of total noise, beginning with an illustrative result of the Total noise acoustic pressure signals at an observer's location of $90°$ for the flapped configuration, showing the contribution of the main element and the flap, separately:

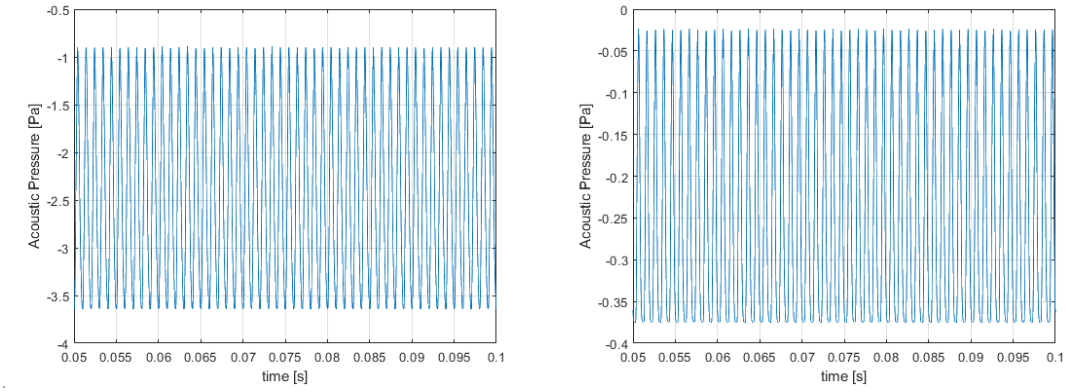

Figure 5.6: Acoustic Total pressure signals for the NLR7301 (left) and the trailing edge flap (right) at $90°$.

It can be seen that the amplitude of the Total noise acoustic pressure from the main element NLR7301 is one order of magnitude greater than the flap's one. In terms of noise, their corresponding one-third octave bands plots show that the Sound Pressure Levels from the main element (surpassing $90dB$) are also higher than the ones of the flap (slightly below $80dB$). It is reasonable to be so, as the highest acceleration induced on the fluid belongs to the leading edge of the main element, hence creating a way higher perturbation onto the fluid that is translated into major noise levels. Regarding the one-third octave bands plots, the general tendency matches with the experimental results obtained by [109] (left of figure 5.10) for an airfoil section including velocities close to the present work's, for a NACA 0012 airfoil section (with $c = 30.48cm$), in which the noise dominance belongs to two frequencies also set around $f_1 = 1000Hz$ and $f_2 = 2000Hz$ moving towards higher frequencies with an increase of the free-

stream velocity, shown in figure 5.7. According to what has been stated in section 2.5.4 from Curle's analysis [76], dipole sources have proved to be more efficient generators of sound within the subsonic regime, coming from the acceleration that surface induces to the fluid.

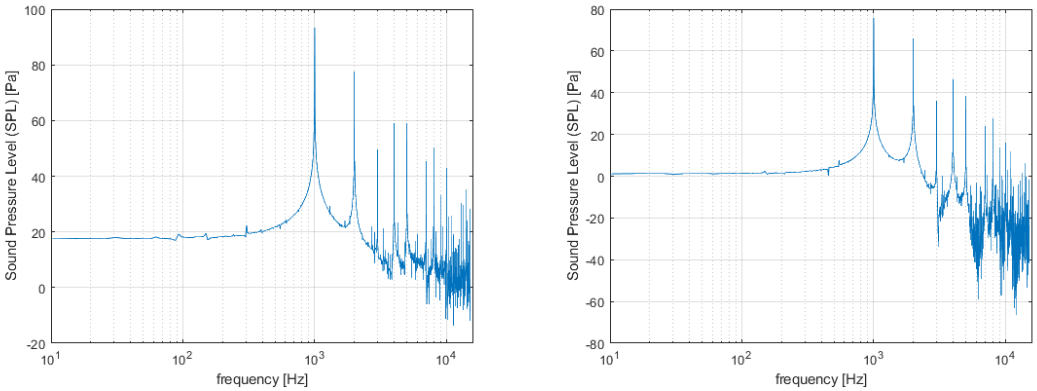

Figure 5.7: Frequency spectrum of the NLR7301 (left) and the trailing edge flap (right) at $90°$.

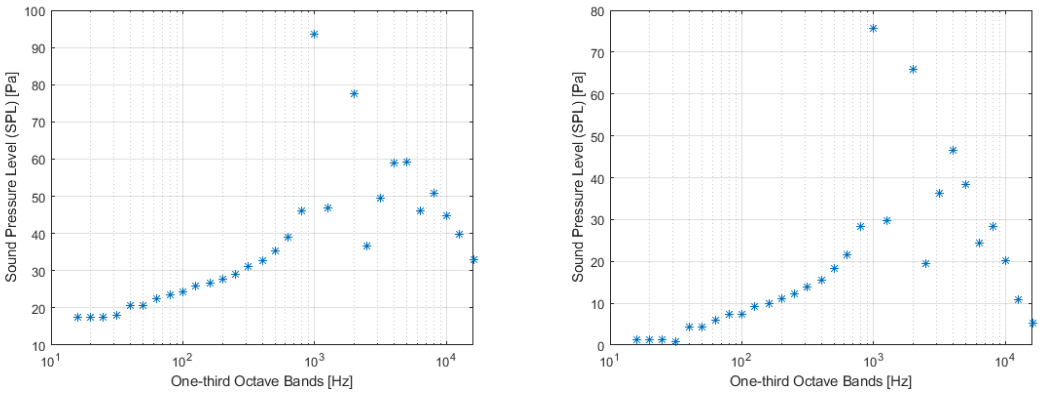

Figure 5.8: One-third octave bands for the NLR7301 (left) and the trailing edge flap (right) at $90°$.

Regarding the morphing airfoil, the FFT frequency spectrum and the one-third octave bands at the same observer's location are shown in figure 5.9. The dipole effect is not as clear as the flapped configuration, although dominant frequencies at positions $f_1 = 1000\,Hz$ and $f_1 = 2000\,Hz$ arise again, as seen in the one-third octave bands. Another characteristic feature arises at the low-frequency domain, in which in comparison with the spectrum from the two airfoils of the flapped configuration where this was not observed, an SPL peak at $f \approx 50\,Hz$ of $40\,dB$ appears. A study about flow features and self-noise of airfoils near stall or in stall [135] showed exactly the same phenomenon on experimental far-field data on a NACA 0012 at $\alpha = 10.8°$, in which deep stall effects such as vortex shedding were found to have influence on the low frequency range, presenting peaks in the frequency spectrum up to $50\,dB$, which are the signature of stall conditions (left of figure 5.10), also appearing in other experimental works such as [136]. Hence, this means that the present work also captures the unsteady fluctuations on the locally stalled trailing edge, at very similar SPL values within the aforementioned studies.

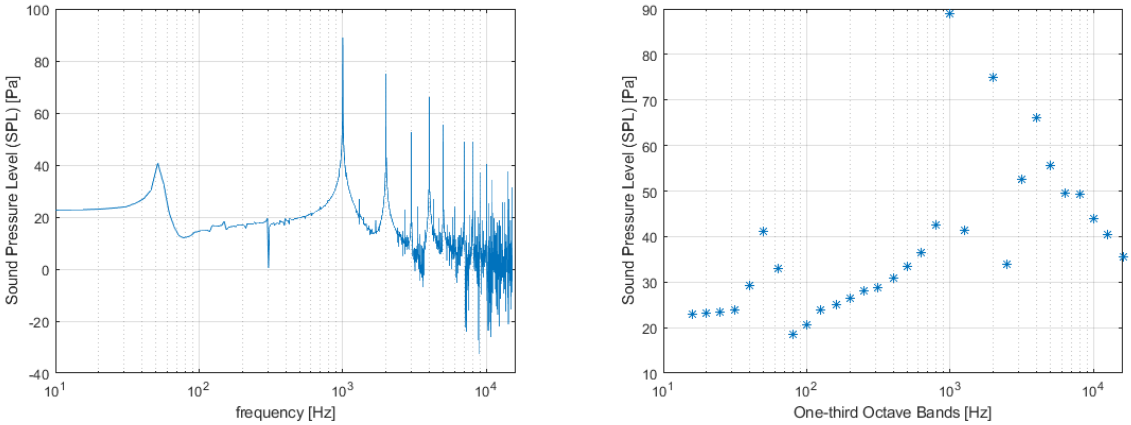

Figure 5.9: Frequency spectrum (left) and one-third octave bands (right) of the Morphing airfoil at $90°$.

In works such as [109], the noise regarding separation has also been quantified and exhibited on one-third octave bands for the a NACA 0012 (right of figure 5.10):

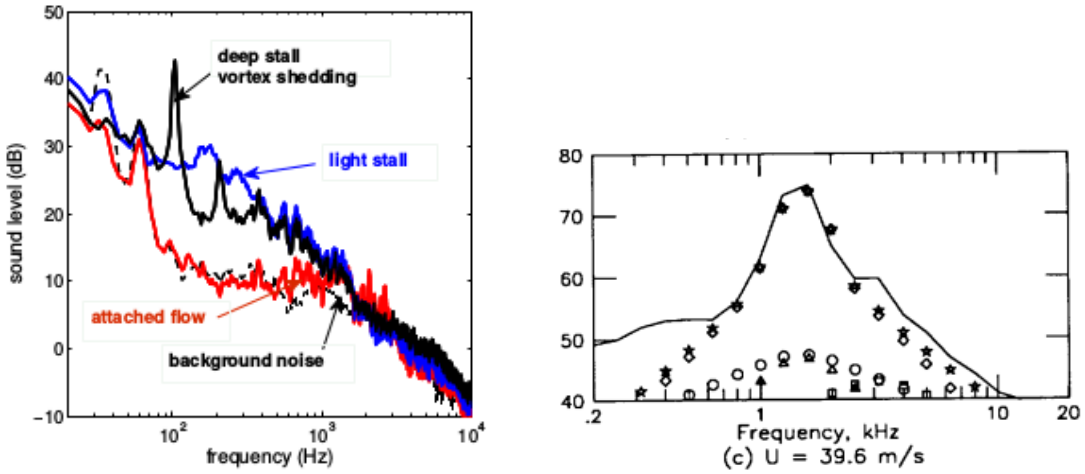

Figure 5.10: NACA 0012's frequency spectrum under deep stall [135] (left) and NACA 0012's one-third octave bands [109] (right).

It can be seen that, in the case of the right figure regarding stall noise (triangular markings), the noise peak is also set at around $50\,dB$. However, for this case, the SPL range is wider than the obtained in the present work, as a result of not capturing all stall features out of the airfoil's surface. Conclusively, it can be stated that at least a percentage of stall noise is captured within the final noise levels, as shown within the one-third octave bands from the morphed airfoil.

A very important matter must be addressed when computing the Overall Sound Pressure Levels (OASPL) at the different azimuthal locations around the Morphing airfoil. As the acoustic framework of the present work computes the total noise emitted only by the surface pressure fluctuations, the noise emitted by vortex shedding features from stall conditions are not accounted, and that must be taken into account in the OASPL values. Regarding the noise estimation of an airfoil at a deep stall condition along all its surface, works such as [111] have quantified an increase in sound pressure levels up to $10\,dB$. Never-

theless, for the present work's morphing airfoil, the situation is slightly different due to the fact that just a percentage of the whole airfoil is under stall conditions and such increments might not be achieved, as well as already capturing some stall noise contribution on the surface, as seen before. However, in order to provide a conservative approach to the matter, this hypothetical increase in the OASPL values will also be displayed in figure 5.11:

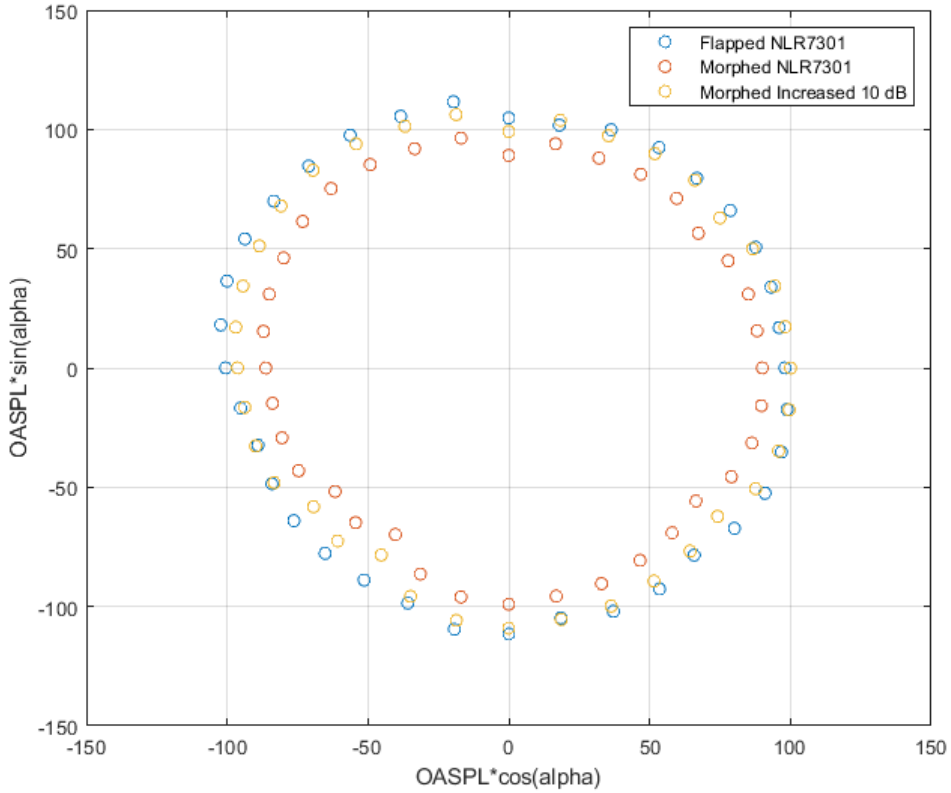

Figure 5.11: OASPL comparative results between the flapped and morphing NLR7301 airfoil.

Firstly, regarding the quality of the results, the smoothness of this OASPL spatial distribution directivity shows compactness [119], which means that the Strouhal number of the unsteady simulations is adequate for both the conventional and morphed configurations. Without accounting for the stall noise increase of $10\,dB$, figure 5.11 shows a clear OASPL reduction of the morphing airfoil with respect to the conventional high-lift configuration for all observer's locations. Even though it is not expected to change such conclusions, it must be stated that the fact that the resulting lift coefficient from the morphing airfoil is 1.73% lower than the conventional high-lift configuration, slight differences on the OASPL, and consequently on these conclusions, might be obtained. When accounting for the limit case of noise increase of $10\,dB$, the majority of the OASPL values are still below the values from the conventional configuration, although these significant increase due to the suction side being under deep stall conditions are not equivalent to the morphing airfoil case, in which this condition is localised upon its trailing edge.

The quantification of such increments is displayed in figure 5.12, composed by the morphing noise

relative increments in percentage not accounting (left) and accounting (right) for the $10 dB$ increment of stall noise. In these plots, positive values represent a relative noise decrease whereas negative values a relative increase:

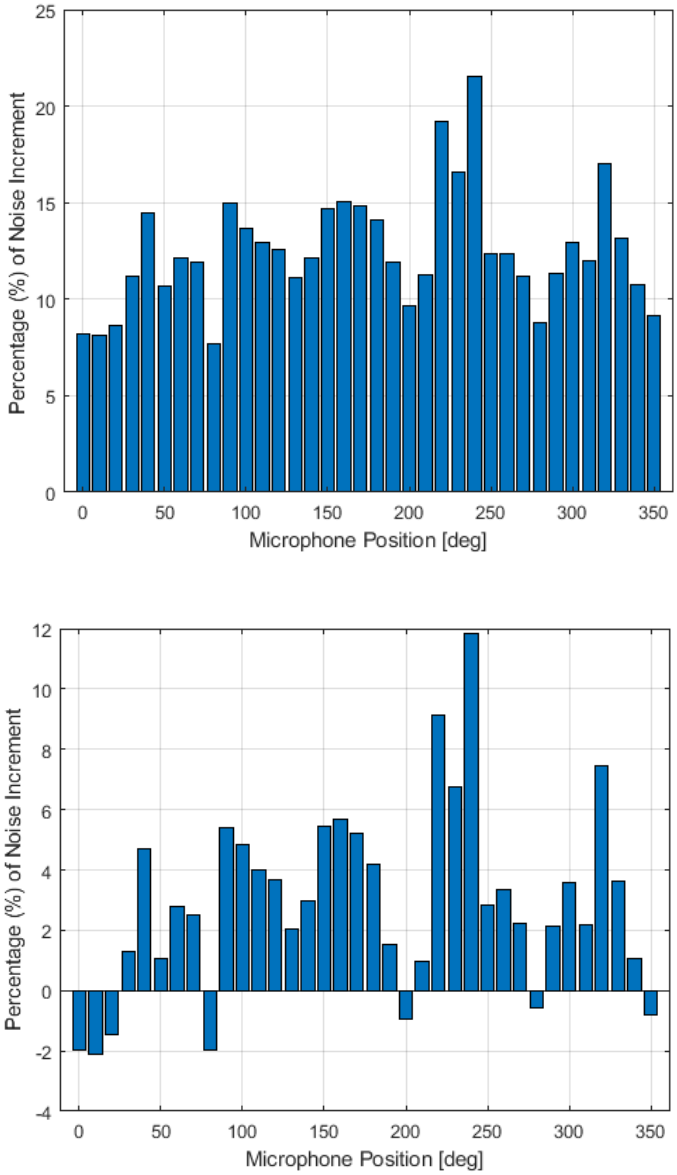

Figure 5.12: Percentage of airframe noise increment for the Morphing airfoil with respect to the Conventional configuration (upper), and with 10 dB of stall noise increment (lower).

Concerning the first case, all microphones suggest an overall noise reduction with the morphing airfoil, achieving a maximum decrease of 22% at position $240°$, and a minimum decrease of $7.5 dB$ at position $10°$. On the other hand, considering the extra stall noise, seven of the microphones suggest an increase of noise, although not surpassing a 2%, contrasted with the maximum decrease of 12%.
As an overall result, it can be concluded that the morphing airfoil provides a significant improvement in airframe noise performances with respect to the conventional configuration in both cases, even with a substantial noise increase of $10 dB$.

Chapter 6

Conclusions

The objectives of this thesis were to develop a methodology to perform a shape design optimisation of a two-dimensional airfoil section by means of the morphing concept, in order to achieve equivalent lifting capabilities to a high-lift configuration at take-off and landing performances, to latter obtain the airframe noise contributions regarding both configurations for comparison. The high-lift configuration represented by the baseline airfoil *NLR7301* with a trailing edge flap has been tested. Steady simulations have been carried out with the open-source software SU^2 at the same flow conditions as the experimental tests that have validated the computational set-up implemented within this work. Firstly, the domain has been meshed, where the compressible RANS equations accompanied by the Spalart-Allmaras turbulence model have been used for describing the flow, giving excellent results compared to experimental data. The optimisation has been undertaken onto the baseline airfoil *NLR7301*, which has been morphed by using a gradient-based methodology to compute the sensitivities of the objective function by means of the discrete adjoint method: the lift coefficient. Regarding the shape deformation, the Free Form Deformation parametrisation method has been in charge of such task. Finally, unsteady simulations have been performed in order to obtain the surface pressure distributions along a certain time-span for both configurations, which have been used as the input data for the acoustic framework provided by [114], in which Total noise contributions (composed by the Thickness and Loading noises) at a set of observer's locations have been computed for both configurations using the Farassat 1A formulation, to finally be compared. The morphing airfoil has proved to be advantageous in terms of noise emissions for a comparable lift as the flapped configuration, up to a 22% of reduction, although having a significant penalisation onto the drag coefficient due to stall conditions on its trailing edge. Concerning commercial airliners, take-off and landing performances represent a small percentage of the totality of a flight, which mostly belongs to cruise conditions. Hence, as the morphing airfoil can also be optimised during cruise conditions, the penalisation on drag on take-off and landing performances in terms of a higher fuel consumption could be balanced on cruise conditions.

6.1 Achievements

The present work has achieved two objectives regarding Aerodynamics and Aeroacoustics. Within the Aerodynamics section, it has been achieved to implement a computational high-accuracy CFD set-up to perform flow analysis on two-dimensional high-lift configurations as well as single element airfoils on steady and unsteady simulations. A methodology for shape design optimisation of an airfoil in order to emulate a conventional high-lift configuration under structural feasibility constraints has also been successfully accomplished. Lastly, the coupling of the aerodynamic data with an aeroacoustic framework that generates acoustic predictions by means of Loading and Thickness noises has also been accomplished.

6.2 Future Work

Within the aerodynamic section, the Spalart-Allmaras turbulence model has been used for all computations, even for locally separated regions regarding the morphing airfoil. As other turbulence models have shown better agreement to stall conditions, such as the Menter SST turbulence model, further comparisons between the results achieved within this work against other turbulence models should be performed. Moreover, Large-Eddy Simulations may also be implemented so that large scale flow features such as the separation bubble exhibited by the morphing airfoil can be represented and compared to the present work's one. Another feature that could be studied is the influence of the Strouhal number on the dominant frequencies (*i.e.* performing unsteady simulations using several time-steps) in order to see if other dominant frequencies are captured. Consequently, in case of a more accurate flow description, better aeroacoustic predictions can be performed. Severe research should be performed regarding flow control techniques in order to delay the stall separation on the trailing edge, and hence reducing the overall drag to improve its aerodynamic performances. In addition, experimental tests should be performed to quantify the whole contribution of stall noise to the far-field, enhancing the OASPL spatial mappings obtained within this work. Regarding the structural feasibility of the morphing airfoil, structural analysis could be performed in order to prove its manufacturability and capability of withstanding the aerodynamic loads, specially on its trailing edge. Several studies may be focused on research for proper skin materials, which can be easily deformable, and their corresponding mechanisms to perform such deformations. Furthermore, in order to achieve a more realistic level, three-dimensional wing designs using the morphing airfoil would bring highlights about three-dimensional effects, leading to closer-to-reality new conclusions.

Bibliography

[1] World Health Organization. Burden of disease from environmental noise. Quantification of healthy life years lost in Europe. Technical report, JRC European Comission, Copenhagen, Denmark, 2011.

[2] C. Clark. Aircraft Noise Effects on Health. Technical report, Centre of Psychiatry Barts and the London School of Medicine. Queen Mary University of London, May 2015.

[3] R. N. Lawton and D. Fujiwara. Living with aircraft noise: Airport proximity, aviation noise and subjective wellbeing in England. *Transportation Research Part D: Transport and Environment*, 42:104 – 118, 2016. ISSN 1361-9209. doi: https://doi.org/10.1016/j.trd.2015.11.002.

[4] L. Jarup. Hypertension and Exposure to Noise Near Airports: the HYENA Study. *Environmental Health Perspectives*, 116(3):329–333, March 2008. ISSN 0091-6765. doi: 10.1289/ehp.10775. URL http://www.ncbi.nlm.nih.gov/pmc/articles/PMC2265027/.

[5] European Aviation Safety Agency. EASA Certification noise levels. URL: "https://www.easa.europa.eu/easa-and-you/environment/easa-certification-noise-levels", 2018.

[6] Federal Aviation Administration (FAA). Title 14 Part 36 – Noise Standards: Aircraft Type and Airworthiness Certification. URL: "https://www.faa.gov/about/office_org/headquarters_offices/apl/noise_emissions/airport_aircraft_noise_issues/levels/", 2018.

[7] International Civil Aviation Organization (ICAO). *Annex 16 Environmental Protection Volume I*, 9^{th} edition, 2014.

[8] United Nations. Department of Economic and Social Affairs. *World Urbanization Prospects: The 2014 Revision*. Population Division, New York, 2015. (ST/ESA/SER.A/366).

[9] United Nations. Department of Economic and Social Affairs. World Population. URL: "https://esa.un.org/unpd/wpp/", 2017.

[10] EuroControl. Challenges of growth 2013. Task 4: European Air Traffic in 2035. Technical report, European Organisation for the Safety of Air Navigation, 2013.

[11] Airbus. Global Market Forecast. Growing Horizons 2017/2036. Technical report, Airbus S.A.S., Blagnac Cedex, France, 2017.

[12] Boeing. Current Market Outlook 2017/2036. Technical report, Boeing, Seattle. WA 98124-2207, 2017.

[13] European Comission. Horizon 2020. EU Research and Innovation programme. URL: "https://ec.europa.eu/programmes/horizon2020/".

[14] Clean Sky. Horizon 2020. EU Research and Innovation programme. URL: "http://www.cleansky.eu/".

[15] Rept. of the Group of personalities. European Aeronautics: A vision for 2020, Meeting Society's Needs and Winning Global Leadership. URL: "http://www.cleansky.eu/", January 2001. ISBN: 92-894-0559-7.

[16] Clean Sky. Clean Sky at a Glance. Technical report, Horizon 2020. EU Research and Innovation programme, Avenue de la Toison d'Or 56-60. Brussels, Belgium, 2016.

[17] Clean Sky. Special Edition. Noise Reduction. Technical report, Horizon 2020. EU Research and Innovation programme, Avenue de la Toison d'Or 56-60. Brussels, Belgium, 2014.

[18] Advisory Council for Aviation Research and Innovation in Europe (ACARE). Flightpath 2050. URL: "http://www.acare4europe.org/sria/flightpath-2050-goals/protecting-environment-and-energy-supply-0".

[19] Federal Aviation Administration. Continous Lower Energy, Emissions, and Noise (CLEEN) Program. URL: "https://www.faa.gov/about/office_org/headquarters_offices/apl/research/aircraft_technology/cleen/#pg".

[20] International Civil Aviation Organization (ICAO). *Doc. 9426-AN/924 Air Traffic Services Planning Manual*, 1^{st} edition, 1984.

[21] International Civil Aviation Organization (ICAO). *Doc. 4444. Procedures for Air Navigation Services. Air Traffic Management*, 16^{th} edition, 2016.

[22] Heathrow Airport Expansion Consultation. Our Approach to Noise, January 2018.

[23] *Worldwide Air Transportation Conference. Night Flight Restrictions*, number ATConf/6-WP/8, 2013. International Civil Aviation Organization (ICAO).

[24] The National Archives. UK Legislation. Civil Aviarion Act 2006. URL: "https://www.legislation.gov.uk/ukpga/2006/34/contents".

[25] M. J. T. Smith. *Aircraft Noise*. Cambridge Aerospace Series. Cambridge University Press, 1989. doi: 10.1017/CBO9780511584527.

[26] R. Davy and H. Remy. Airframe noise characteristics of a 1/11 scale airbus model. *Aeroacoustics Conferences*, June 1998. doi: 10.2514/6.1998-2335. URL https://doi.org/10.2514/6.1998-2335.

[27] M. Macaraeg. Fundamental investigations of airframe noise. *American Institute of Aeronautics and Astronautics*, June 1998. doi: 10.2514/6.1998-2224. URL https://doi.org/10.2514/6.1998-2224.

[28] J. Hayes, W. Horne, P. Soderman, and P. Bent. Airframe noise characteristics of a 4.7 percent scale DC-10 model. *Aeroacoustics Conferences*, May 1997. doi: 10.2514/6.1997-1594. URL https://doi.org/10.2514/6.1997-1594.

[29] K. R. Meadows, T. F. Brooks, W. M. Humphreys, W. W. Hunter, and C. H. Gerhold. Aeroacoustic Measurements of a Wing-Flap Configuration. Technical report, NASA Langley, 1997.

[30] F. Farassat and M. K. Myers. Extension of Kirchhoff's formula to radiation from moving surfaces. *Journal of Sound and Vibration*, 123(3):451 – 460, 1988. ISSN 0022-460X. doi: https://doi.org/10.1016/S0022-460X(88)80162-7.

[31] J. E. F. Williams and D. L. Hawkings. Sound generation by turbulence and surfaces in arbitrary motion. *Philosophical Transactions of the Royal Society of London A: Mathematical, Physical and Engineering Sciences*, 264(1151):321–342, 1969. ISSN 0080-4614. doi: 10.1098/rsta.1969.0031.

[32] K. S. Brentner and F. Farassat. Modeling aerodynamically generated sound of helicopter rotors. *Progress in Aerospace Sciences*, 39(2):83 – 120, 2003. ISSN 0376-0421. doi: https://doi.org/10.1016/S0376-0421(02)00068-4.

[33] The Boeing Preliminary Design Department. Assessment of Variable Camber for Application to Transport Aircraft. Technical report, NASA Contractor Report CR-1589305, National Aeronautics and Space Administration Langley Research Center, Hampton, VA, November 1980.

[34] NASA and The U.S Air Force Laboratory. Adaptive Compliant Trailing Edge Flaps on a GIII Airplane. Technical report, National Aeronautics and Space Administration, 2014. URL: "https://www.nasa.gov/centers/armstrong/research/ACTE/index.html".

[35] Y. Tani, Y. Yamashita, K. Miyazaki, S. Aso, H. Ura, and T. Ito. Morphing flap concept to reduce the flap side edge noise for aircraft wing slotted flaps. *AIAA SciTech Forum*, January 2014. doi: 10.2514/6.2014-0019.

[36] F. Afonso, J. Vale, F. Lau, and A. Suleman. Performance based multidisciplinary design optimization of morphing aircraft. *Aerospace Science and Technology*, 67:1 – 12, 2017. ISSN 1270-9638. doi: https://doi.org/10.1016/j.ast.2017.03.029.

[37] A. Suleman, F. Afonso, J. Vale, and F. Lau. Performance Based MDO of a Joined-Wing Regional Transport Aircraft (For Challenges in the Design of Joined Wings (Special Session). *AIAA SciTech Forum*, January 2015. doi: 10.2514/6.2015-0696.

[38] Novel Air Vehicles Configurations: From Fluttering Wings to Morphing Flight (NOVEMOR). URL: "https://trimis.ec.europa.eu/project/novel-air-vehicles-configurations-fluttering-wings-morphing-flight", 2011-2014.

[39] M. R. R. Dias. Aeroacoustical Module Development for the NOVEMOR MDO Software. Master's thesis, Instituto Superior Técnico (IST), July 2017.

[40] S. Perennes and M. Roger. Aerodynamic noise of a two-dimensional wing with high-lift devices. *Aeroacoustics Conferences. American Institute of Aeronautics and Astronautics*, June 1998. doi: 10.2514/6.1998-2338.

[41] C. Streett, J. Casper, D. Lockard, M. Khorrami, R. Stoker, R. Elkoby, W. Wenneman, and J. Underbrink. Aerodynamic Noise Reduction for High-Lift Devices on a Swept Wing Model, January 2006.

[42] W. Dobrzynski, K. Nagakura, B. Gehlhar, and A. Buschbaum. Airframe noise studies on wings with deployed high-lift devices. *Aeroacoustics Conferences. American Institute of Aeronautics and Astronautics*, June 1998. doi: 10.2514/6.1998-2337.

[43] W. Dobrzynski, B. Gehlhar, and H. Buchholz. Model and full scale high-lift wing wind tunnel experiments dedicated to airframe noise reduction. *Aerospace Science and Technology*, 5(1):27 – 33, 2001. ISSN 1270-9638.

[44] Y. P. Guo and M. C. Joshi. Noise Characteristics of Aircraft High Lift Systems. *AIAA Journal*, 41 (7):1247–1256, July 2003. ISSN 0001-1452. doi: 10.2514/2.2093.

[45] K. Takeda, X. Zhang, and P. Nelson. Unsteady aerodynamics and aeroacoustics of a high-lift device configuration. *Aerospace Sciences Meetings. American Institute of Aeronautics and Astronautics*, January 2002. doi: 10.2514/6.2002-570.

[46] W. Dobrzynski and M. P. Pollenske. Slat noise source studies for farfield noise prediction. *Aeroacoustics Conferences. American Institute of Aeronautics and Astronautics*, May 2001. doi: 10.2514/6.2001-2158.

[47] J. R. Radeztsky, B. Singer, and M. Khorrami. Detailed Measurements of a flap Side-edge Flow Field. *Aerospace Sciences Meetings. American Institute of Aeronautics and Astronautics*, January 1998. doi: 10.2514/6.1998-700.

[48] J. Kendall and W. Ahtye. Noise generation by a lifting wing/flap combination at Reynolds numbers to 2.8 x 10 to the 6th. *Aerospace Sciences Meetings. American Institute of Aeronautics and Astronautics*, January 1980. doi: 10.2514/6.1980-35. URL `https://doi.org/10.2514/6.1980-35`.

[49] M. R. Fink and R. H. Schlinke. Airframe Noise Component Interaction Studies. *Journal of Aircraft. American Institute of Aeronautics and Astronautics*, 17(2):99–105, February 1980. ISSN 0021-8669. doi: 10.2514/3.57880. URL `https://doi.org/10.2514/3.57880`.

[50] T. F. Brooks and W. M. Humphreys. A deconvolution approach for the mapping of acoustic sources (DAMAS) determined from phased microphone arrays. *Journal of Sound and Vibration*, 294(4): 856 – 879, 2006. ISSN 0022-460X. doi: https://doi.org/10.1016/j.jsv.2005.12.046.

[51] C. McGinley, J. Anders, and F. Spaid. Measurements of Reynolds stress profiles on a high-lift airfoil. *Fluid Dynamics and Co-located Conferences*, Jun 1998. doi: 10.2514/6.1998-2620.

[52] S. Olson, F. Thomas, and R. Nelson. Mechanisms of slat noise production in a 2D multi-element airfoil configuration, May 2001.

[53] K. Takeda, G. Ashcroft, X. Zhang, and P. Nelson. Unsteady aerodynamics of slat cove flow in a high-lift device configuration. *American Institute of Aeronautics and Astronautics*, January 2001. doi: 10.2514/6.2001-706.

[54] C. L. Rumsey, R. T. Biedron, and J. Thomas. CFL3D: Its History and some Recent Applications, June 1997. NASA TM-112861.

[55] Langley Research Center. NASA. CFL3D Homepage, March 2013. https://cfl3d.larc.nasa.gov/.

[56] M. Takallu and K. Laflin. Reynolds-Averaged Navier-Stokes simulations of two partial-span flap wing experiments. *Aerospace Sciences Meetings*, January 1998. doi: 10.2514/6.1998-701.

[57] M. E. Berkman, M. R. Khorrami, M. Choudhari, and S. S. Sadowski. Investigation of High-Lift Flowfield of an Energy Efficient Transport Wing. *Journal of Aircraft*, 37(1):45–52, January 2000. ISSN 0021-8669. doi: 10.2514/2.2560.

[58] M. R. Khorrami, B. A. Singer, and R. H. Radeztsky Jr. Reynolds-Averaged Navier-Stokes Computations of a Flap-Side-Edge Flowfield. *American Institute of Aeronautics and Astronautics*, 37(1): 14–22, January 1999. ISSN 0001-1452. doi: 10.2514/2.687.

[59] P. Spalart and S. Allmaras. A one-equation turbulence model for aerodynamic flows. *American Institute of Aeronautics and Astronautics*, January 1992. doi: 10.2514/6.1992-439.

[60] D. L. Mathias, K. R. Roth, J. C. Ross, S. E. Rogers, and R. M. Cummings. Navier-Stokes Analysis of the Flow About a Flap Edge. *Journal of Aircraft*, 35(6):833–838, November 1998. ISSN 0021-8669. doi: 10.2514/2.2384.

[61] S. E. Rogers and N. Ames Research Center. INS3D Homepage. URL: `https://www.nas.nasa.gov/publications/software/docs/ins3d/index.html`.

[62] B. Baldwin and T. Barth. A one-equation turbulence transport model for high Reynolds numbers wall-bounded flows. *Aerospace Sciences Meetings. American Institute of Aeronautics and Astronautics*, January 1991. doi: 10.2514/6.1991-610.

[63] R. Satti, Y. Li, R. Shock, and S. Noelting. Unsteady Flow Analysis of a Multi-Element Airfoil Using Lattice Boltzmann Method. *AIAA Journal*, 50(9):1805–1816, September 2012. ISSN 0001-1452. doi: 10.2514/1.J050906.

[64] S. Chen and G. D. Doolen. Lattice Boltzmann Method For Fluid Flows. *Annual Review of Fluid Mechanics*, 30(1):329–364, 1998.

[65] B. A. Singer, D. P. Lockard, and K. S. Brentner. Computational Aeroacoustic Analysis of Slat Trailing-Edge Flow. *AIAA Journal*, 38(9):1558–1564, September 2000. ISSN 0001-1452. doi: 10.2514/2.1177.

[66] D. Lockard and M. Choudhari. Noise Radiation from a Leading-Edge Slat. *Aeroacoustics Conferences. American Institute of Aeronautics and Astronautics*, May 2009. doi: 10.2514/6.2009-3101.

[67] M. J. Lighthill. On sound generated aerodynamically I. General theory. *Proceedings of the Royal Society of London A: Mathematical, Physical and Engineering Sciences*, 211(1107):564–587, 1952. ISSN 0080-4630. doi: 10.1098/rspa.1952.0060.

[68] B. Singer, K. Brentner, D. Lockard, and G. Lilley. Simulation of Acoustic Scattering From a Trailing Edge. *Journal of Sound and Vibration*, 230(3):541 – 560, 2000. ISSN 0022-460X. doi: https://doi.org/10.1006/jsvi.1999.2628.

[69] M. M. Choudhari and M. R. Khorrami. Effect of Three-Dimensional Shear-Layer Structures on Slat Cove Unsteadiness. *AIAA Journal*, 45(9):2174–2186, September 2007. ISSN 0001-1452. doi: 10.2514/1.24812.

[70] M. R. Khorrami, M. E. Berkman, and M. Choudhari. Unsteady Flow Computations of a Slat with a Blunt Trailing Edge. *AIAA Journal*, 38(11):2050–2058, November 2000. ISSN 0001-1452. doi: 10.2514/2.892.

[71] C. Rumsey, R. Biedron, F. Farassat, and P. Spence. Ducted-Fan Engine Acoustic Predictions Using a Navier–Stokes Code. *Journal of Sound and Vibration*, 213(4):643 – 664, 1998. ISSN 22-460X. doi: https://doi.org/10.1006/jsvi.1998.1519.

[72] F. Menter. Improved Two-Equation k-w Turbulent Models for Aerodynamic Flows, 1992. NASA TM103975.

[73] P. Spalart, W.-H. Jou, M. Strelets, and S. Allmaras. Comments on the Feasibility of LES for Wings, and on a Hybrid RANS/LES Approach. In *First AFOSR International Conference on DNS/LES*, pages 137 – 147, Ruston, USA, 1997. Greyden Press.

[74] B. Nebenführ, H. Yao, S.-H. Peng, and L. Davidson. Hybrid RANS/LES Simulations for Aerodynamic and Aeroacoustic Analysis of a Multi-Element Airfoil. In 19^{th} *AIAA/CEAS Aeroacoustics Conference*, May 2013. ISBN 978-1-62410-213-4.

[75] H. Yao, L. Davidson, L.-E. Eriksson, O. Grundestam, S.-H. Peng, and P. Eliasson. Surface Integral Analogy Approaches to Computing Noise Generated by a 3D High-Lift Wing Configuration. *American Institute of Aeronautics and Astronautics*, January 2012. doi: 10.2514/6.2012-386. URL `https://doi.org/10.2514/6.2012-386`.

[76] N. Curle. The influence of solid boundaries upon aerodynamic sound. *Proceedings of the Royal Society of London A: Mathematical, Physical and Engineering Sciences*, 231(1187):505–514, 1955. ISSN 0080-4630. doi: 10.1098/rspa.1955.0191.

[77] Flexsys. https://www.flxsys.com.

[78] Smart Intelligent Aircraft Structures (SARISTU). *Proceedings of the Final Project Conference*. Number 1. Springer International Publishing, 2015. ISBN 978-3-319-22413-8. doi: 10.1007/978-3-319-22413-8.

[79] G. Fujiwara and N. Nguyen. Aerostructural Design Optimization of a Subsonic Wing with Continuous Morphing Trailing Edge, June 2017.

[80] Z. Lyu and J. R. R. A. Martins. Aerodynamic Shape Optimization of an Adaptive Morphing Trailing-Edge Wing. *Journal of Aircraft*, 52(6):1951–1970, July 2015. ISSN 0021-8669. doi: 10.2514/1.C033116.

[81] O. Schorsch, C. Nagel, and A. Lühring. Chapter 7 - Morphing Skin: Foams. In *Morphing Wing Technologies*, pages 207 – 230. Butterworth-Heinemann, 2018. ISBN 978-0-08-100964-2. doi: https://doi.org/10.1016/B978-0-08-100964-2.00007-1.

[82] A. Vigliotti and D. Pasini. Chapter 8 - The Design of Skin Panels for Morphing Wings in Lattice Materials. In *Morphing Wing Technologies*, pages 231 – 246. Butterworth-Heinemann, 2018. ISBN 978-0-08-100964-2. doi: https://doi.org/10.1016/B978-0-08-100964-2.00008-3.

[83] A. Airoldi, G. Sala, L. A. Landro, P. Bettini, and A. Gilardelli. Chapter 9 - Composite Corrugated Laminates for Morphing Applications. In *Morphing Wing Technologies*, pages 247 – 276. Butterworth-Heinemann, 2018. ISBN 978-0-08-100964-2.

[84] R. Pecora, S. Barbarino, A. Concilio, L. Lecce, and S. Russo. Design and Functional Test of a Morphing High-lift Device for a Regional Aircraft. *Journal of Intelligent Material Systems and Structures*, 22(10):1005–1023, July 2011. ISSN 1045-389X. doi: 10.1177/1045389X11414083.

[85] A. Concilio, I. Dimino, M. Ciminello, R. Pecora, F. Amoroso, and M. Magnifico. Chapter 17 - An Adaptive Trailing Edge. In *Morphing Wing Technologies*, pages 517 – 545. Butterworth-Heinemann, 2018. ISBN 978-0-08-100964-2. doi: https://doi.org/10.1016/B978-0-08-100964-2.00017-4.

[86] J. D. Anderson Jr. *Computational Fluid Dynamics*, chapter 2, pages 33–75. McGraw-Hill Education, 1995.

[87] J. H. Ferziger and M. Peric. *Computational Methods for Fluid Dynamics*, volume 3. Springer, January 2002.

[88] G. Alfonsi. Reynolds-Averaged Navier-Stokes Equations for Turbulence Modeling. *Applied Mechanics Reviews - Appl. Mech. Rev.*, 62, July 2009. doi: 10.1115/1.3124648.

[89] C. Nguyen. Turbulence Modelling, November 2005.

[90] S. Rogers, F. Menter, P. Durbin, and N. Mansour. A comparison of turbulence models in computing multi-element airfoil flows. *American Institute of Aeronautics and Astronautics*, January 1994. doi: 10.2514/6.1994-291.

[91] P. Godin, D. W. Zingg, and T. E. Nelson. High-Lift Aerodynamic Computations with One- and Two-Equation Turbulence Models. *AIAA Journal*, 35(2):237–243, 1997. ISSN 0001-1452. doi: 10.2514/2.113.

[92] F. Palacios. Stanford University Unstructured (SU2): Open-source Analysis and Design Technology for Turbulent Flows, 2014.

[93] W. O. Valarezo and D. J. Mavriplis. Navier-Stokes applications to high-lift airfoil analysis. *Journal of Aircraft*, 32:618–624, May 1995.

[94] D. Jackson and B. Launder. Osborne Reynolds and the Publication of His Papers on Turbulent Flow. *Annu. Rev. Fluid Mech.*, July 2007.

[95] Advisory Group for Aerospace Research and Development (AGARD). *AGARD-AR-303: A Selection of Experimental Test Cases for the Validation of CFD Codes*. North Atlantic Treaty Organization, August 1994.

[96] B. van den Berg. Boundary layer measurements on a two-dimensional wing with flap. Technical report, National Aerospace Laboratory, NLR TR 79009 U, 1979.

[97] T. J. A. Dolle. Flap Performance Improvement by Surface Excitation. Master's thesis, Delft University of Technology, 2009.

[98] D. C. Wilcox. Turbulence Modeling for CFD, 1994.

[99] F. Moukalled, L. Mangani, and M. Darwish. *The Finite Volume Method in Computational Fluid Dynamics: An Advanced Introduction with OpenFOAM and Matlab*. Springer International Publishing.

[100] F. Palacios, M. R. Colonno, A. C. Aranake, A. Campos, S. R. Copeland, T. Economon, A. Lonkar, T. W. Lukaczyk, T. W. R. Taylor, and J. Alonso. Stanford University Unstructured (SU2): An open-source integrated computational environment for multi-physics simulation and design. *AIAA Journal*, 2013:1–60, January 2013.

[101] P. L. Roe. Approximate Riemann Solvers, Parameter Vectors, and Difference Schemes. *Journal of Computational Physics*, 43(2):357 – 372, 1981. ISSN 0021-9991. doi: https://doi.org/10.1016/0021-9991(81)90128-5.

[102] A. Jameson, W. Schmidt, and E. Turkel. Numerical solution of the euler equations by Finite Volume Methods using Runge Kutta time stepping schemes. *Fluid Dynamics and Co-located Conferences*, June 1981. doi: 10.2514/6.1981-1259.

[103] B. Leer. Towards the ultimate conservative difference scheme. V. A. second-order sequel to Godunov's method. *Journal of Computational Physics*, 32(1):101 – 136, 1979. ISSN 0021-9991. doi: https://doi.org/10.1016/0021-9991(79)90145-1.

[104] E. Toro. *Riemann Solvers and Numerical Methods for Fluid Dynamics: A Practical Introduction*, chapter 13th, High–Order and TVD Methods for Scalar Equations, pages 426–449. Springer International Publishing.

[105] V. Venkatakrishnan. On the accuracy of limiters and convergence to steady state solutions. *American Institute of Aeronautics and Astronautics*, January 1993. doi: 10.2514/6.1993-880.

[106] A. Jameson and S. Shankaran. An Assessment of Dual-Time Stepping, Time Spectral and Artificial Compressibility Based Numerical Algorithms for Unsteady Flow with Applications to Flapping Wings. In *19th AIAA Computational Fluid Dynamics Conference*, June 2009. ISBN 978-1-62410-137-3. doi: 10.2514/6.2009-4273.

[107] S. Rienstra and A. Hirschberg. *An Introduction to Acoustics*. Eindhoven University of Technology, August 2004.

[108] T. F. Brooks and T. H. Hodgson. Trailing edge noise prediction from measured surface pressures. *Journal of Sound and Vibration*, 78(1):69 – 117, 1981. ISSN 0022-460X. doi: https://doi.org/10.1016/S0022-460X(81)80158-7.

[109] T. F. Brooks, D. Pope, and M. A. Marcolini. Airfoil self-noise and prediction. *NASA*, 1218, August 1989.

[110] J. C. Yu and C. K. W. Tam. Experimental Investigation of the Trailing Edge Noise Mechanism. *AIAA Journal*, 16(10):1046–1052, October 1978. ISSN 0001-1452. doi: 10.2514/3.61003.

[111] M. R. Fink and D. A. Bailey. Airframe Noise Reduction Studies and Clean-Airframe Noise Investigation. Technical Report NASA-CR-159311, R80-914626-12, United Technologies Research Center, April 1980.

[112] C. K. W. Tam. Discrete Tones of Isolated Airfoils. *The Journal of the Acoustical Society of America*, 55(6):1173–1177, 1974. doi: 10.1121/1.1914682.

[113] T. F. Brooks and W. M. Humphreys. Flap-edge Aeroacoustic Measurements and Predictions. *Journal of Sound and Vibration*, 261(1):31 – 74, 2003. ISSN 0022-460X. doi: https://doi.org/10.1016/S0022-460X(02)00939-2.

[114] J. Souto. Development of an Aeroacoustic Prediction Tool for Wind Turbine Noise. Master's thesis, Instituto Técnico Superior, May 2017.

[115] F. Farassat. Derivation of Formulations 1 and 1A of Farassat. *NASA/TM-2007-214853*, March 2007.

[116] F. Farassat. Theory of Noise Generation of Moving Bodies with an Application to Helicopter Rotors. Technical report, NASA Langley Research Center, 1975. NASA TR R-451.

[117] K. S. Brentner. Numerical Algorithms for Acoustic Integrals with Examples for Rotor Noise Prediction. *AIAA Journal*, 35(4):625–630, April 1997. ISSN 0001-1452. doi: 10.2514/2.182.

[118] S. W. Smith. *The Scientist and Engineer's Guide to Digital Signal Processing*. California Technical Publishing, San Diego, CA, USA, 1997. ISBN 0-9660176-3-3.

[119] W. C. van der Velden and S. Oerlemans. Numerical analysis of noise reduction mechanisms on improved trailing edge serrations using the Lattice Boltzmann method. *American Institute of Aeronautics and Astronautics*, January 2017. doi: 10.2514/6.2017-1379.

[120] S. Nadarajah and A. Jameson. *A comparison of the continuous and discrete adjoint approach to automatic aerodynamic optimization*, chapter Aerospace Science Meetings, pages 1–20. American Institute of Aeronautics and Astronautics, January 2000. doi: 10.2514/6.2000-667.

[121] A. Jameson. Aerodynamic shape optimization using the adjoint method, January 2003.

[122] M. A. Leschziner. Computation of aerodynamic flows with turbulence-transport models based on second-moment closure. *Computers and Fluids*, 24(4):377–392, 1995.

[123] H. Cao and K. Kusunose. Grid generation and Navier-Stokes analysis of multi-element airfoils. *Aerospace Sciences Meetings. American Institute of Aeronautics and Astronautics*, January 1994. doi: 10.2514/6.1994-748.

[124] S. E. Rogers, N. L. Wiltberger, and D. Kwak. Efficient simulation of incompressible viscous flow over single and multielement airfoils. *Journal of Aircraft*, 30(5):736–743, September 1993. ISSN 0021-8669. doi: 10.2514/3.46405.

[125] T. Larsson. Separated and High-Lift Flows over Single and Multi-Element Airfoils. *International Council of Aeronautical Sciences*, January 1994.

[126] K. Kusunose, L. Wigton, and P. Meredith. A rapidly converging viscous/inviscid coupling code for multi-element airfoil configurations. *American Institute of Aeronautics and Astronautics*, January 1991. doi: 10.2514/6.1991-177.

[127] J. Häuser and Y. Xia. *Modern Introduction to Grid Generation*. Department of Parallel Computing Center of Logistics and Expert Systems, May 2019.

[128] B. E. Launder and W. Rodi. The turbulent wall jet. *Progress in Aerospace Sciences*, 19:81–128, 1979. ISSN 0376-0421.

[129] www.solidworks.com.

[130] A. B. Orovio, C. Castro, F. Palacios, and E. Zuazua. Continuous Adjoint Approach for the Spalart-Allmaras Model in Aerodynamic Optimization. *American Institute of Aeronautics and Astronautics*, 50(3):631–646, March 2012. ISSN 0001-1452. doi: 10.2514/1.J051307.

[131] G. F. Corliss, C. Faure, A. Griewank, and L. Hascoet. Automatic Differentiation of Algorithms: From Simulation to Optimization. Springer Verlag, 2002.

[132] T. Sederberg and S. R. Parry. Free-form deformation of solid geometric models. In *Proc. 13th Annu. Conf. Comput. Graph. Interact. Tech.*, volume 20 of *ACM Siggraph Computer Graphics*, pages 151–160, August 1986.

[133] R. M. Hicks and P. A. Henne. Wing Design by Numerical Optimization. *Journal of Aircraft*, 15, September 1977.

[134] J. Lourenço. Supersonic and Transonic Adjoint-based Optimization of Airfoils. Master's thesis, Instituto Superior Técnico (IST), November 2018.

[135] S. Moreau, M. Roger, and J. Christophe. Flow Features and Self-noise of Airfoils Near Stall or in Stall. *15th AIAA/CEAS Aeroacoustics Conference (30th AIAA Aeroacoustics Conference)*, May 2009.

[136] A. Laratro, M. Arjomandi, B. Cazzolato, and R. Kelso. Self-noise and directivity of simple airfoils during stall: An experimental comparison. *Applied Acoustics*, 127:133 – 146, 2017. ISSN 0003-682X.

Appendix A

Sensibility Analysis of the Shape Design Optimisation Set-up

First of all, one must be aware of the typology of the problem, in which the flow conditions remain unchanged with respect to the flapped configuration, meaning that an abrupt increase of lift will inherently result in a parallel drag increase, at least within the first designs of the optimisation cycle. The flapped configuration already implies a drag increase of

$$\Delta C_d(\%) = \frac{C_d|_{flapped} - C_d|_B}{C_d|_B} \cdot 100 = \frac{0.0597 - 0.0216}{0.0216} \cdot 100 = 176\% \tag{A.1}$$

which is an even greater relative increase than the lift coefficient's. As widely explained in section 3.3, the beneficial aerodynamic effect from the high-lift configuration gap is neglected, so it is reasonable to think that the drag coefficient from the optimised airfoil will be greater than the baseline's. In any case, the idea has been tested by setting up the drag coefficient as the objective function to be minimised, together with the geometrical constraints regarding thickness, area, and chord variations, and a lift constraint to impose a positive increment equal or greater than the flapped configuration's ($C_l \geq 2.875$). For any set of scale factors upon the design variables ($\vec{D_v}$) that has been implemented, the optimisation cycle has always showed an undesired behaviour where the line of search gets stuck inside a loop in which the lift remains unchanged, undoubtedly due to the impossibility of a drag reduction while satisfying the lift demand.

The same problem has been encountered for the case in which the lift-to-drag ratio is set as the objective function (in this case, to maximise), where the line of search analogously enters a cul-de-sac design loop. Consequently, these optimisation simulations are not able to achieve the target of the present work.

As a determining result, the present work has developed the shape design optimisation by setting the **lift** as the **objective function** to force the line of search towards an abrupt increase of lift.

A.0.1 Conclusive Optimisation Simulations

The scale factors from the design variables have presented to have the biggest influence on the line of search and thus the final solution, and some of the simulations that have led to determining conclusions are presented.

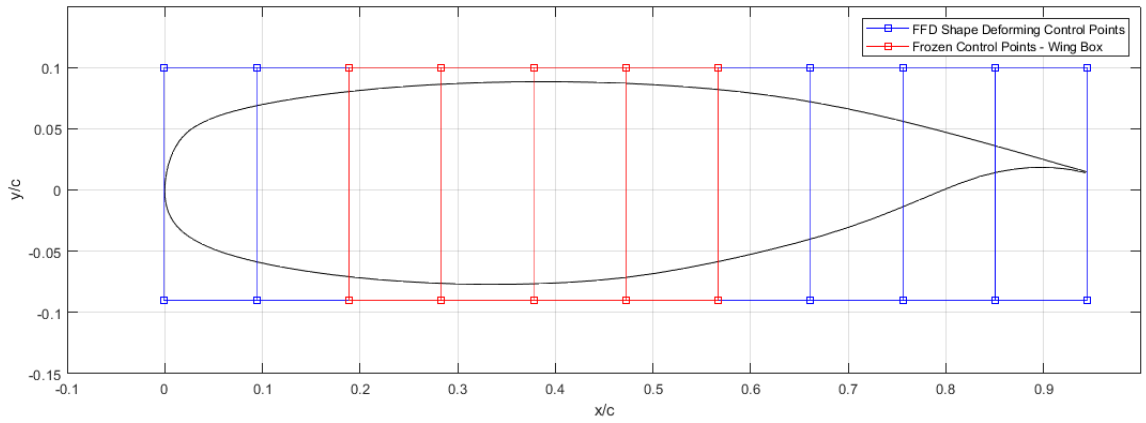

Figure A.1: Design Variables located on the Free Form Deformation box.

The deflections of both leading and trailing edges must emulate a slat and flap deflections. For that, certain directions ought to be imposed onto the design variables. Regarding the ones located on the leading edge, the exploring direction is forced to evolve upstream (negative x) for a chord increase, and towards a negative coordinate y, cambering the airfoil. On the other hand, the ones from the trailing edge are forced to explore towards a positive x and a negative y, for a chord and camber increase, respectively:

$$\text{Leading Edge } \vec{D_v} = \begin{cases} x_i < 0 \\ y_i < 0 \end{cases} \tag{A.2}$$

$$\text{Trailing Edge } \vec{D_v} = \begin{cases} x_i > 0 \\ y_i < 0 \end{cases} \tag{A.3}$$

First Optimisation Conclusive Case

One of the simulations that supplied one of the main conclusive ideas is illustrated in figure A.2, in which all scale factors were set to the same absolute value: $|x_i| = |y_i| = 0.5$, reaching a maximum lift of $C_l = 2.17$, with a drag of $C_d = 0.0697$:

Two features are noticeable within this result. The first is that the line of search explores the leading edge deflection for a beneficial flow acceleration to contribute to stall delay, which is positive. Secondly, the trend of exploration regarding the trailing edge is to deflect it with a severe push from $\vec{D_v} = (10, 0)$ and

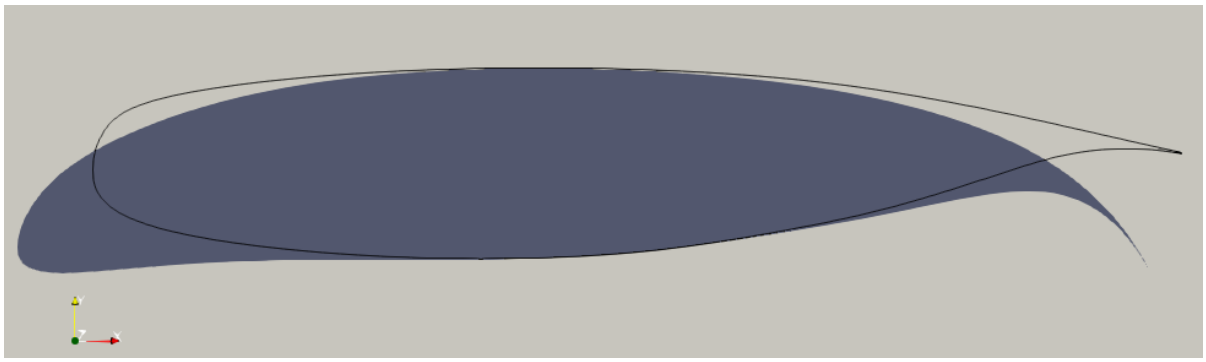

Figure A.2: First conclusive optimisation simulation.

$\vec{D_v} = (10, 1)$, not accounting for chord or sectional area increases. Hence, these edge design variables must be limited in movement with respect to the adjacent ones in order to impose a larger exploration in downwards direction from the other $\vec{D_v}$. This suggested the idea of a gradual allowed movement decrease from the inner towards the trailing edge $\vec{D_v}$.

Second Optimisation Conclusive Case

Once the $\vec{D_v}$ movement progression was implemented, the presence of a drag increase limit constraint was tested, imposing a drag increase not more than the double of the flapped configuration: $C_d \leq (2 \cdot 0.0597 = 0.1194)$. For this case, the resulting morphing airfoil proved advantageous aerodynamic capabilities, where high values of lift were achieved for small drag increases, reaching a lift coefficient of $C_l = 1.94$ for still drag coefficients lower that the flapped configuration, $C_d = 0.035$. However, the structural feasibility is undoubtedly out of reach, as illustrated in figure A.3, surpassing the chord increase limit of 32%, as well as a non-smooth trailing edge deflection.

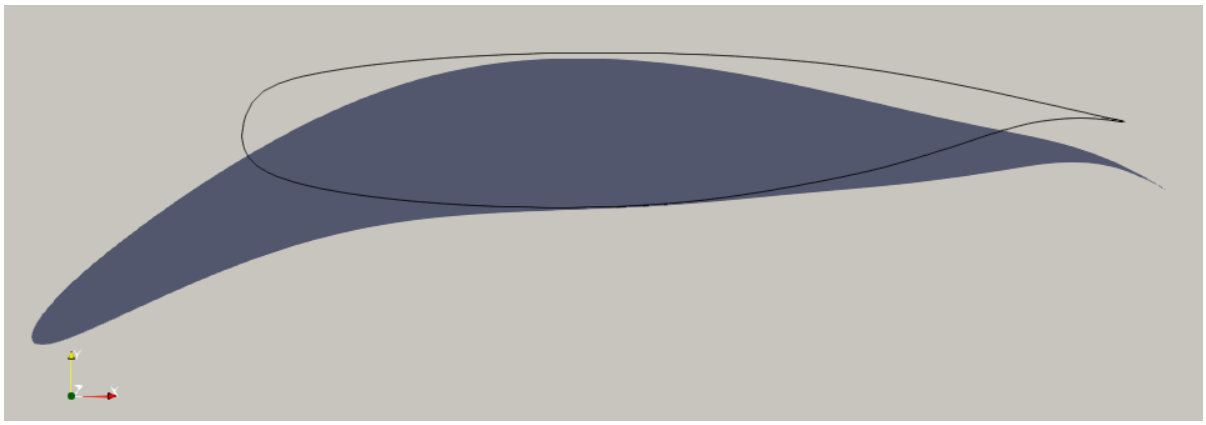

Figure A.3: Second conclusive optimisation simulation.

All designs that were implemented with a C_d constraint showed very similar patterns in the final designs. Consequently, the drag penalisation reduction objective has been faced by imposing a higher leading edge deflection than the previous case's in both directions (0.25), so as to gain enough flow acceleration to energise the boundary layer on the morphed trailing edge, neglecting the C_d constraint.

Appendix B

One-third Octave Bands

Lower Band Limit (Hz)	Center Frequency (Hz)	Upper Band Limit (Hz)
14.1	16	17.8
17.8	20	22.4
22.4	25	28.2
28.2	31.5	35.5
35.5	40	44.7
44.7	50	56.2
56.2	63	70.8
70.8	80	89.1
89.1	100	112
112	125	141
141	160	178
178	200	224
224	250	282
282	315	355
355	400	447
447	500	562
562	630	708
708	800	891
891	1000	1122
1122	1250	1413
1413	1600	1778
1778	2000	2239
2239	2500	2818
2818	3150	3548
3548	4000	4467
4467	5000	5623
5623	6300	7079
7079	8000	8913
8913	10000	11220
11220	12500	14130
14130	16000	17780
17780	20000	22390

Table B.1: One-third octave bands.